ELSEVIER

Progress in Nuclear Magnetic Resonance Spectroscopy 32 (1998) 193–275

PROGRESS IN NUCLEAR MAGNETIC RESONANCE SPECTROSCOPY

Technical aspects of NMR spectroscopy with biological macromolecules and studies of hydration in solution

Gerhard Wider*

Institut für Molekularbiologie und Biophysik, Eidgenössische Technische Hochschule, Hönggerberg, CH-8093 Zürich, Switzerland

Received 1 December 1997

Contents

* Tel.: +41 1 633 3455; fax: +41 1 633 1151.

PII S0079-6565(98)00014-4

Keywords: Protein NMR; Instrumentation; Hydration; Multidimensional NMR

1. Introduction

The first nuclear magnetic resonance (NMR) spectrum of a protein was published some forty years ago [1] and ever since, NMR of biological macromolecules has been a growing field in research and applications [2]. The capability to observe signals from individual atoms in complex biological macromolecules in solution makes possible the measurements of parameters that can be analysed in terms of

molecular structure, conformation and dynamics. Complete assignments of signals in an NMR spectrum to individual atoms in the molecule are a prerequisite for such studies; a problem that cannot generally be solved on the basis of one-dimensional (1D) NMR spectra. Only the application of two-dimensional (2D) NMR spectroscopy [3,4], which spreads signals into two frequency dimensions, allowed the development of a general strategy for the assignment of proton signals in protein spectra using two types of 2D spectra [5–7]. In [^{1}H,^{1}H]-COSY spectra [3,4] protons are correlated which are separated by up to three chemical bonds. In [^{1}H,^{1}H]-NOESY spectra [8,9] correlations between protons which are closer than 0.5 nm through space are detected. The combination of these two techniques allows the assignment of most proton NMR signals to individual protons in small proteins [6,10,11]. In a further step all distances obtainable from NOESY spectra provide the data for the calculation of protein structures [12,13]. These relatively simple techniques allow the determination of structures of proteins with a molecular weight up to 10 kDa whereas for larger proteins extensive signal overlap and increasing resonance linewidths prevent complete assignments of all signals. This barrier can be overcome with three-dimensional (3D) NMR techniques [14] and uniformly ^{13}C- and ^{15}N-labelled proteins. With these methods, systems with molecular weights up to 30 kDa can be studied. However, not only overlapping signals limit the size of the macromolecules that can be investigated; in addition, faster relaxation of the signals with increasing molecular weight leads to a substantial sensitivity loss in experiments. The molecular weight limit can be increased to about 50 kDa using deuteration of the protein to reduce relaxation. Simultaneously with the methodological developments, technical advances revolutionized the design of NMR spectrometers making it possible to implement the complex experimental schemes needed for multidimensional NMR experiments. The increased complexity of the instrumentation has been more and more hidden from the user by complex software control which allows the selection of all modes of operation from a software interface.

In parallel to the methodological and technical developments NMR has become an accepted tool in structural biology and investigations of structure and dynamics of biological macromolecules by NMR are established techniques. The rapid expansion of NMR techniques for applications to biological macromolecules increases the number of interested users with little technical background in NMR spectroscopy. These newcomers find it increasingly difficult to follow and make use of the myriad of NMR experiments available today. The applications and theoretical foundation of biomolecular NMR are described in many excellent books, e.g. [15–27]; however, often only a few experimental schemes are discussed and the common features of different pulse sequences are not always made transparent. In addition, important technical details of experimental implementations are either not discussed or may be missed in the overwhelming amount of information. This review is intended to address the need for an introduction to general technical and methodological aspects of modern NMR experiments with biological macromolecules to these newcomers. The basis for this presentation is not to provide complete experimental schemes, which change rather rapidly, but instead to present the underlying basic technical methods and the basic segments from which individual experiments are constructed and which change much more slowly. The understanding of the basic segments should provide the basis for clarifying the functioning of existing and newly developed experiments and assist the reader in making their own adjustments to experiments or even in developing new methods.

This review was written with a reader in mind who is interested in technical and methodological aspects of NMR with macromolecules in solution, who has had first contact with spectra of proteins in one and two dimensions and knows the principles of their analysis. In addition, knowledge of the product operator formalism [28] is an advantage since the discussion of the basic segments requires the application of this formalism. This text should help such readers to quickly become familiar with the technicalities of multidimensional NMR experiments.

The main text starts with Section 2 where some theoretical aspects are discussed briefly, followed by an introduction of technical principles starting with radiofrequency pulses and ending with multidimensional NMR and data processing. Not only in this section but throughout the text, mathematics is kept to the minimum necessary for the presentation of the

technical aspects of NMR spectroscopy. Section 3 introduces those parts of a modern NMR spectrometer which critically influence the performance of NMR experiments. Section 4 concentrates on the basic experimental segments from which most of the vast number of experiments available today are constructed. Section 5 discusses hydration studies with NMR and serves two purposes. First, it gives examples of experiments using the segments introduced in Section 4 and the principles discussed in Section 2. Second, it introduces the technical aspects of a very interesting application of NMR which allows detailed studies of individual water molecules in the hydration shell of a protein.

2. Basic principles

2.1. Theoretical aspects

This section presents some basic theoretical aspects of NMR which are relevant to a technical discussion of the principles and experimental procedures used when studying biological macromolecules in solution by NMR. A rigorous discussion of the theoretical foundation of NMR can be found in many textbooks, e.g. [16,19,24,26,29]. Only a very limited theoretical foundation is necessary for the technically oriented discussion of NMR methods in the following sections. The concept of energy levels, the Bloch equations and the product operator formalism are sufficient in most cases. NMR is intimately related with frequencies and to obtain a clear distinction between angular frequencies with units rad s^{-1} and technical frequencies in Hertz (Hz) the symbols ω or Ω are used for the former and ν for the latter.

The basis of all NMR experiments is the nuclear spin which can be interpreted as a magnetic moment. A spin $\frac{1}{2}$ nucleus in this view forms a small dipole. This dipole orients either parallel (α state) or antiparallel (β state) to a magnetic field leading to a small energy difference ΔE between the two states

$$\Delta E = \frac{h\gamma}{2\pi} B_0 = \hbar\gamma B_0 \tag{1}$$

where B_0 is a large externally applied homogeneous magnetic field, h is Planck's constant ($\hbar = h/(2\pi)$), and γ the gyromagnetic ratio which is a property of the nucleus and can have a positive or a negative value. Table 1 lists the gyromagnetic ratio and some other properties of nuclei important in NMR of biological macromolecules. From the two states of a dipole the α state is energetically slightly more favourable and thus possesses a higher population than the β state. Transitions between adjacent energy levels can be induced by small additional magnetic fields perpendicular to B_0 which oscillate with a frequency ν_0 fulfilling the resonance condition $\nu_0 = \Delta E/h$. The frequency ν_0 typically lies in the radio-frequency range and is often referred to as the Larmor frequency. In the equilibrium state the Boltzmann distribution favours the lower energy states. Thus, the sum of all contributing nuclear magnetic moments of the individual nuclei leads to a resulting macroscopic magnetization M along the homogeneous external field B_0. In the framework of classical physics the behaviour of this magnetization under the action of time-dependent magnetic fields can be

Table 1
Properties of selected nuclei

Nucleus	Spin	$\gamma^a/10^7$ rad T^{-1} s^{-1}	Natural abundance/%	Relative sensitivity[b]
^1H	$\frac{1}{2}$	26.75196	99.985	1.00
^2H	1	4.106625	0.015	9.65×10^{-3}
^3H	$\frac{1}{2}$	28.53495	–	1.21
^{13}C	$\frac{1}{2}$	6.72828	1.108	1.59×10^{-2}
^{14}N	1	1.93378	99.634	1.01×10^{-3}
^{15}N	$\frac{1}{2}$	− 2.71262	0.366	1.04×10^{-3}
^{17}O	$\frac{5}{2}$	− 3.6281	0.037	2.92×10^{-2}
^{19}F	$\frac{1}{2}$	25.18147	100.00	0.83
^{31}P	$\frac{1}{2}$	10.8394	100.00	6.64×10^{-2}

[a] γ, gyromagnetic ratio: $\chi = \gamma/(2\pi)$.
[b] For an equal number of nuclei relative to protons.

described by the Bloch equations [30]. Because the spin is a quantum mechanical phenomenon this description has a very limited scope, but it proves very useful for the description of single resonance lines under the action of radiofrequency (RF) pulses and thus for the characterization of the effect of RF pulses.

2.1.1. Magnetization, precession and Bloch equations

In a classical description the macroscopic magnetization M created by the spins is described by a vector $\boldsymbol{M}$ parallel to the magnetic field vector $\boldsymbol{B}_0$. $\boldsymbol{M}$ is forced to move away from the direction of $\boldsymbol{B}_0$ by an additional linearly polarized magnetic field $\boldsymbol{B}_1$ perpendicular to $\boldsymbol{B}_0$. $\boldsymbol{B}_1$ must fulfil the resonance condition and oscillate with the resonance frequency ν_0. The magnetization vector $\boldsymbol{M}$ precesses about the resulting magnetic field $\boldsymbol{B} = \boldsymbol{B}_0 + \boldsymbol{B}_1$ with an angular velocity vector $\boldsymbol{\omega}$ pointing in the opposite direction and the components as described in Eq. (2)

$$\boldsymbol{\omega} = -\gamma \boldsymbol{B} = -\gamma(2B_x \cos(2\pi\nu_0 t + \phi), 2B_y \sin(2\pi\nu_0 t + \phi), B_0) \quad (2)$$

where $\boldsymbol{\omega} = (\omega_x, \omega_y, \omega_0)$, $\boldsymbol{B}_0$ is chosen along the z axis and ϕ describes the angle between the x axis and $\boldsymbol{B}_1$. The magnetic field $\boldsymbol{B}_1$ is often applied only for short time periods as RF pulses. The discussion of the motion of the magnetization vector $\boldsymbol{M}$ in space due to RF pulses is usually based on a rotating frame of reference which has the same z axis along the static magnetic field $\boldsymbol{B}_0$ as the laboratory frame but rotates around the z axis with a frequency which is often chosen equal to the resonance frequency ν_0. In this rotating frame of reference, the relevant component of the applied oscillating field $\boldsymbol{B}_1$ appears static making the discussion and visualization much easier. To fulfil the physical requirement that the magnetization vector $\boldsymbol{M}$ returns to its equilibrium position in a finite period of time after a disturbance, a longitudinal relaxation time T_1 (spin–lattice relaxation) is introduced. The loss of coherent precession is described by a transverse relaxation time T_2 (spin–spin relaxation). The motion of the magnetization vector $\boldsymbol{M}$ under the action of the magnetic field $\boldsymbol{B}$ and hence under $\boldsymbol{\omega}$ can be described by the Bloch equations [30]. These equations are presented in Appendix A for further reference.

In the rotating frame where $\boldsymbol{B}_1$ becomes static the main magnetic field $\boldsymbol{B}_0$ vanishes for nuclei with resonance frequency ν_0. Hence, Eq. (2) in this rotating frame contains only a transverse component $\boldsymbol{\omega} = -\gamma(B_1, 0, 0)$ with $\boldsymbol{B}_1$ chosen along the x axis. Consequently $\boldsymbol{M}$ precesses by an angle β around the magnetic field $\boldsymbol{B}_1$ applied as a pulse for the short duration τ

$$\beta = -\gamma B_1 \tau \quad (3)$$

where β is called the flip angle of the pulse. The flip angle is often indicated in degrees, for example during a 90° pulse $\boldsymbol{M}$ can precess from the z axis to the x axis. The angle β depends on γ and is negative for positive γ values such as for protons (Table 1). For positive γ values a magnetic field $\boldsymbol{B}_1$ pointing along the positive x axis turns $\boldsymbol{M}$ towards the negative y axis. A $\boldsymbol{B}_1$ field along the $+y$ axis turns $\boldsymbol{M}$ towards the $+x$ axis [16,31]. When applying an RF pulse with a frequency differing from ν_0 the action of the RF pulse becomes more complex as described in Appendix A, a situation often referred to as non-ideal behaviour of the RF pulses or as off-resonance effects.

The oscillating magnetic field $2B_1 \cos(\omega_{RF} t)$ used for excitation is linearly polarized in the laboratory frame. The transformation into the rotating frame can best be followed when this is thought of as a superposition of two counter-rotating, circular polarized fields with an amplitude B_1. When transforming into the rotating frame one component matches the Larmor frequency whereas the other oscillates at twice the Larmor frequency and does not fulfil the resonance condition. Bloch and Siegert [32] calculated the effect of the non-resonant field and found that it slightly shifts the frequency of the observed resonance lines away from the disturbing field by the small amount $\nu_B = (\gamma B_1)^2/\Delta\nu$ where $\gamma = \gamma/(2\pi)$ and $\Delta\nu$ stands for twice the resonance frequency. The Bloch–Siegert shift is small and amounts, for example, to 0.5 Hz for a frequency of 600 MHz during an RF pulse with duration τ of 10 μs and a flip angle of $\frac{\pi}{2}$ (Eq. (3)) or 90°. The shift disappears as soon as B_1 is switched off. An effect similar to the Bloch–Siegert shift occurs whenever an RF field is applied with a frequency $\Delta\nu$ off-resonance for the nuclear spins. Although first described by Ramsey [33] it is still very often referred to as the Bloch–Siegert effect. To better distinguish it from the effect

due to the counter-rotating field the term "non-resonant effect" was introduced [34]. Since this additional field may be rather strong and close to the resonance frequency, this effect can become quite large and needs to be compensated [35] (Section 2.2.1).

2.1.2. Operators, coherence, and product operator formalism

The description of NMR experiments by the Bloch equations and by magnetization vectors in the rotating frame has significant limitations particularly for the description of multipulse experiments. On the other hand, a full quantum mechanical treatment which describes the state of the system by calculation of the time evolution of the density operator under the action of the appropriate Hamiltonian can be cumbersome. In a quantum mechanical description an RF pulse applied to the equilibrium state creates a coherent superposition of eigenstates which differ in their magnetic quantum number by one, often simply referred to as a coherence. In more complex experiments the magnetic quantum numbers between states may differ by a value q different from one, leading to a q quantum coherence with at least q spins involved. However, only in-phase single quantum coherences (Table 2) are observable and correspond to the classical magnetization detected during the acquisition of an NMR experiment. Multiple quantum coherences cannot be observed directly, but they influence the spin state and this information can be transferred to observable magnetization.

In a step towards a full quantum mechanical treatment, the product operator formalism for spin $\frac{1}{2}$ nuclei was introduced [28]. In this approach it is assumed that there is no relaxation and that the difference in the resonance frequency $\Delta\nu$ of two nuclei is much larger than their mutual scalar coupling J; this situation is often referred to as weak spin–spin coupling whereas strong spin–spin coupling specifies the case where $\Delta\nu$ is close to or even smaller than J. With these assumptions simple rules can be calculated which describe the evolution of spin operators under the action of chemical shift, J coupling and RF pulses. The formalism combines the exact quantum mechanical treatment with an illustrative classical interpretation and is the basis for the development of many NMR experiments. However, some parts of experimental schemes, for example TOCSY sequences (Section 4.2.1), can only be described with a full quantum mechanical treatment. Calculations with the formalism are not difficult, but many terms may have to be treated and implementations of the formalism within computer programs are very helpful in such situations [36,37]. Although most of the experiments applied in biomolecular NMR correlate three or more spins, the majority of interactions can still be understood based on an analysis of two spins. For two spins I and S the operator basis for the formalism contains 16 elements. Two sets of basis operator, cartesian and shift operators, have proven very useful for the description of experimental schemes and are used in parallel. The two basis sets and the nomenclature used to characterize individual states are summarized in Table 2 [28].

The operators I_z and S_z are identical in the two basis sets and a simple relationship exists between the two other cartesian and shift operators:

$$I_x = (I^+ + I^-)/2 \qquad I^+ = I_x + iI_y \tag{4}$$

$$I_y = -i(I^+ - I^-)/2 \qquad I^- = I_x - iI_y$$

Three operators, which represent the action of the Hamiltonians for chemical shift, scalar coupling and

Table 2
Product operator basis for a two-spin system

Cartesian operator basis	Nomenclature	Shift operator basis
I_z, S_z	Longitudinal magnetization	I_z, S_z
I_x, I_y, S_x, S_y	In-phase transverse magnetization	I^+, I^-, S^+, S^-
$2I_xS_z$, $2I_yS_z$	Anti-phase I spin magnetization	$2I^+S_z$, $2I^-S_z$
$2S_xI_z$, $2S_yI_z$	Anti-phase S spin magnetization	$2S^+I_z$, $2S^-I_z$
$2I_xS_x$, $2I_yS_x$, $2I_xS_y$, $2I_yS_y$	Two-spin coherence	$2I^+S^+$, $2I^-S^-$, $2I^-S^+$, $2I^+S^-$
$2I_zS_z$	Longitudinal two-spin order	$2I_zS_z$
E	Unity operator	E

RF pulse, act on these basis operators and may transform them into other operators within the basis set. In this way the spin states created during an NMR experiment can be described and the observable magnetization calculated. The operator formalism can be summarized by simple rules [28] which are listed for both basis systems in Appendix B for further reference. Operators transform individually under these rules even in products of operators except for anti-phase terms which have to be considered as a unit and transformed accordingly; however, they can be treated consecutively when different couplings to the same nucleus exist.

The cartesian operators transform more easily under pulses and their single operators have a direct classical interpretation as magnetization vectors. The shift basis provides a useful alternative for the description of the evolution due to chemical shift and/or the influence of magnetic field gradients (Section 2.3) and is better suited for the description of coherence orders and coherence pathways (Fig. 1). Their single operators describe a transition from the α to the β state, I^+, or from the β to the α state, I^-. Hence, shift product operators are uniquely associated with one coherence order, for example I^+S^+ describes only double quantum coherence (DQC), whereas the cartesian product operator may be associated with several coherence orders, for example $2I_xS_x$ describes a linear combination of both DQC and zero quantum coherence (ZQC). The cartesian x and y components of a multiple quantum coherence are given by linear combinations of the shift or cartesian operators. For example, the ZQCs and DQCs of a two-spin system can be described as follows

$$(\mathrm{ZQC})_x = (2I_xS_x + 2I_yS_y) = (I^+S^- + I^-S^+) \qquad (5)$$

$$(\mathrm{DQC})_x = (2I_xS_x - 2I_yS_y) = (I^+S^+ + I^-S^-)$$

$$(\mathrm{ZQC})_y = (2I_xS_y - 2I_yS_x) = \mathrm{i}(I^+S^- - I^-S^+)$$

$$(\mathrm{DQC})_y = (2I_xS_y + 2I_yS_x) = -\mathrm{i}(I^+S^+ - I^-S^-)$$

On the basis of the operator formalism the selection of particular states using phase cycling of RF pulses in an NMR experiment can be rationalized. Coherences present in an experiment can be classified into their different orders or coherence levels which can be represented in a pictorial way (Fig. 1) to visualize the coherence transfer pathways in an experimental scheme [38,39]. The order of coherence p corresponds to the change q in the magnetic quantum number between the two connected states [28]. Hence for n coupled spins the maximal coherence level that can be reached is n. Free precession conserves the coherence order whereas pulses may cause coherences to be transferred from one order to another (Fig. 1). The sensitivity of a coherence to the phase of an RF pulse is proportional to its order, a q quantum coherence will experience a phase shift $\Delta\phi$ of an RF pulse as $q\Delta\phi$. If the pulse results in a change in the coherence order of Δp, the corresponding phase shift experienced by the affected coherence will be $-\Delta\phi\Delta p$. Proper phase cycling of consecutive RF pulses allows for selection of a specific succession of coherence levels that define a coherence pathway (Fig. 1). The concept of coherence transfer pathways clarifies the role of phase cycling in NMR experiments and describes their action with a simple set of rules [21,24,38,40]. A particular RF pulse can be designed to select a certain difference in coherence order $\Delta p \pm nN$ ($n = 0, 1, 2, \ldots,$) with a phase cycle comprising N phase steps $\Delta\phi$ of the same size equal to $360°/N$. The N signals obtained must be summed together with the proper receiver phase $-k\Delta\phi\Delta p$ to

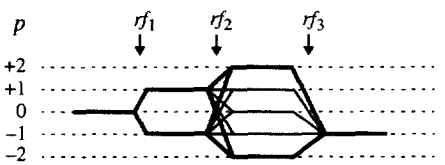

Fig. 1. Coherence level diagram. The coherence levels p are formally represented by products of the shift operators I^- and I^- which are conserved during periods of free evolution. The application of radiofrequency pulses may transfer coherences from one order (level) to another. The positions of three pulses are indicated in the figure by vertical arrows labelled rf_1, rf_2 and rf_3. Thick lines represent the coherence pathway starting at the equilibrium state ($p = 0$) passing through single quantum coherences after the first pulse ($|p| = 1$), reaching double quantum coherences after the second pulse ($|p| = 2$) and ending as observable magnetization ($p = -1$) after the third pulse. Only single quantum coherences ($|p| = 1$) can be observed. The spectrometer detects only one of these two coherence levels which is usually assumed to be $p = -1$ [38] and hence all other coherence orders after the third pulse cannot be detected and therefore are not drawn. Thin lines indicate alternative pathways which have to be suppressed if only the pathway indicated by thick lines should contribute to the signal measured at the end of the sequence.

compensate for the phase change experienced by the coherence, k takes on values {0, 1, 2, 3, ...}. An example for the design of a phase cycle using this system is given in Section 4.2.1 with the discussion of the double quantum filter. A detailed discussion of phase cycling can be found in most textbooks on NMR, e.g. [16,21,24,26].

2.1.3. Descriptive representations of experimental schemes

An NMR experiment can be graphically described to a limited extent based on a classical physical model using populations and magnetization vectors in the rotating frame or based on quantum mechanical principles using the product operator formalism. Both descriptions find widespread applications for the discussion and development of NMR experiments. The different representations are discussed on the basis of the scheme shown in Fig. 2. The application of this experiment to a system of two scalar coupled spins I and S is described with four different representations in Fig. 3 for each of the five time points a to e. Fig. 3 represents energy level diagrams (E), the observable spectra (S), magnetization vector diagrams (V) and the notation in the product operator formalism (O) showing the cartesian and the shift operator basis. In Fig. 3 spins I and S are assumed to be proton and carbon nuclei, respectively, with the size of representative vectors proportional to the corresponding populations, but qualitatively the figure applies to all nuclei with spin $\frac{1}{2}$ and positive gyromagnetic ratio.

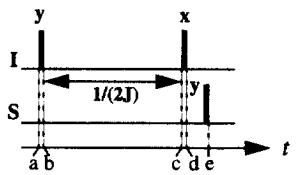

Fig. 2. Sketch of the experimental scheme used for the discussion of different representations shown in Fig. 3. The black narrow bars indicate 90° RF pulses, five time-points on the time axis t are denoted by the letters a, b, c, d and e. The RF pulses applied on-resonance to the two species of nuclei I and S are indicated on the lines marked with the corresponding letters, a particular pulse acts only on one nuclear species. The scalar coupling between the two spins is J. The two pulses applied on spin I are separated by the time period $(2J)^{-1}$. The phases of the RF pulses are indicated by x or y at the top of the pulses, where x or y stand for the application of the B_1 field in the rotating frame along the positive x or y axis, respectively.

The experiment in Fig. 2 starts at time point a in thermal equilibrium (Fig. 3) where the populations on the upper P_u and the lower energy level P_l across a transition fulfil the Boltzmann distribution (Eq. (6)). Because ΔE in Eq. (1) is typically much smaller than kT we can approximate this exponential distribution by the first term in a Taylor expansion

$$P_u/P_l = \exp\left(-\frac{\Delta E}{kT}\right) \cong 1 - \frac{\Delta E}{kT} = 1 - \frac{\gamma\hbar B_o}{kT} \qquad (6)$$

where k is Boltzmann's constant and T the absolute temperature. With Eq. (1) the energies E_1, E_2, E_3, and E_4 of the four different energy levels in the system can be calculated

$$E_1 = h(-\nu_I - \nu_S + J/2)/2 \qquad (7)$$

$$E_2 = h(-\nu_I + \nu_S - J/2)/2$$

$$E_3 = h(\nu_I - \nu_S - J/2)/2$$

$$E_4 = h(\nu_I + \nu_S + J/2)/2$$

where ν_I and ν_S stand for the resonance frequencies of the I and S nuclei, respectively. The resonance frequencies of nuclei with positive gyromagnetic ratio γ such as protons and carbons are negative (Eq. (2)) and, hence, E_1 becomes the highest and E_4 the lowest energy (Fig. 3). For nuclei with a positive γ value the α state (spin $\frac{1}{2}$) has lower energy than the β state (spin $-\frac{1}{2}$). The polarizations M_I^+ and M_I^- are proportional to the energy differences $(E_4 - E_2)$ and $(E_3 - E_1)$, respectively, and they determine the intensity of the corresponding transitions $2 \leftrightarrow 4$ (24) and $1 \leftrightarrow 3$ (13). The consistent use of signs and transformation properties as presented in Fig. 3 may seem not to be of great importance and, indeed, has very often no direct experimental consequences. But there are situations where inconsistencies occur and the interpretation of data becomes confusing or wrong [31,41].

Apart from the consistent illustration of different representations for the description of an NMR experiment, Fig. 3 demonstrates that the scheme shown in Fig. 2 transfers polarization from proton to carbon spins. At time point d the proton polarization M_I^- is inverted. As a consequence the populations across the carbon transitions 12 and 34 acquire a larger difference than at thermal equilibrium at time point a and, hence, the experimental scheme allows measurement

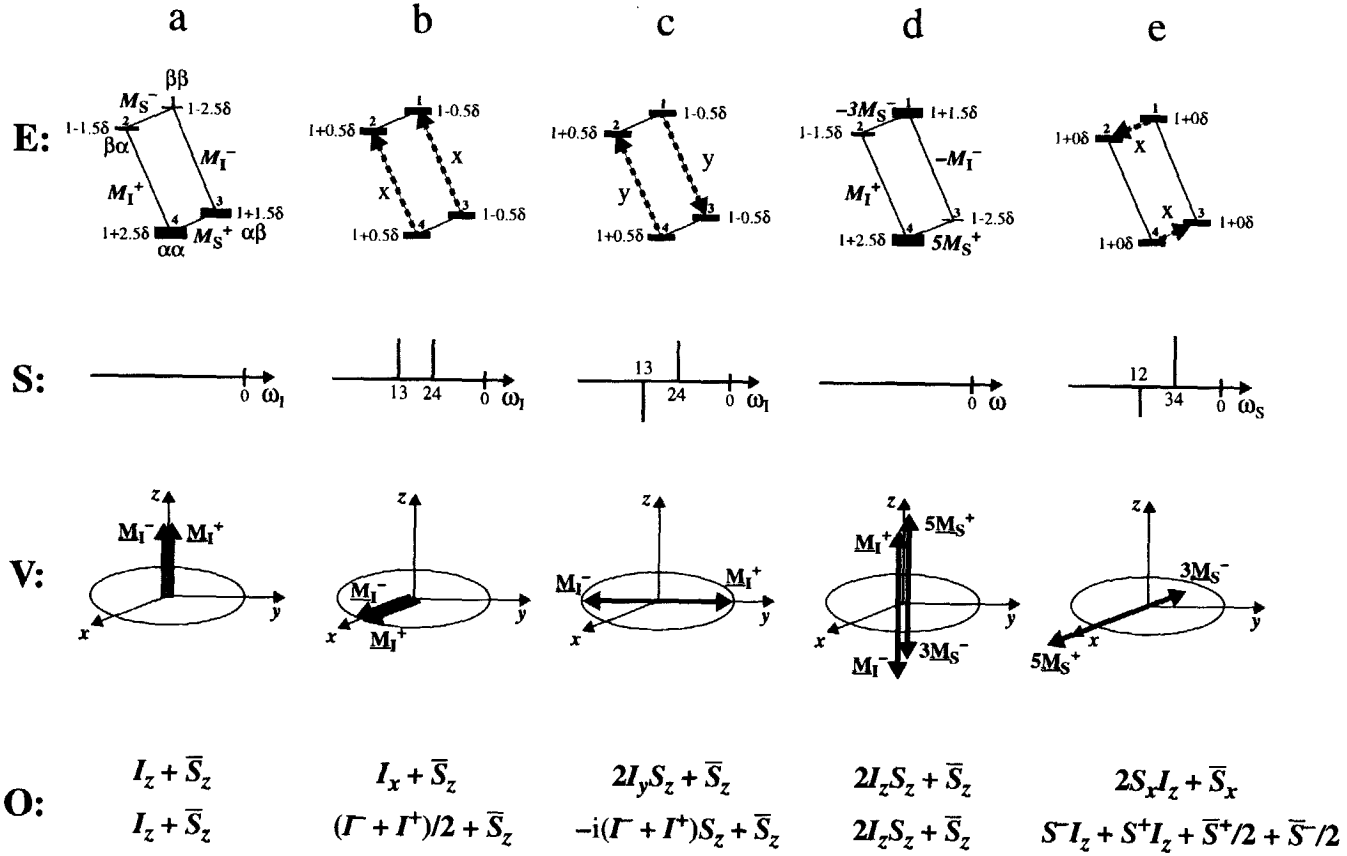

Fig. 3. Different representations used for the description of NMR experiments illustrated for the experimental scheme shown in Fig. 2 using a two-spin system consisting of a proton (I) and a carbon (S) nucleus with a scalar coupling $J > 0$. The representations are qualitatively valid for all spins with a positive gyromagnetic value (Eqs. (2) and (6)). The labels a, b, c, d and e refer to the different time points indicated in Fig. 2. Four different representations are indicated: E, energy level diagrams; S, sketch of the observable spectrum; V, vector diagram; O, product operator formalism in the cartesian and in the shift operator basis. In E the spin states α and β associated with each energy level are indicated with the first character representing the proton spin and the second the carbon spin. The polarizations are indicated by M with the corresponding nucleus indicated as a subscript, the superscript plus or minus signs refer to the sign of the corresponding frequency of the components after excitation in the rotating frame (compare V). The populations of individual energy levels are normalized to one and deviations are given in units of δ with $\delta = \gamma_c \hbar B_0/(kT)$ (Eq. (6)) where γ_c is the gyromagnetic ratio for carbons. The ratio of four between the γ values of protons and carbons was used to represent populations. The coherences evolving after excitation have a "direction" (arrows) [16] and are labelled x and y for x and y phase, respectively. In the schematic stick spectra S, the transitions are labelled according to the numbers of the connected energy levels. The spectra in S and the rotating frame in V are at the proton frequency at the time points a, b and c, at the proton and carbon frequency at time point d and at the carbon frequency at time point e. The magnetization vectors M in V are labelled with the same conventions as the polarizations in E. In the product operator representation the natural S spin magnetization is indicated by the operator $\bar{S}$.

of carbon spectra with higher sensitivity. Such polarization transfer experiments are extremely important in heteronuclear NMR experiments and are discussed further in Section 4.2.3.

2.1.4. Relaxation

Relaxation processes re-establish an equilibrium distribution of spin properties after a perturbation. After a disturbance, the non-equilibrium state decays in the simplest case exponentially characterized by the spin–lattice relaxation time T_1. Re-establishing thermal equilibrium requires changes in the population distribution of the spin states and lowers the energy of the spin system. Thus, it involves energy transfer from the spin system to its surroundings which are usually referred to as the lattice. Microscopically, relaxation is caused by fluctuating magnetic fields. Dynamical processes such as atomic or molecular motion produce fluctuating dipolar interactions and facilitate spin–lattice relaxation. The efficiency of the relaxation process depends on the extent of the overlap between the frequency spectrum of the motional process and the relevant resonance frequencies. This overlap is described by the spectral density function $J(\omega)$. Since $J(\omega)$ is the Fourier transform of the time correlation function describing the motion, its functional form depends on the mechanism of motion. An exponential correlation function with correlation time τ_c results in the spectral density function [16,24,29]

$$J(\omega) = \frac{2}{5} \frac{\tau_c}{1+\omega^2\tau_c^2} \tag{8}$$

Fig. 4 shows a plot of $J(\omega)$ as a function of the frequency ω for the three correlation times τ_c of 5, 10 and 20 ns. These correlation times represent the motion of small, medium and large globular proteins in solution. In addition, Fig. 4 illustrates that low frequency motions are especially effective in NMR relaxation processes for proteins. Using the concept of spectral density functions the different behaviour of longitudinal relaxation and relaxation of transverse magnetization can be rationalized. When considering only relaxation due to fluctuating dipolar interactions caused by stochastic motion, the relaxation rate T_1^{-1} is proportional to $J(\omega_0)$ since only stochastic magnetic fields in the transverse plane at the resonance frequency ω_0 are able to interact with the transverse magnetization components, bringing them back to the z axis. For frequencies larger than 25 MHz the values $J(\omega_0)$ decrease for the three increasing values of τ_c represented in Fig. 4. The longitudinal relaxation times, therefore, increase for increasing molecular weight of the protein. For very small molecules with very small τ_c the values $J(\omega_0)$ values get smaller again leading to an increase of T_1 compared to the value for a τ_c of 5 ns (Eq. (8)). The minimum T_1 value is obtained when $\omega_0\tau_c = 1$, e.g. at 600 MHz for a τ_c of 0.26 ns. Transverse relaxation shows a different dependence on the molecular weight of the molecule. T_2 relaxation not only depends on $J(\omega_0)$ but also on $J(0)$ since the z components of stochastic magnetic fields (zero frequency) reduce the phase coherence of transverse magnetization components which consequently sum up to a smaller macroscopic magnetization. Since $J(0)$ increases monotonously with

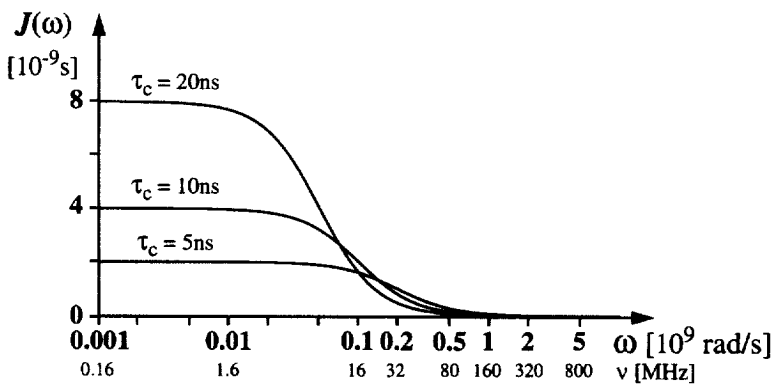

Fig. 4. Plot of the spectral density function $J(\omega)$ (Eq. (8)) versus the frequency ω on a logarithmic scale. Three correlation times 5, 10 and 20 ns are indicated which represent small, medium and large proteins. The frequency scale is given in units of rad s^{-1} and in MHz.

increasing correlation times (Eq. (8), Fig. 4) T_2 decreases monotonously with increasing molecular weight. Low T_2 values reduce the performance of NMR experiments with large molecules. However, relaxation depends not only on the size of a molecule but also on its internal motions. Two molecules with the same molecular weight may show quite different relaxation behaviour depending on their particular internal motions.

2.1.5. *Through-bond correlations*

The magnetic dipole–dipole interaction describes the effect of the local magnetic fields associated with the magnetic moments of surrounding nuclei. Two mechanism contribute to this effect: the "direct" (through-space) coupling and the "indirect" spin–spin coupling or J coupling transmitted via polarization of bonding electrons. The complete analysis of protein spectra is based on interactions between different spins, either mediated by electrons in through-bond correlations or by direct interactions through space. Through-bond correlations group individual spins into spin systems [15] which are characteristic for individual amino acids. In proteins couplings over more than three chemical bonds are not usually observed. Consequently, only spin systems for amino acid types can be obtained for unlabelled or ^{15}N-labelled proteins. The sequential arrangement of these spin systems relies on through-space correlations [5,6] which may be ambiguous for larger proteins. The efficiency of through-bond correlations depends on the size of the coupling constants involved. Heteronuclear coupling constants are often much larger than proton–proton couplings (Fig. 5). The use of heteronuclear coupling constants requires the protein to be labelled with ^{15}N and/or ^{13}C isotopes. With ^{13}C, ^{15}N doubly labelled proteins, spin systems of individual amino acid residues can be connected via J couplings across the peptide bond. Based on heteronuclear couplings a complete assignment can be obtained from through-bond correlations alone. Fig. 5 summarizes some typical coupling constants found for nuclei in proteins. A wide range of experiments for the determination of homo- and heteronuclear scalar coupling constants in proteins exists. An excellent survey of these methods can be found in a recent review [42].

Two principally different mechanisms for the through-bond correlation of spins are used. Either individual spin pairs are correlated or all spins in a spin systems interact simultaneously. The first case is often referred to as a COSY-type and the second as a TOCSY-type correlation. TOCSY stands for total correlation spectroscopy [43], also known under the acronym HOHAHA for homonuclear Hartmann–Hahn transfer [44]. Both types of correlation can transfer magnetization between two nuclei. Thus the sensitivity of a nucleus can be enhanced when the experiment starts with the polarization of a nucleus of a different species with a higher gyromagnetic ratio (Figs. 2 and 3). Polarization transfer based on a COSY-type sequence was given the acronym INEPT

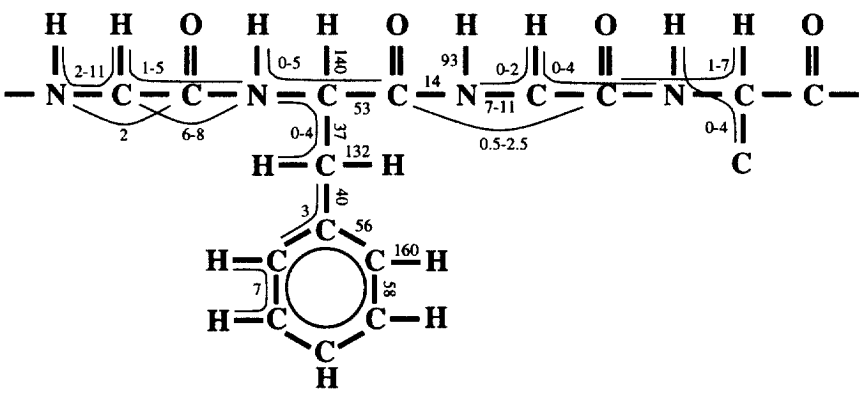

Fig. 5. Typical absolute values for coupling constants and their range in Hertz. If the variation is less than 10% of the maximal value, single average values are given, otherwise the range is indicated by the maximal and the minimal value. One-bond coupling constants are written along the bond; for multiple bond coupling constants a line drawn along the chemical bonds connects the two coupled nuclei.

[45] which stands for insensitive nuclei enhanced by polarization transfer. Polarization transfer based on a TOCSY-type sequence is usually referred to as an HEHAHA (heteronuclear Hartmann–Hahn) experiment (Section 4.2.3).

The COSY-type correlation can easily be rationalized using the product operator formalism for two scalar coupled spins I and S (Eq. (A.7) in Appendix B). Transverse I_y magnetization will evolve into anti-phase magnetization of the form $2I_xS_z$ due to scalar coupling. A 90° RF pulse with phase y on both spins transforms this operator product into $2I_zS_x$ which can evolve into the observable operator S_y. The crucial element in a COSY-type transfer is the 90° RF pulse acting on an anti-phase state. If the two nuclei belong to two different nuclear species the polarization transfer from spin I to spin S (Fig. 3) will change the sensitivity of the spin S by the ratio γ_I/γ_S of the gyromagnetic ratios.

In a homonuclear TOCSY-type transfer a strong RF field is applied to one nuclear species. Viewed in the rotating frame this field locks the spins along the axis it is applied. In this spin-locked state individual precession around B_0 is suppressed and replaced by a collective precession with the frequency of the applied RF field. Without their characteristic precession frequencies the spins lose their individuality and can no longer be distinguished and behave as part of a strongly coupled spin system. The product operator formalism cannot describe such a state and an analysis is only possible using a quantum mechanical treatment. A homonuclear two-spin system with scalar coupling J evolves under spin-locking for a period τ_m from the state I_x as follows [43]:

$$I_x \rightarrow I_x[1+\cos(2\pi J\tau_m)]/2 + S_x[1-\cos(2\pi J\tau_m)]/2 + [I_yS_z - I_zS_y]\sin(2\pi J\tau_m) \quad (9)$$

For $\tau_m = (2J_{IS})^{-1}$ complete in-phase magnetization transfer from I_x to S_x will occur. For more than two coupled spins different coupling constants will govern the transfer and complete transfer from one spin to another is usually not possible. The theoretical evaluation leading to Eq. (9) does not consider offset effects of RF pulses. When the effective fields for two nuclei are not aligned (Eqs. (A.3) and (A.4) in Appendix A) the effective J coupling during the mixing sequence is reduced resulting in a slower transfer. In addition to magnetization transfer through bonds, TOCSY mixing sequences transfer magnetization through space as discussed in the next section. This pathway requires special attention only for very sensitive nuclei such as protons and can safely be neglected for all other nuclei. Detailed descriptions of the foundations of the TOCSY experiment can be found in the literature with both experimental [46] and theoretical treatments [43,47].

In the more general case of the heteronuclear TOCSY, magnetization is transferred between nuclei of different species. In this situation two RF fields B_{1I} and B_{1S} at two different nuclear resonance frequencies have to be applied, with $B_{1I} = \gamma_I\omega_I$ and $B_{1S} = \gamma_S\omega_S$. As in the HOHAHA experiments the spins must experience the same magnetic field strength to lose their individuality and to form a strongly coupled system. Setting B_{1I} and B_{1S} equal produces the well-known Hartmann–Hahn condition [16,19,48] which must be fulfilled to obtain a heteronuclear TOCSY transfer:

$$\gamma_I\omega_I = \gamma_S\omega_S \quad (10)$$

If, for example, I stands for a ^{1}H and S for a ^{15}N nucleus the locking RF field applied to ^{15}N has to be almost 10 times larger than the one applied to protons (Table 1). Based on a quantum mechanical treatment the transformation properties of the operator I_x of a heteronuclear two-spin system submitted to a HEHAHA sequence can be formulated in analytical form [16,24]

$$I_x \rightarrow I_x[1+\cos(\pi J\tau)]/2 + S_x[1-\cos(\pi J\tau)]/2 + [I_yS_z - I_zS_y]\sin(\pi J\tau) \quad (11)$$

where J stands for the heteronuclear coupling constant between the spins I and S. For a full transfer of the magnetization in an HEHAHA experiment the mixing time τ_m must be $1/J_{IS}$ which corresponds to double the duration compared to the homonuclear transfer (Eq. (9)).

2.1.6. Through-space correlations

A nucleus with a spin different from zero generates a magnetic dipolar field proportional to its magnetic moment. As the molecule tumbles in solution, this field fluctuates and constitutes a mechanism of relaxation for nearby spins. Since the dipole–dipole

interaction involves a pair of spins, four states can occur for a system with two spins $\frac{1}{2}$. Due to the double and zero quantum transitions which are possible in such a system, the longitudinal relaxation process for the two spins I and S are coupled [49] and the expectation values $\langle I_z\rangle$ and $\langle S_z\rangle$ describing the z magnetization fulfil the equation

$$\mathrm{d}/\mathrm{d}t(\langle I_z\rangle - I_0) = -\rho_N(\langle I_z\rangle - I_0) - \sigma_N(\langle S_z\rangle - S_0) \quad (12)$$

$$\mathrm{d}/\mathrm{d}t(\langle S_z\rangle - S_0) = -\rho_N(\langle S_z\rangle - S_0) - \sigma_N(\langle I_z\rangle - I_0)$$

where ρ_N stands for the longitudinal relaxation rate constant of the two spins I and S of the same nuclear species, σ_N for the cross-relaxation rate constant and I_0 or S_0 are the equilibrium magnetizations. The coupling of the relaxation of the two nuclei will alter the magnetization of one spin when the other spin is not in its equilibrium state. For example, when the equilibrium value S_0 is selectively disturbed, leading to a deviation ΔS from S_0, then the I magnetization will change from I_0 with an initial rate proportional to $\sigma_N \Delta S$ (Eq. (12)). The following expression can be derived for σ_N and ρ_N using two spins of the same species without scalar coupling and with an internuclear distance r [50]:

$$\sigma_N = \frac{K}{r^6}(6J(2\omega_0) - J(0)) \quad (13)$$

$$\rho_N = \frac{K}{r^6}(J(0) + 3J(\omega_0) + 6J(2\omega_0)) \quad (14)$$

$$K = \left(\frac{\mu_0}{4\pi}\right)^2 \cdot \frac{h^2\gamma^4}{16\pi^2} \quad (15)$$

These expressions are valid in the case of isotropic tumbling and dipolar relaxation. σ_N can take positive or negative values depending on the value of the spectral density function in Eq. (8) (Fig. 4) and has a zero crossing (Fig. 6). For globular proteins measured at high magnetic fields σ_N is negative. For protons K equals 1.424×10^5 nm^6 s^{-2}. For example, in a globular protein with a rotational correlation time of 10 ns, σ_N becomes approximately 10 s^{-1} for two protons at a distance r of 0.2 nm and $\sigma_N = 0.04$ s^{-1} for $r = 0.5$ nm. Nuclear Overhauser enhancement (NOE) experiments make use of the cross-relaxation between spins and allow detection of nuclei which are close in space, in practice at a maximal distance of about 0.5 nm for protons in a globular protein. In a system with more than two spins, consecutive cross-relaxation can occur leading to so-called spin diffusion [51], where two distant spins exhibit a larger apparent cross-relaxation due to the contributions of the intervening spins. This effect complicates the derivation of distances from NOE measurements. Since the initial NOE is proportional to σ_N, spin diffusion becomes more important for larger proteins which exhibit a longer rotational correlation time τ_c (Fig. 6). Practical implementations exploiting cross-relaxation use the NOESY segment discussed in Section 4.2.2.

Based on the observation of cross-relaxation between I_z and S_z states, one may expect a similar effect with transverse magnetization. In general, a net magnetization transfer between transverse magnetization components does not occur because the spins precess with different frequencies and the continuously changing phase relationship between the

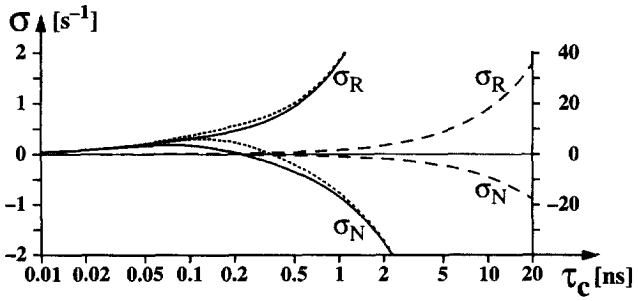

Fig. 6. Plot of cross-relaxation rates σ versus the rotational correlation time τ_c for a two-spin system. σ is given for the NOE in the laboratory frame denoted by σ_N and in the rotating frame, σ_R, for two spectrometer frequencies: 800 MHz indicated with solid lines and 500 MHz drawn with dotted lines. For these curves, the scale for σ on the left-hand side of the figure applies. The dashed lines show σ_N and σ_R on a 20-fold smaller vertical scale shown on the right-hand side. On this scale the curves for the two field strengths are indistinguishable. For the calculation, Eqs. (8), (13), (15) and (16) were used, assuming two protons with a constant internuclear distance of 0.2 nm.

corresponding magnetization vectors prevents the accumulation of a net transfer of magnetization. The situation changes when different spins are forced to precess at the same frequency by applying a strong RF field. With the individual precession frequencies removed, a net transfer can be established which couples the transverse relaxation process for two spins I and S. By analogy to the calculation of σ_N, a cross-relaxation rate constant, σ_R, and a relaxation rate constant, ρ_R, can be obtained [50,52]:

$$\sigma_R = \frac{K}{r^6}(2J(0) + 3J(\omega_o)) \tag{16}$$

$$\rho_R = \frac{K}{r^6}(5J(0) + 9J(\omega_o) + 6J(2\omega_o)) \tag{17}$$

The NOE between spin-locked transverse magnetization components is usually referred to as NOE in the rotating frame (ROE). Originally, the ROE experiment was called CAMELSPIN [53], but was later renamed ROESY for the two-dimensional ROE experiment [54]. Fig. 6 illustrates that the cross-relaxation rate σ_R does not have a zero crossing and that for molecules with a correlation time τ_c larger than 0.05 ns, σ_R is larger than σ_N. A detailed theoretical derivation of homonuclear cross-relaxation in the rotating frame can be found in an excellent review [52] and a number of textbooks, e.g. [16,24,26,50].

The ROE and TOCSY mixing sequences both use a spin-lock field to suppress the individual precession frequencies of transverse magnetization components and special care is required in the implementation to separate the two effects (Section 4.2.1). Although there are experimental implementations which minimize the simultaneous occurrence of both effects, a strict separation is not possible and both processes can contribute to correlations between scalar coupled nuclei. Nevertheless, ROE and TOCSY mixing sequences find widespread applications because the residual interference between them can, in many practical cases, be distinguished since the two effects generate signals with different signs.

Both the NOE and ROE enhancements for short mixing times are proportional to the cross-relaxation rate which for globular proteins is dominated by the spectral density function at zero frequency, $J(0)$, and therefore from Eqs. (13) and (16) $\sigma_R \cong 2\,\sigma_N$. This relation indicates that the ROE effect builds up signal with increasing mixing time twice as fast as NOE and in the opposite direction. When results from ROE and NOE spectra are to be directly compared, the mixing time for the ROE experiment is often chosen to be half as long as for the NOE experiment. Both ROE and NOE experiments not only detect cross-relaxation but also magnetization transfer by chemical or conformational exchange. Whereas the sign for the NOE and the ROE effect may be different, this is not the case for exchange contributions which always have an opposite sign compared to the ROE effect. This allows a separation of exchange contributions from NOE effects.

2.2. Radiofrequency pulses

2.2.1. Rectangular pulses

An NMR experiment consists of a series of RF pulses and delays, the pulse sequence, followed by the measurement of the voltage induced by the resulting magnetization in an RF coil (Section 3.5.1). A delay specifies a time period during which no external RF field is applied and the nuclear spin states evolve due to their intrinsic properties (chemical shift, scalar coupling and relaxation). A pulse represents a time period during which RF is delivered to the coil in the probe. Four parameters describe an RF pulse: frequency, phase, duration and strength. The frequency of the pulse is often called the carrier frequency since, generally, it is identical to the frequency used to demodulate the detected NMR signal. For a rectangular pulse the strength stays constant during its application. The magnetic field strength applied during such a pulse is often given in frequency units γB_1 which can be obtained with Eq. (3) by setting the pulse flip angle to 2π for a 360° pulse with the corresponding pulse length τ_{360}:

$$\frac{\gamma B_1}{2\pi} = \underline{\gamma} B_1 = \frac{1}{\tau_{360}} \tag{18}$$

For example, a 90° pulse with a duration of 12.5 μs is produced by a field strength γB_1 of 20 kHz.

Ideally, an RF pulse applied to a given nuclear species will rotate all magnetization components irrespective of their individual resonance frequencies by the same flip angle β about the axis in the rotating frame defined by the phase of the pulse. However, the performance of a real RF pulse degrades with

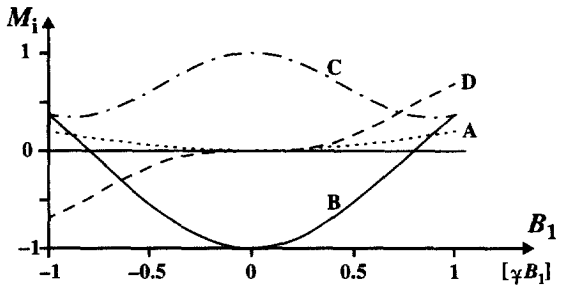

Fig. 7. Excitation profiles of RF pulses represented by the normalized magnetization M_i plotted against the offset given in units of γB_1 where B_1 is the applied field strength. (A) M_z after a 90° excitation pulse and (B) M_z after a 180° inversion pulse applied to z magnetization. (C) M_x after a 180° refocusing pulse with phase x applied to x magnetization. (D) Same as (C) but M_y is shown.

increasing offset of the nuclear precession frequencies from the applied RF frequency. The precession axis introduced by an RF pulse applied off-resonance deviates from the direction of the B_1 field of the pulse (see Appendix A). Whereas for a 90° excitation pulse satisfactory performance can be obtained over a wide bandwidth, the efficiency of a 180° pulse degrades rather rapidly. Fig. 7 shows excitation profiles for 180 and 90° pulses dependent on the offset frequency. Best use of these excitation profiles can be made when the carrier frequency sits in the middle of the spectral range of interest. A 90° pulse applied to z magnetization brings most magnetization into the transverse plane when the offset frequency ν_{off} fulfils the condition $\nu_{off} < \gamma B_1$. However, the magnetization acquires an offset dependent angle ε to the direction it would reach after an ideal 90° pulse with duration τ_{90}. This angle ε can be calculated to be $4\tau_{90}\nu_{off}$ in units of radians [16,24,26].

A further consequence of the non-ideal behaviour of RF pulses is specific offset frequencies at which the pulse does not perturb the resonances. This feature can be used to excite one group of resonances while selectively avoiding excitation of another group, a technique that finds frequent applications in heteronuclear experiments involving carbon nuclei, where carbonyl carbons and aliphatic carbons are excited separately. Using the Bloch equations (see Appendix A) the kth null in the excitation profiles can be calculated for a 90° pulse with duration τ_{90} to be at a frequency ν_{90} and for a 180° pulse with duration τ_{180} at a frequency ν_{180} from the carrier frequency:

$$\nu_{90} = \pm \left(k^2 - \frac{1}{16}\right)^{1/2} / \tau_{90} \tag{19}$$

$$\nu_{180} = \pm \left(k^2 - \frac{1}{4}\right)^{1/2} / \tau_{180} \tag{20}$$

For a 90° pulse the first null is at $\nu_{90} = \pm 0.97/\tau_{90}$ and for a 180° pulse at $\nu_{180} = \pm 0.87/\tau_{180}$.

Typically, several 180° pulses occur in a pulse sequence and the signals created by their non-ideal behaviour may limit the spectral quality. With a phase cycling scheme, EXORCYCLE [55], magnetization components not inverted by the 180° pulse and those which underwent a coherence transfer due to off-resonance effects can be removed from the detected signal. The EXORCYCLE consists of a four-step phase cycle where the phase of the 180° pulse changes according to the scheme x, y, −x, −y together with the receiver phase cycling through x, −x, x −x.

Many applications require the inversion of z magnetization. In this case simple composite pulses exhibit much broader inversion profiles than a single 180° pulse. A composite pulse based on a 180° pulse with phase y embraced by 90° pulses with phase x, in short notation $90_0\,180_{90}\,90_0$, shows more than 80% inversion over a bandwidth of $\pm \gamma B_1$ [56]. The composite pulse $90_0\,225_{90}\,90_0$ where the 180° pulse is replaced by a 225° pulse results in even better inversion of more than 98% but at the cost of a smaller bandwidth of $\pm 0.7\gamma B_1$. Analogous simple composite pulses for improved refocusing of transverse magnetization do not exist [57].

When pulses or more complex pulse trains with low power are applied selectively to only a small frequency range in a spectrum, the signals at an offset $\Delta\nu$ far from the irradiation frequency can still be significantly affected. These off-resonance or non-resonant effects can lead to a phase shift ϕ_{nr} and a rotation ρ of the evolving magnetization and depend on the strength $\nu_2(t) = \gamma B_2(t)$ of the applied magnetic field $B_2(t)$ [34,35]. The rotation ρ is towards the positive z axis around an axis perpendicular to the axis along which the RF pulse is applied. Both ϕ_{nr} and ρ depend on the length τ_p of the pulse train applied and on the average of the square of the field strength,

$\langle\nu_2^2(t)\rangle$. In addition, ρ is proportional to the average of the field strength:

$$\phi_{nr} = \pi\langle\nu_2^2(t)\rangle\tau_p/\Delta\nu \tag{21}$$

$$\rho = \pi\langle\nu_2^2(t)\rangle\langle\nu_2(t)\rangle\tau_p/(\Delta\nu)^2 = \phi_{nr}\langle\nu_2(t)\rangle/\Delta\nu \tag{22}$$

In these equations ϕ_{nr} and ρ are given in units of radians. Eqs. (21) and (22) exhibit clear differences between ρ and ϕ_{nr}. The rotation ρ is always smaller than the phase shift ϕ_{nr}, and when the average strength of the applied field $\langle\nu_2(t)\rangle$ is zero, then the rotation ρ, but not ϕ_{nr}, vanishes completely, a situation encountered with composite pulse decoupling where $\langle\nu_2(t)\rangle = 0$ due to the applied phase cycling schemes. A typical numerical example relates to the decoupling of alpha carbon resonances from carbonyl carbons which are separated by $\Delta\nu = 18\,000$ Hz on a 600 MHz NMR spectrometer. The application of an 8-ms-long, low-power WALTZ decoupling sequence to carbonyl carbons using a 1 kHz decoupling field strength results in $\phi_{nr} = 1.4$ rad (80°) and $\rho = 0$. Using instead of WALTZ a rectangular 180° pulse at the carbonyl frequency with its sixth null at 18 000 Hz (Eq. (20)) to refocus the effect of the carbonyl couplings, the values change to $\phi_{nr} = 0.13$ rad (7.5°) and $\rho = 0.6°$.

In the course of a multidimensional NMR experiment selective decoupling may be applied during an evolution time which is incremented. In this situation τ_p increases linearly and considering Eq. (21) it becomes clear that the time-dependent phase ϕ_{nr} will manifest itself as a frequency shift ν_{nr}:

$$\nu_{nr} = \langle\nu_2^2(t)\rangle/2\Delta\nu \tag{23}$$

With the numerical example given above using WALTZ decoupling, the frequency shift ν_{nr} becomes 27.8 Hz. The numerical examples show that the non-resonant effects described by ϕ_{nr} and ρ may cause severe signal loss and care has to be taken to correct for their influence. Four different procedures can be envisaged to compensate for non-resonant effects [35]:

1. Adjusting the phase and flip angle of the pulse directly following or preceding the occurrence of non-resonant effects.
2. A phase error occurring during an evolution time can be corrected by applying a phase correction after Fourier transformation.
3. Compensation by modulating the amplitude of the pulse train with a cosine function which results in the application of the disturbing field at $+\Delta\nu$ and $-\Delta\nu$, thereby cancelling the effects at the frequency of interest.
4. Applying the disturbing field twice, once before and once after a non-selective 180° pulse and thereby refocussing the adverse effects.

2.2.2. *Amplitude-modulated pulses*

Modulating the amplitude of a pulse permits the design of specific excitation profiles. Since the shape of a pulse and its excitation profile are not related by a Fourier transformation [16], more elaborate procedures must be used to find the optimal pulse shape based on a desired excitation profile. A large selection of pulse shapes have been developed and characterized [58]. From a given pulse shape the excitation profile can be calculated by integrating the Bloch equations given in Appendix A. Software packages on commercial spectrometers include corresponding routines (Bloch simulator) which help to choose the appropriate shape for a specific experiment and to determine its parameters. In general, a good amplitude-modulated pulse should have an adequate frequency selectivity, uniform excitation, uniform phase behaviour and a short duration. Some of these desired properties contradict each other. Improving the selectivity, for example, tends to increase the pulse duration which should be kept as short as possible to counteract relaxation losses. During the application of a selective pulse, the magnetization components of interest accumulate an offset-dependent phase error. If the phase error is approximately linear across the excitation bandwidth it can be refocused by a non-selective 180° pulse after a suitable delay within or after the selective pulse [59]. Far from its irradiation frequency, a selective pulse may introduce non-resonant phase and amplitude errors as described by Eqs. (21) and (22). These deficiencies can be corrected using the same methods as described for rectangular pulses in Section 2.2.1.

The performance of an amplitude-modulated pulse depends on the initial state of the magnetization. A selective 180° pulse that provides good inversion properties for longitudinal magnetization in general does not perform well as a 180° refocusing pulse for

transverse magnetization. For this reason, some shapes of pulses, for example the BURP pulses [60], are grouped into families with a member for excitation, inversion and refocusing. The most frequently used shaped pulses are Gaussian, sinc with no or one pair of side lobes, Gaussian cascades [61] which are based on individual Gaussian-shaped pulses, and pulses of the BURP family [60].

The application of amplitude-modulated pulses in a pulse sequence requires all stages of the transmitter pathway of the spectrometer to be linear, otherwise the shape and hence the excitation profile deviate from the one selected. The direct determination of the pulse length of an amplitude-modulated pulse can be rather tedious. In this situation the use of a Bloch simulator program which integrates the Bloch equations (Eq. (A.1)) seems more efficient for the determination of the parameters of a shaped pulse by using the known parameters of a rectangular 90° pulse to determine the field strength of a given power setting. A prerequisite for such calculations is the linearity of the transmitter channel. In addition, amplitude-modulated pulses can be rather sensitive to RF inhomogeneity of the coil in the probe and therefore require good RF homogeneity for best performance.

2.2.3. Amplitude- and phase-modulated pulses

A pulse excites a spectral range around its irradiation frequency. However, some experimental techniques require the pulse to excite at a frequency different from this position. For example, in the middle of a period of free precession a selective 180° pulse may need to be applied to the amide protons to decouple them from the alpha protons. If the carrier is to remain on the water resonance, this requires a homonuclear off-resonance selective pulse. Off-resonance pulses have the advantage over switching the carrier frequency in that the latter method generates a phase shift which must be taken into account and complicates the phase setting of subsequent pulses applied to the precessing magnetization. The centre of excitation of a pulse cannot only be changed by changing its frequency but also by changing its phase during the application. Two types of phase-modulated pulses can be distinguished: pulses shifted off-resonance by a fixed frequency and pulses where the frequency is swept during their application. A pulse with a fixed off-resonance frequency shift ν_{off} during the application can be obtained by linearly increasing the pulse phase $\Phi(t)$ with time while keeping the carrier frequency fixed at ν_o:

$$\cos(2\pi\nu_o t + \Phi(t)) = \cos(2\pi\nu_o t + (\Phi_o + 2\pi\nu_{off} t)) \tag{24}$$

The increment per unit time depends on the required offset frequency ν_{off} from the carrier frequency ν_o. A positive phase increment will shift the frequency to higher values, decrementing the phase lowers the effective frequency of the pulse. For example, amide protons or carbonyl carbons resonate at a higher absolute frequency than methyl resonances of protons or carbons, respectively. The time point $t = 0$ sets the reference phase Φ_o for the off-resonance pulse. Any further pulse on transverse magnetization of the same nuclear species during the pulse sequence at a later time point T will have the phase $\Phi(T)$ which in general deviates from Φ_o. The performance of pulses which invert z magnetization will usually be independent of $\Phi(T)$. However, off-resonance pulses that create or act on transverse magnetization require the phase $\Phi(T)$ to be adjusted properly, otherwise signal may be lost. $\Phi(T)$ can be calculated on the basis of Eq. (24) and, for example, the proper time chosen where $\Phi(T) = \Phi_o$.

When the phase $\Phi(t)$ in Eq. (24) depends nonlinearly on the time t, the effective frequency changes during the pulse. An important group of pulses using frequency sweeps during their application are the adiabatic pulses. These pulses excite, invert or refocus magnetization over a very wide frequency range at the cost of a longer pulse duration and a phase dispersion across the excitation bandwidth. In applications where such pulses excite or invert magnetization, they are robust to RF inhomogeneities but not when applied for refocusing [62]. An additional feature makes adiabatic pulses very attractive: doubling the RF field strength of the pulse quadruples the bandwidth covered [62]—a distinct advantage over conventional pulses which excite a bandwidth proportional to the strength of the pulse.

The concept of adiabatic pulses can be understood with the help of a description in the rotating frame. With the applied radiofrequency field B_1 far above resonance, the effective field B_{eff} corresponds to the residual magnetic field B_z (Eq. (A.3) and Fig. 38 in Appendix A) and the magnetization M stays aligned

along the positive z axis. Sweeping the frequency of B_1 towards resonance will tip B_{eff} away from the z axis towards the transverse plane. For a sufficiently slow sweep the magnetization M stays aligned with the changing direction of the effective field. At resonance, B_{eff} and M lie in the transverse plane. As the frequency of the exciting field B_1 passes through resonance and is subsequently swept to frequencies much lower than resonance, the magnetization M moves on towards the negative z axis (Eqs. (A.3) and (A.4)). For M to follow B_{eff} the adiabatic passage condition must be fulfilled [29]:

$$|d\Theta/dt| \ll \gamma B_{eff} \text{ with } B_{eff} = \left(B_1^2(t) + B_z^2(t)\right)^{1/2} \quad (25)$$

where B_z represents the offset from the resonance frequency and Θ describes the angle between the effective field and the z axis (Eq. (A.4)). With Eqs. (25) and (A.4) one finds that the critical stage of any adiabatic sweep is the point where B_1 sweeps through resonance for a given magnetization component resulting in the relation

$$dB_z(t)/dt \ll \gamma B_1^2(t) \quad (26)$$

In addition to the condition described in Eq. (26), adiabatic passage requires that no relaxation occurs during the sweep period. In practical implementations the field cannot be swept starting at an infinitely large offset; however, when choosing a finite starting value the effective field and the magnetization M are not aligned. Consequently, M precesses around B_{eff} which degrades the performance of adiabatic pulses. To reduce this initial precession the starting angle Θ_o must be as small as possible. For small values of Θ one finds with Eq. (A.4)

$$\Theta = B_1/B_z \quad (27)$$

Based on Eq. (27) small values of Θ require large initial offsets for the start of the sweep. For an angle Θ corresponding to 1° (0.0175 rad) and with $\gamma B_1 = 2$ kHz, an offset of at least 115 kHz is necessary. Eq. (27) suggests an alternative approach to reduce the initial offset substantially. If the sweep starts with an amplitude of B_1 at zero and is smoothly increased to its nominal value, then the offset where the sweep must start can be reduced, making adiabatic sweeps more efficient [62]. The same consideration for the end of the adiabatic sweep leads to the conclusion that the amplitude of B_1 should be smoothly reduced to zero.

As long as Eq. (26) stays fulfilled, the time-dependent phase $\Phi(t)$ of the pulse can have any functional form. For simplicity, very often linear sweeps are applied (Eq. (28)). With the total sweep range F and the total duration of the sweep τ_s, the change of B_z per unit time (dB_z/dt) becomes $2\pi F/\gamma\tau_s$. Linear sweeps result in a quadratic time dependence for the phase $\Phi(t)$ of the constant frequency ν_o during the application of an adiabatic pulse:

$$\cos(2\pi\nu_o t + \Phi(t)) = \cos(2\pi\nu_o t + (\Phi_o + (2\pi F/\gamma\tau_s)t^2)) \quad (28)$$

Most applications of adiabatic pulses use single inversion pulses or trains of inversion pulses in decoupling sequences. When used to refocus transverse magnetization, their inherent long execution time may cause problems with fast relaxing magnetization as well as with evolution due to scalar couplings which may modulate the signals. On the other hand, depending on the chemical shift range of scalar coupled nuclei, partial decoupling may be achieved during the adiabatic pulse [63,64]. Applications for refocusing are not yet very common, but their applicability has been demonstrated [63,65,66].

2.3. Magnetic field gradients

Pulsed magnetic field gradients (PFGs) have been used in NMR spectroscopy for more than thirty years to study the diffusion of molecules in solution [67,68]. However, PFGs became a routine tool in high-resolution NMR in solution [69–73] only since the introduction of actively shielded gradient coils which offer short recovery times (Section 3.5.2) for the re-establishment of the very homogeneous magnetic field after the application of a PFG. The resonance frequency of nuclei placed in a magnetic field gradient becomes dependent on their spatial location. A linear PFG with the strength G per unit length along the z direction produces the following dependence of the resonance frequency $\omega(z)$ on the z coordinate

$$\omega(z) = \omega_o + \gamma G z \quad (29)$$

where ω_o is the resonance frequency without the application of a PFG. The evolution of the operators

used to describe an NMR experiment (Section 2.1.2) becomes dependent on the vertical position in the sample. Using the shift operator basis the following transformations are obtained due to the action of a gradient pulse applied for a duration τ:

$$I^- \rightarrow I^- \, e^{i\gamma Gz\tau} \tag{30}$$

$$I^+ \rightarrow I^+ \, e^{-i\gamma Gz\tau}$$

$$I_z \rightarrow I_z$$

In these transformation rules the evolution due to chemical shift and J coupling are not included. The phase factor γGz describing the spatial dispersion of the resonance frequencies depends on the gyromagnetic ratio γ which makes the action of a gradient less efficient for nuclei with a small γ. For example, applying an identical gradient on transverse proton and nitrogen magnetization will result in a spread of resonance frequencies across the sample which is 10 times larger for proton than for nitrogen nuclei. Eq. (30) describes how the evolution of magnetization components depends on the z coordinate. However, the magnitude of the macroscopic magnetization M will be the integral over the sample length L which results in the following relationship

$$M = \frac{\sin(\gamma G\tau L/2)}{\gamma G\tau L/2} = \mathrm{sinc}(\gamma G\tau L/2) \tag{31}$$

The sinc function in Eq. (31) has a damped oscillatory behaviour and is zero only at specific values. In between the zero crossings the detectable signal can reach appreciable values and can interfere with the performance of the experiment requiring the value for $\gamma G\tau L$ to be optimized. For example, a moderate gradient with a duration of 1 ms and a strength of 0.1 T m^{-1} applied to proton magnetization using a typical commercial probe will show a maximum signal recovery between the first and second zero crossing of about 0.5% of the original intensity which, for example, results in a substantial residual signal for the solvent resonance.

Pulsed magnetic field gradients find three main applications: (i) spatial encoding of coherences, (ii) elimination of unwanted coherences and (iii) selection of coherences. Whereas point (i) has already been used in diffusion measurements for a long time, points (ii) and (iii) have become increasingly important in high-resolution NMR spectroscopy only in recent years replacing or supplementing phase cycling schemes for the selection of a specific coherence transfer pathway (Fig. 1). Eq. (30) illustrates the basic principle used. Every application of a PFG introduces a phase factor of the form $\gamma Gz\tau$. For the desired coherence pathway the sum of all these phase factors must be zero. All other pathways do not result in detectable signal if sufficiently strong gradients are used (Eq. (31)). For multiple quantum coherence every operator in the product will evolve according to Eq. (30). Consequently, the sensitivity of the precession frequency of a coherence to magnetic field gradients will be proportional to its order. Thus homonuclear double quantum coherence will be twice as sensitive to magnetic field gradients as single quantum coherence, while homonuclear zero quantum coherence will be unaffected. For heteronuclear multiple quantum coherences, the different gyromagnetic ratios have to be taken into account (Eq. (30)). The application of gradients has the potential to select the desired signal in one scan in contrast to phase cycling which requires the repetition of the experiment and the subtraction of unwanted signals. Unfortunately, only half the signal defocused by a gradient can be refocused if a 90° RF pulse is applied between the two gradients. This drawback can be verified using Eqs. (A.9) and (30). Such a signal loss constitutes a common feature when gradients are used for pathway selection. As discussed in Section 4.5.3, experimental techniques exist for some cases that prevent this signal loss. Further signal losses can occur due to diffusion losses. In between the defocusing and refocusing gradients, the molecules with the nuclei diffuse to a different location preventing a complete refocusing (Eq. (51)). Diffusion losses are largest for small molecules, particularly the solvent magnetization.

Magnetic field gradients can also be applied in the form of spatially inhomogeneous RF pulses [74,75], either using the inherent RF inhomogeneity of the transmitter coil or using a separate coil designed to deliver inhomogeneous B_1 fields [76]. The first method is frequently used in the form of spin-lock purge pulses which destroy magnetization components that are not aligned along the axis defined by the phase of the RF pulse [77]. The second more efficient method requires special hardware and has not yet found many applications. Radiofrequency

gradients possess the inherent advantage over static pulsed magnetic field gradients that they can be applied frequency selective [78]. On the other hand, limitations arise due to RF heating effects and the rather modest maximal strength for RF gradients which typically is limited to 0.1 T m^{-1}.

2.4. Data acquisition

2.4.1. Digitizing the signal

At the end of a pulse sequence the free induction decay (FID) of the magnetization of one nuclear species is measured. The sensitivity of the detection is proportional to $\gamma^{3/2}$ (Eq. (50)), and whenever feasible the magnetization should be transferred to and detected on the nuclear species with the largest gyromagnetic ratio. This procedure requires an efficient coupling between the different species of nuclei to retain the sensitivity advantage, despite the inevitable signal losses during the transfer. When working with macromolecules in solution, the proton constitutes the preferred nucleus for detection. However, irrespective of the nuclear species detected, the resonance frequency is tens or hundreds of megahertz, whereas the difference of resonance frequencies of one particular nuclear species in different environments, the chemical shift range, is very small, often only a few kilohertz. Technically speaking, a high frequency, the carrier frequency, is modulated by low frequency signals which represent the spectrum of interest. By subtracting the carrier frequency from the signal, one obtains a modified signal that contains only frequencies between zero and a few kilohertz. Spectrometers use frequency mixing schemes to transform the high resonance frequencies to a lower frequency range since the necessary high dynamic range digitizers exist only up to frequencies of a few hundred kilohertz. In addition, a quadrature detection scheme (Section 3.3.1) delivers two signals which are 90° out of phase, which allows discrimination between positive and negative frequencies with respect to the carrier frequency. The carrier frequency and the frequency of the RF pulses on the observe channel are usually identical and consequently quadrature detection enables the user to place the carrier in the middle of the spectrum resulting in a more efficient excitation of the resonances (Fig. 7). The low frequency analog signal thus obtained is digitized at equidistant time points and stored on a computer.

The sampling theorem [79] specifies that for the representation of the analog signal in digital form, the sampling rate of the digitizer must be at least twice the highest frequency in the signal. With a quadrature detection system the highest frequency in the spectrum is half the spectral range covered by the signals. In other words, the time increment, the dwell time Δ, between two digitized points must be equal to or smaller than the inverse of the sweep width $2\nu_N$ which covers the frequency range from $-\nu_N$ to $+\nu_N$ with the carrier frequency being at zero frequency. Slower sampling results in folding of the signals with absolute frequencies larger than ν_N into the spectral range of interest. The folded signals will be represented by an incorrect frequency and in general will have a phase that differs from that of unfolded signals. One-dimensional ^{1}H NMR spectra of proteins contain a very large number of resonances and folding of additional signals into the spectral range is not desired. This is in contrast to multidimensional experiments where folding quite frequently can be tolerated and helps to reduce the spectral range in additional dimensions.

The data can be digitized with two different sampling techniques. The first method digitizes the two quadrature channels simultaneously and delivers data points that can be regarded as complex numbers. This simultaneous digitization method simply measures the orthogonal components of the precessing magnetization which correspond to the two quadrature channels. The minimal sampling rate $1/\Delta$ becomes equal to the sweep width $2\nu_N$ and a complex Fourier transform of the FID produces the spectrum. The second method digitizes the two quadrature channels sequentially with a sampling rate of $4\nu_N$. Consequently, two time-shifted signals are measured and correct processing requires that every second data point pair must be inverted in sign before the signal is submitted to a real Fourier transformation, resulting in the spectrum [80]. The sequential digitization can be understood using the concept of the rotating frame of reference at the carrier frequency (Fig. 38 in Appendix A). Including the effect of the sign inversion, the sampling method corresponds to a sequential sampling of the magnetization components along the x, y, −x, −y, x, y, −x, ... axis in the rotating frame.

From one digitized point to the next, the axis along which the magnetization is sampled rotates by 90° about the z axis instead of being static as with simultaneous digitization. In other words, the reference frame for detection rotates within two dwell times by 360° with respect to the carrier frequency which corresponds to a frequency shift of ν_N. Consequently, the zero frequency shifts from the middle to the edge of the spectrum and all resonance lines have a frequency larger than zero which lies between 0 and $2\nu_N$. This detection scheme is based on a linear phase incrementation with time and is referred to as the TPPI method which stands for time proportional phase incrementation [80,81].

The requirement for a constant dwell time and the sampling theorem are consequences of the Fourier transformation method used to obtain the spectrum from time domain data. Other transformation methods permit varying dwell time lengths. In general, time periods in the FID which have better signal-to-noise (S/N) ratios should be sampled more frequently than those with less S/N. Different sampling schemes were proposed in combination with maximum entropy reconstruction for the transformation into the frequency domain [82–84]. Considering the modest benefits obtained, these procedures do not seem to be justified in most applications due to the increased complexity involved in the data collection, transformation, and sensitivity to parameter settings. Currently, equidistant sampling is by far the most frequently used scheme.

2.4.2. *Handling the water resonance*

Many NMR measurements with biological macromolecules rely on the presence of exchangeable protons in the molecules and must therefore be performed in H_2O solutions which contain only a small amount of D_2O for the field–frequency lock (Section 3.3.3). Measuring the spectrum of a protein dissolved in H_2O at a typical concentration of 1 mM requires a dynamic range of the spectrometer which cannot be obtained without the reduction of the signal intensity of the water. Numerous techniques for the reduction of the intense solvent line have been developed and a number of excellent reviews on these techniques exist, e.g. [21,85]. Here only a few selected techniques can be mentioned. When 2D methods were first developed it was a real challenge to obtain spectra from H_2O solutions and initial success was achieved by presaturation of the water resonance [86]. Later, spin-lock pulses were introduced which destroy the water magnetization due to the spatial RF field inhomogeneity during the pulse [77]. Unlike solvent presaturation, which happens during the relaxation delay, spin-lock pulses occur later in the sequence allowing the water to recover during the relaxation delay and reducing the degree of saturation of the water magnetization. This enhances the signal intensities of exchangeable protons of the protein, for example for the amide protons which play an important role for many experimental schemes. Magnetic field gradients act in a very similar way to spin-lock pulses; however, better suppression can often be obtained [69,70,87]. Work at higher pH demands an even better conservation of water polarization due to the faster exchange rates of labile protons, and methods were developed that attempt to conserve the equilibrium water magnetization during the pulse sequence and flip the water back to the positive z axis before the start of the acquisition [88].

The huge magnetization of water exhibits special behaviour after the excitation by an RF pulse. The magnetization of water rotates back to the positive z axis much faster than expected from relaxation. The large signal induced in the receiving coil during precession of the water magnetization creates a magnetic field that acts on the water resonance like a shaped RF pulse and rotates it back to the z axis. This effect, known as radiation damping, may interfere with the performance of experiments where the water resonance cannot be destroyed, for example when studying interactions between water and protein protons (Section 5.3). When using water flip-back methods [88,89] the H_2O resonance should never be aligned with the negative z axis just prior to acquisition because radiation damping can efficiently rotate the water magnetization into the transverse plane which can overload the receiver system during acquisition. The strength of radiation damping is proportional to the size of the water magnetization and the quality factor of the probe. Consequently, it becomes a more serious problem with high magnetic field strengths and higher sensitivity probes. Different techniques have been developed to suppress radiation damping during a pulse sequence without destroying the water resonance. Using pulse field gradients the

water can be defocused during periods of free precession and refocused just before the next pulse which is different from 180° [90]. This procedure conserves the water magnetization except for diffusion losses which must be minimized. Another method temporarily reduces the quality factor Q of the receiving coil and therefore decreases the current induced in the coil and hence the radiation damping effect [91]. This technique requires special circuitry in the probe known as a Q switch, which allow rapid changes in the Q value. A third method uses an active feedback loop driven by the detected water magnetization. Such a device sends very weak RF pulses to the coil counteracting the radiation damping effect. In this way, the state of the water magnetization can actively be controlled and suppression as well as an enhancement of the radiation damping effect can be obtained [92,93].

The very large polarization of water not only interferes with the water resonance itself but slightly alters the main static magnetic field which changes the resonance frequencies of all nuclei. This demagnetizing field effect amounts to a fairly small change of the main magnetic field of about 1.5 Hz for protons at 750 MHz when the water magnetization is switched from the positive z axis to the negative z axis. None the less, difference experiments such as hydration experiments may exhibit subtraction artefacts and suffer losses of performance due to these small field changes [94,95] (Section 5.4).

2.4.3. Decoupling during acquisition

During acquisition of the signal, scalar coupling between nuclei splits the resonance line into different components. Often it would be preferable to decouple the individual nuclei from each other to obtain the best sensitivity and the minimum number of lines. For different species of nuclei, decoupling is usually straightforward. For example, protons attached to ^{15}N nuclei in labelled proteins can be decoupled from the ^{15}N nuclei by continuous inversion of the magnetization of all the ^{15}N nuclei during acquisition of the proton signal without adverse effects on the measured spectrum. Practical consequences and limitations of heteronuclear decoupling will be discussed in Section 4.3.

Decoupling nuclei of the same species from each other requires more elaborate schemes and, of course, the decoupled nuclei cannot be directly detected. Homonuclear decoupling requires RF irradiation at the receiving frequency which in turn requires that the preamplifier (Section 3.3.1) is switched off during the period of irradiation. The total dwell time, DW_t, is split into a period where the preamplifier is turned off and a period where the signal is received, DW_r. This time sharing reduces the measured signal since the receiver can integrate the signal only during the time DW_r. Switching off the preamplifier reduces not only the signal by a factor DW_r/DW_t but simultaneously the noise proportional to $(DW_r/DW_t)^{1/2}$. For the signal-to-noise with homonuclear decoupling $(S/N)_{hd}$ one obtains the reduction

$$(S/N)_{hd} = (DW_r/DW_t)^{1/2}(S/N) \tag{32}$$

where S/N is the signal-to-noise ratio without decoupling. For example, using half the dwell time for homo-decoupling including the necessary switching delays of the hardware reduces $(S/N)_{hd}$ by $\sqrt{2}$ compared to that obtainable without decoupling. Instrumental limitations may reduce the obtainable $(S/N)_{hd}$ further. Not only decoupling but any disturbance which interferes with the integration of the signal reduces the sensitivity, for example when applying defocusing and refocusing gradients during the acquisition of the signal [96].

2.4.4. Oversampling and digital filtering

Before the signal reaches the digitizer the spectral bandwidth must be limited by a suitable analog filter to the frequency range (sweep width) selected. Otherwise higher frequency noise folds into the spectral region of interest and reduces the obtainable S/N. Such analog filters introduce a frequency-dependent retardation of the signals and show transient oscillations after a sudden change of the voltage which typically happens at the start of the FID. This characteristic behaviour can result in baseline distortions in the spectrum and the necessity of first-order phase correction which itself introduces baseline curvature [97–99]. The distortions in the spectrum due to the filters can be minimized by judicious choice of the time at which the receiver opens and the first data point is sampled [100]. Spectrometers do start accumulation according to this scheme but the appropriate delays usually require fine adjustment for best performance. Use of analog filters presents somewhat

of a dilemma; on the one hand, analog filters introduce distortions which increase with the steepness of the frequency cutoff of the filters; on the other hand, the filter should be as steep as possible for efficient suppression of signals and noise outside the chosen sweep width. This dilemma can be overcome with oversampling when the digitized frequency range is much larger than the one finally desired. Oversampling allows the use of analog filters with a much broader transition frequency range between full passage and full attenuation. Such filters have short filter delays and negligible transient oscillations which reduces their detrimental effects on the baseline of the acquired spectrum [101]. The analog narrowband filters with steep cutoffs for the adjustment of the final spectral range can then be replaced by digital filters. Special digital signal processors are programmed to apply very steep filters without introducing baseline distortions. The digital signal processors are inserted between the digitizer and the computer memory which stores the data so that the storage requirements of oversampled data do not exceed the space used by conventionally acquired data. Oversampling provides a further advantage by increasing the dynamic range of the digitizer [102]. The extra bits n obtained with oversampling can be calculated from the following expression

$$n = \log_2(SW_{ov}/SW)/2 \quad (33)$$

where SW_{ov} is the oversampled frequency range, SW the desired spectral range and the logarithm is base 2. For example, with SW = 10 kHz and SW_{ov} = 160 kHz the effective dynamic range of a 16 bit digitizer corresponds to 18 bits.

The quadrature detection scheme used in spectrometers (Section 3.3.1) requires a phase difference of exactly 90° and identical amplification in the two signal paths which, in practice, cannot be achieved. As a consequence, positive and negative frequencies with respect to the carrier cannot be completely separated, leaving typically less than 1% of the wrong signal as a quadrature image on the wrong side of the carrier frequency. Still, these signals may have a detrimental effect in multidimensional NMR spectra which contain resonances with widely different signal intensities. The images can usually be suppressed beyond detection by exchanging the signal pathways in subsequent scans which are added [97]. This cancellation method requires simultaneous changing of the phases of all RF pulses and the receiver by 90° between scans. When this procedure is extended to a four-step phase cycle using the phases 0, 90, 180 and 270° it is called CYCLOPS [103]. In addition to the quadrature images, CYCLOPS suppresses the spike at zero frequency which is caused by different DC offsets in the two receiver channels. When the carrier is set on-resonance with H_2O the original two-step phase cycle suffices since the water resonance usually causes a distortion at zero frequency which is much larger than the zero frequency spike. Modern spectrometers use a different scheme, sometimes referred to as digital quadrature detection. In this scheme the signal is mixed to a low frequency range which does not contain zero frequency. A narrow bandpass filter programmed into the digital signal processor used to reduce oversampled data then selects the desired spectral range which does not contain quadrature images. The technique produces spectra which cannot contain quadrature images and hence renders CYCLOPS unnecessary which reduces the phase cycling schemes, a definite advantage in multidimensional NMR spectroscopy where phase cycles may be longer than necessary to obtain sufficient signal-to-noise, causing unnecessarily long experiment times.

2.5. Multidimensional NMR

Multidimensional NMR was first proposed in 1971 [3] and the first applications were published a few years later [4]. A multidimensional data set depends on different time variables which can be transformed into multiple frequency domains. For the introduction of an additional time variable, a suitable delay during the pulse sequence, the evolution time, is incremented during the experiment [16,40,104]. Only during the last time period is the signal physically acquired which is thus often referred to as the direct dimension, in contrast to all other dimensions referred to as indirect dimensions. The magnetization measured depends on the evolution times during the pulse sequence and this dependence is reflected by a change in amplitude and/or phase of the acquired signal. A typical n-dimensional NMR experiment follows the scheme

$$\text{excitation–(evolution–mixing)}_{n-1}\text{–detection} \quad (34)$$

where the bracket repeats $(n-1)$ times. In a simple example the excitation just consists of a 90° pulse and the single mixing could be another 90° pulse which mixes the non-equilibrium states obtained after the first pulse and the evolution time. This sequence is usually referred to as a COSY experiment [3,4]. The sampling of frequencies in evolution periods must fulfil the same requirements with respect to folding and the sampling theorem as the measurement of the FID in the detection period. A subsequent n-dimensional Fourier transform provides an n-dimensional spectrum that depends on n frequency variables. If two nuclei suitably interact with each other in a mixing time between two evolution periods or between the last evolution time and the detection period, this interaction will be manifested by a resonance in the spectrum, a cross-peak, at a position characterized by the precession frequencies of the interacting nuclei. Nuclei that did not have any interaction in the mixing time will show the same frequency in the two successive evolution times. The later resonances, for example, form the diagonal resonances observed in homonuclear 2D spectra. Magnetization components that relax during the scheme will show zero frequency for all evolution periods that occurred before the magnetization relaxed. Such signals are called axial peaks and are usually not of interest.

The number of dimensions measured should be kept to a minimum since increasing their number reduces the sensitivity due to the additional quadrature sampling step (see below), larger signal losses due to relaxation and additional RF pulses. Theoretical considerations show that nD spectra do not offer fundamentally new information but are just the mathematical products of the corresponding basic 2D experiments [105]. More than two dimensions should mainly be used to reduce spectral overlap. Most multidimensional experiments are run with two or three dimensions. Only for a few experiments may a four-dimensional (4D) scheme be beneficial. One example of a rather frequently used 4D experiment is a homonuclear [^{1}H,^{1}H]-NOESY which is resolved into a ^{13}C and a ^{15}N dimension [106].

Based on the scheme given in Eq. (34), every evolution time is represented by a separate dimension in the spectrum. But experiments can be designed which combine the information from different evolution periods into one dimension. The basic principle of these experiments is very simple. Whenever two evolution times are incremented simultaneously, the corresponding frequencies occur in one spectral dimension, reducing the number of dimensions by one but keeping the same information [107,108]. In such experiments one frequency is encoded conventionally on the chemical shift scale. This signal is modulated by the offset frequency of the second nucleus leading to a splitting similar to a J coupling but representing the second chemical shift. Hence, the carrier frequency for the second nucleus must be set to one edge of the spectrum since positive and negative frequencies with regard to the carrier result in the same splitting. The chemical shifts of the two nuclei are obtained from the centre frequency of the two lines and from their splitting [107,108].

In multidimensional spectra, resonances should have absorptive lineshapes in all dimensions for the best spectral resolution and quality of an nD spectrum. To prevent the undesirable mixture of absorptive and dispersive signals, the two orthogonal transverse magnetization components represented by the operators I_x and I_y must be obtained separately from the final signal. In the framework of coherence pathways, both $+k$ and $-k$ coherence levels of a k quantum coherence during an evolution time must be maintained [16,40], which then allows separation of the operators I_x and I_y in the final signal. For practical applications this requires that sine and cosine components of the signal during the evolution time are not mixed when accumulating the data. In other words, these components should not be summed into one FID, otherwise only n- or p-type peaks are obtained which do not have a pure phase; p-type peaks result from a coherence pathway whose coherence levels have the same sign during the evolution and final detection period, opposite signs lead to n-type peaks [16] (Fig. 1).

In analogy to the direct acquisition of the signal, a quadrature scheme must be applied in the indirect dimension. For the indirect dimensions the sine and cosine components of the signal cannot be measured simultaneously. The two quadrature components are typically sampled consecutively, changing the phase of the 90° RF pulse at the start of the evolution time by 90° according to one of the schemes given in Table 3. This procedure reduces the sensitivity for every additional dimension by a factor $\sqrt{2}$. With respect to

Table 3
Properties of different quadrature sampling schemes

Quadrature scheme	Sampling of x and y components[a]				FT mode	Axial peaks[b]	Folded peaks[c]
	n	$n+1$	$n+2$	$n+3$			
Redfield	$x(t)$	$y(t+\Delta/2)$	$x(t+\Delta)$	$y(t+3\Delta/2)$	Real[d]	Centre	Mirrored
TPPI	$x(t)$	$y(t+\Delta/2)$	$-x(t+\Delta)$	$-y(t+3\Delta/2)$	Real	Edge	Mirrored
Complex	$x(t)$	$y(t)$	$x(t+\Delta)$	$y(t+\Delta)$	Complex	Centre	Cyclic
Complex-TPPI	$x(t)$	$y(t)$	$-x(t+\Delta)$	$-y(t+\Delta)$	Complex[d]	Edge	Cyclic

[a] The four columns indicate consecutive time points at which four magnetization components are sampled which evolve during the evolution time period; Δ stands for the dwell time which is equal to the inverse of the frequency range sampled; $x(t)$ and $y(t)$ refer to the x- and y-component at time point t, respectively; the sign indicates the use of the positive or negative component.

[b] Axial peaks appear either in the centre or at the edge of the spectral range selected.

[c] Folded peaks are either mirrored at the closer edge of the spectral range or cyclically shifted into the spectrum by subtraction of the spectral range.

[d] Every second pair of data points in the indirect dimension has to be inverted in sign before Fourier transformation (FT), the same goal can be achieved by changing the phase setting of the receiver by 180°.

sensitivity it is important to note that all noise in the spectrum originates from the measurement in the direct dimension. During the evolution periods the signal may be reduced due to relaxation but no noise is added. As there is no noise to be excluded from the bandwidth of interest, there is no need for filters in the indirect dimensions. None the less, the baseline in indirect dimensions may be distorted. This baseline distortion originates from linear phase corrections applied in the indirect dimensions. Therefore, linear phase corrections must be avoided by adjusting the initial delay of the evolution time properly. In principle, the minimal evolution time should be zero. Often this delay cannot be zero. For example, the finite duration of the RF pulses at the beginning and at the end of the evolution period results in evolution of the magnetization, and a linear phase correction is required for an absorptive spectrum. It is customary to sample the first point at half the dwell time. For data sampled as complex data points this requires a linear phase correction of 180° across the spectrum which does not introduce baseline curvature [97,99]. As an additional advantage, folded peaks have opposite sign and are easily detected if they do not overlap with an unfolded resonance line. This feature proves useful in some instances to reduce the spectral range together with the number of increments required, as for example in the indirect carbon dimension of heteronuclear multidimensional spectra [109]. Hence, folding can be used to extend the phase cycling and/or to reduce disk storage requirements.

For quadrature detection in indirect dimensions, several techniques are available [110] (Table 3). The individual schemes sample the data at different time points and with a different sign which requires suitable Fourier transform (FT) algorithms to be used. The particular method affects both the frequency position of the axial peaks and the folding behaviour for resonances outside the selected spectral range (Table 3). The best overall performance can be expected using a combination of complex sampling [111] with TPPI phase incrementation [81]. This scheme allows adjustment of the initial delay to obtain optimal baseline behaviour, and at the same time places axial peaks at the edge of the spectrum [110]. In principle, axial peaks are suppressed using a suitable phase cycling scheme, for example the phase cycle x, −x applied to the excitation pulse and the receiver. None the less, residual intensity should still be moved to the edge of the spectrum. TPPI [81] and Redfield [80] quadrature detection are nowadays only used when their specific folding properties are required.

2.6. Data processing

2.6.1. Transforming the time domain data into a spectrum

A detailed description of data processing methods used in biomolecular NMR is outside the scope of this article. There are excellent monographs dealing with all aspects of data processing in detail [112–114]. Here only a few basic aspects shall be mentioned. In

NMR, time-dependent oscillations of the magnetization are measured, which can be represented in an analytical form as a complex signal $S(t)$.

$$S(t) = \sum_k \exp(2i\pi\nu_k t) \exp(-t/T_{2k}) \quad (35)$$

where ν_k are the individual resonance frequencies and T_{2k} the corresponding transverse relaxation times. The frequency components ν_k encoded in the modulation are typically analysed by a complex Fourier transformation resulting in a spectrum with a real part containing absorptive lines $A_k(\nu_k - \nu)$ of the form

$$A_k(\nu_k - \nu) = T_{2k}/(1 + 4\pi^2 T_{2k}^2(\nu_k - \nu)^2) \quad (36)$$

and an imaginary part containing dispersive lines $D_k(\nu_k - \nu)$

$$D_k(\nu_k - \nu) = 2\pi T_{2k}^2(\nu_k - \nu)/(1 + 4\pi^2 T_{2k}^2(\nu_k - \nu)^2) \quad (37)$$

In practice, the signals in the real part of the spectrum may not be completely absorptive due to a phase factor in the modulation of the signal. By a suitable mixing of the real and imaginary parts using a phase correction routine, absorptive lines can be obtained in the real part, and dispersive lines in the imaginary part of the spectrum. Absorptive lineshapes are preferred since they have narrower lineshapes (Eqs. (36) and (37)) and hence offer a better resolved spectrum. In multidimensional NMR experiments, proper acquisition schemes have to be used to avoid summation of absorptive and dispersive lines in the real part of the spectrum (Table 3). A sum of absorptive and dispersive resonances cannot be corrected by a mathematical procedure and severely degrades the spectral quality. Alternative analysis methods to Fourier transformation are available but are not frequently used because they often require extensive calculation times, consist of non-linear algorithms which may distort the signal intensities, and the quality of the results is sensitive to parameter settings [113,114].

Because the causality principle requires the measured FID to be zero for times smaller than zero, Fourier transformation of the FID leads to a relation (Kramers–Kronig relation) between the real and imaginary part of the spectrum [16]. The two parts can be calculated from each other by a Hilbert transformation. Since Fourier transformation results in a real and an imaginary part with identical information content, the number of data points N in the FID must be doubled by adding N zeroes at the end of the FID (zero filling). In this way N independent data points in the FID are represented by N independent data points in the spectrum. More zero filling smooths the representation of the data by interpolation, but no additional information can be obtained [7,115]. To avoid truncation artefacts, which result in oscillations around individual signals, zero-filled FIDs must be brought smoothly to zero by multiplication with a weighting function which becomes zero at the end of the FID.

The first data point in the FID is often measured as close as possible to the time point zero in order to avoid a first-order phase correction in the spectrum. With this procedure the intensity of the first time domain data point should be averaged with the last data point in the FID to result in a properly periodic signal [116]; in practice this is often equivalent to a division of the first point by two. The first data point represents the integral of the spectrum and overemphasizing its intensity adds a constant offset to the spectrum which can be very disturbing in multidimensional spectra since the offset usually varies from trace to trace. NMR software provides the possibility to scale the first point to remove the baseline offset. In indirect dimensions, where the measurement starts after half a dwell time, the situation is different. In this case the first data point represents the correct integral and no additional scaling is necessary, but a linear phase correction of 180° has to be applied across the spectrum.

In multidimensional experiments the maximal evolution time in indirect dimensions must often be chosen to be rather short to achieve the best sensitivity and therefore truncated FIDs are often obtained for indirect dimensions. Applying weighting functions directly to truncated FIDs discards some of the measured signal. In this situation linear prediction provides a possibility to extend the experimental data in the time domain before applying weighting functions [113]. However, typically used algorithms determine four parameters for every signal: frequency, intensity, linewidth and phase. Enough data points must be available to prevent overfitting the data and the number of predicted points should as a rule of thumb not exceed the number of measured points. Linear prediction works best when the time-domain

data to be extended contains a small number of signals. In order to achieve this, all of the other dimensions of the spectrum should be Fourier transformed before linear prediction in a given dimension. If more than one dimension is to be linearly predicted, then inverse Fourier transformations will be necessary. It should be noted that in the first round of Fourier transformations, window functions are not applied because this would throw away information present in the FID. Even with linear prediction the resulting spectrum in an indirect dimension of a 3D, and especially a 4D, experiment may still have a resolution of only 40 Hz per point or even less. Applying resolution enhancement filters to FIDs with such a low resolution is of little use and often simple cosine functions are applied. There are a variety of commercial and non-commercial programs which allow interactive evaluation of NMR data using a graphics interface. However, for time-consuming calculations, such as linear prediction or sophisticated baseline correction algorithms, it may be advantageous to use a program with no graphic interface to enable processing in batch mode on high performance computers [117,118].

2.6.2. Referencing the chemical shift

The nuclear shielding constant σ_i describes the shielding effect of the electrons on the nucleus which results in the local magnetic field B_i experienced by the nucleus i being different from the applied field B_0 with $B_i = (1 - \sigma_i)B_0$. This shielding influences the resonance frequency and gives rise to chemical shifts between differently shielded nuclei. The chemical shift has long been known to be extremely sensitive to a multitude of structural, electronic, magnetic and dynamical variables and in principle contains a wealth of information on the state of the system under investigation. This potential is largely offset by the difficulties of a detailed interpretation which attributes the measured chemical shift to the various contributions. However, the large amount of data represented by the ^{1}H, ^{13}C and ^{15}N shifts in known 3D NMR structures of proteins forms the basis for a multitude of empirical and semi-empirical correlations with structural parameters. These correlations can be used during the assignment process as an additional source of information [15,119–122]. It is also possible to refine protein structures based on chemical shifts, and even with insufficient information for a structure determination, chemical shifts can be used to distinguish between alpha helix and beta sheet via the chemical shift index [120,123]. This index provides a simple tool for identifying protein secondary structure through analysis of backbone ^{13}C chemical shifts. Further information on many aspects of the use of chemical shifts in studies of proteins can be found in a recent review article [124].

The evaluation of chemical shift data requires an accurate referencing of NMR spectra both for reproducibility and for the correlation of the chemical shift with structural properties. A wide variety of reference compounds exist for various solvents and many nuclei. Referencing each nuclear species individually is cumbersome and prone to errors. Reference substances may interact with the protein or not be soluble in water. In addition, the reference chemical shift may depend on parameters like temperature, pH or ionic strength. External referencing circumvents most of these problems. However, separating the solution and the standard into two compartments introduces susceptibility effects which depend on the sample geometry and disappear only for spherical inserts. With the proton omnipresent in biological samples, indirect referencing of the heteronuclei to a proton standard becomes attractive. Recently, it was proposed to exclusively use dimethylsilapentane sulfonic acid (DSS) as standard for referencing of proton chemical shifts, due to its favourable properties as a reference compound, and to relate standards for heteronuclei to DSS by a scaling factor Ξ which is specific for a selected heteronuclear standard [125]. The absolute methyl proton frequency in DSS in the sample at a given field is simply multiplied by Ξ to obtain the zero frequency for the heteronuclear chemical shift scale. Values of Ξ for ^{13}C and ^{15}N [125] as well as for ^{19}F and ^{31}P [126] have been published for the standards 10 mM DSS in water (DSS), liquid NH_3 (NH_3), trifluoroacetic acid (TFA), and 85% ortho-phosphoric acid (H_3PO_4), respectively, and are reproduced in Eqs. (38)–(42):

$$\Xi(^1\mathrm{H},\ \mathrm{DSS}) = 1.000000000 \tag{38}$$

$$\Xi(^{13}\mathrm{C},\ \mathrm{DSS}) = 0.251449530 \tag{39}$$

$$\Xi(^{15}\mathrm{N},\ \mathrm{NH_3}) = 0.101329118 \tag{40}$$

$$\Xi(^{19}\mathrm{F},\ \mathrm{TFA}) = 0.940866982 \tag{41}$$

$$\Xi(^{31}P,\ H_3PO_4) = 0.404807356 \quad (42)$$

In practice, the frequency difference between the methyl proton resonance of DSS and the carrier (usually at the water resonance) must be subtracted from the absolute frequency of the carrier to obtain the zero ppm reference for protons. Chemical shifts referenced to a variety of different reference compounds can be readjusted to conform to the indirect referencing discussed above using published conversion data [125].

The low digital resolution typically obtained in 3D and 4D NMR spectra makes calibration critically dependent on the spectral data point that represents the position of the carrier frequency. In general, the number of points N contained in an NMR spectrum is a power of 2. Assuming a numbering of the points from 1 to N, the question arises if the carrier frequency is represented by point $N/2 - 0.5$ or by point $N/2 + 0.5$. Using the fact that the frequency domain spectrum is a periodic function, point 1 and point $N + 1$ have identical values and hence point $N + 0.5$ represents the position of the carrier frequency. However, the implementation in the software used may be different. When details of the transformation software are not known, a simple test allows determination of the position of the carrier frequency in the spectrum. Adding a constant to the FID before Fourier transformation will create a spike in the spectrum which appears at the carrier frequency.

3. NMR instrumentation

3.1. Layout of a high-resolution NMR spectrometer

In this section the major features of a modern NMR spectrometer are discussed. A spectrometer used for studies of biological macromolecules does not differ in its basic functionality from any other NMR instrument used for studies of compounds in solution. Fig. 8 displays a block diagram which is used in the following as a basis for a short discussion of the major components. A modern NMR spectrometer is controlled by a dedicated spectrometer computer which is instructed by the operator via a general purpose host

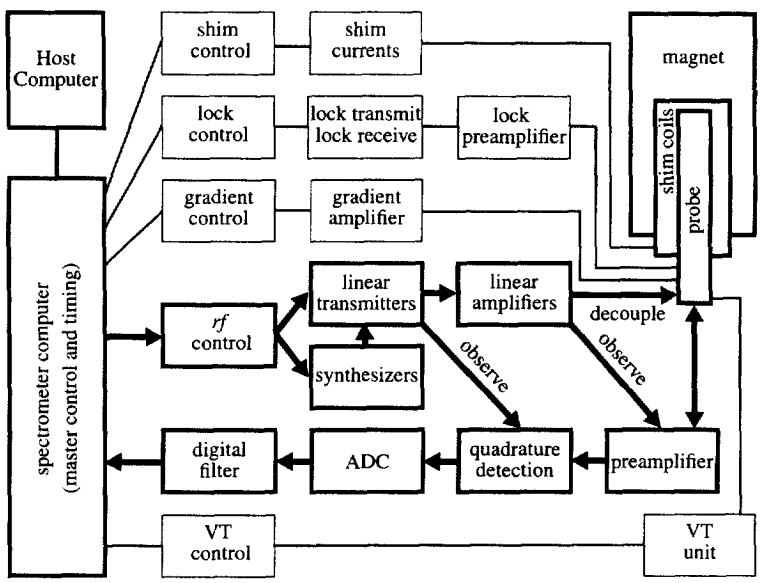

Fig. 8. Block diagram of a typical high-resolution NMR spectrometer. The main parts of the spectrometer are drawn with heavy lines; the arrows indicate the pathway from the spectrometer computer to the probe and back to the computer where the NMR signal is stored. From the preamplifier both the RF pulses on the observe channel and the detected NMR signal travel on the same cable. For the observe channel the reference frequency for detection has to be fed into the receiving pathway. The parts drawn and connected with thin lines provide auxiliary functions of the spectrometer which are essential for a spectrometer used for applications with biological macromolecules; VT stands for variable temperature and ADC for analog-to-digital converter.

computer workstation. Additional processors perform specific functions under the master timing and control of the spectrometer computer. In Fig. 8 the main parts of a spectrometer are connected by arrows drawn with heavy lines. Using this figure the essential steps in obtaining an NMR spectrum can be followed. First, the spectrometer computer instructs the RF control processor to set the necessary frequencies in the synthesizers and to send RF pulses from the transmitter to the different amplifiers according to the experimental requirements. Based on digitally stored data the transmitter prepares the pulses with the required shapes, phases, durations and power settings before sending them to the linear amplifiers. Modern NMR spectrometers are able to set all necessary parameters within a few microseconds during the execution of a pulse sequence. All stages in the transmitter and the power amplifiers have to be linear otherwise pulses with non-rectangular shapes will be distorted and cannot act in the way expected (Section 2.2.2). Via the linear amplifiers the RF pulses reach the probe which contains a coil that delivers the RF frequency to the sample located in the top of the probe. When no RF pulse is applied, the amplifiers are completely blanked, so that the spins can precess free from any RF disturbance. Because the same coil is used for the application of RF pulses at the observe frequency and for receiving the very weak response from the spins, the pulses at the observe frequency are routed through the preamplifier. A special safety circuitry protects the preamplifier from the very high voltage present during an RF pulse and directs the pulse only towards the coil. In the receive mode the NMR signal picked up by the receiving coil reaches the preamplifier stage with minimal attenuation. The signal leaves the preamplifier still at the actual NMR frequency amplified sufficiently to preserve the S/N in the subsequent amplification and mixing stages. The signal cannot be digitized at the NMR frequency and must be transformed into a frequency range of a few tens of kHz where digitizers with a high dynamic range exist. Reducing the frequency does not happen in one step. First, all NMR frequencies are transformed to the same intermediate frequency and the two quadrature channels are created (Section 3.3.1). A further mixing step reduces the signal frequencies of the quadrature channels to lower frequencies which can be digitized in the analog-to-digital converter (ADC) that samples the signal at discrete time points and converts it into a series of numbers. Modern ADCs oversample the data [101] and digitize a frequency range that is much larger than the one desired. The final spectral range is selected using digital filters which can be designed to have a much better performance than corresponding analog filters (Section 2.4.4). If digital filters are not available, the corresponding analog filters must be used before the ADC. After digitizing and filtering, the signal is sent to the computer memory where different scans are summed and the data can later be processed.

In addition to the main task of recording the NMR spectrum, a spectrometer fulfils many auxiliary functions which make modern NMR spectroscopy possible (Fig. 8). Very stable adjustable shim currents must be supplied to the shim coils which create a correcting magnetic field to obtain the required homogeneity of the main magnetic field. The homogeneity thus obtainable by far outperforms the long-term stability of the frequency sources and the magnetic field. To obtain sufficient stability the ratio of the frequencies and the magnetic field is kept constant by permanently monitoring a reference NMR signal at a specific frequency. For this locking of field and frequency the deuterium signal of some deuterated solvent added to the sample is usually observed. Any deviation of the deuterium frequency from a preset value is corrected by a very small change of the magnetic field using a special coil in the room temperature shim system. In this context, the variable temperature (VT) capabilities of a spectrometer become very important. In biological NMR measurements deuterated water often serves as lock substance. However, the deuterium resonance frequency of D_2O depends strongly on the temperature and without a very stable temperature in the sample the lock could not perform its task.

3.2. Spectrometer configuration for biomolecular NMR

The use of an NMR spectrometer for studies of biological macromolecules in solution defines the hardware configuration to a large extent. The importance of proton resonances with their limited spectral dispersion and the large number of resonances present in a protein sample demand, for the majority of

applications, a proton resonance frequency of at least 600 MHz which corresponds to a magnetic field strength of 14.1 Tesla (T). In addition to protons, the nuclei ^{2}H, ^{13}C, ^{15}N, ^{31}P and ^{19}F are most frequently measured (Table 1). In practice, up to four of these nuclei may be correlated in one experiment requiring four radiofrequency channels in addition to the lock channel. For example, larger proteins are often triple labelled with ^{13}C, ^{15}N and ^{2}H. Even though only ^{1}H, ^{13}C and ^{15}N nuclei are usually directly correlated, decoupling of deuterons is required to reduce the linewidths of carbon and/or nitrogen resonances. In some experiments it seems very convenient to use two channels for one nuclear species, as in the case of carbons where aliphatic and carbonyl carbons show a large chemical shift difference which makes these two groups of resonances behave in many aspects like heteronuclei. More and more experiments require shaped pulses and/or frequency shifted pulses for best performance. Consequently, at least three RF channels should be equipped with pulse-shaping capabilities which include the possibility to set the phase of the RF frequency in small increments.

Individual spectrometers will show most variability in their probes (Section 3.5) which depend rather strongly on the applications envisaged. For studies of proteins, a probe tunable to the frequencies of the nuclei ^{13}C, ^{15}N, and ^{1}H is necessary to carry out the standard experiments of proteins labelled with ^{13}C, ^{15}N and/or ^{2}H. For the decoupling of deuterium, the deuterium lock coil can be used. Such a triple resonance probe is designed to detect protons. With protons being the most important nucleus when working with proteins, a proton-only probe may seem necessary; however, the newest probe designs offer at best only modest sensitivity advantage for a selective probe compared to a modern probe with an additional broadband channel. Such a broadband inverse detection probe provides the advantage of making a wide range of other nuclei accessible which may be of interest in some applications. In addition, when working with proteins only labelled with ^{15}N, this probe becomes preferable due to its better performance at the nitrogen frequency compared to a triple resonance probe. This is because in a triple resonance probe the nitrogen and the carbon frequency are transmitted by the same coil which is optimized for the carbon frequency, reducing the performance for pulses on nitrogen. In addition, the broadband inverse detection probe can be used for the occasional direct detection of heteronuclei. In such applications the sensitivity is about half of that obtainable on a probe with a heteronuclear broadband detection coil. For occasional measurements of ^{3}H or ^{19}F, a coil intended for proton pulses can be tuned to excite and/or detect one of the two frequencies. However, proton decoupling with these nuclei requires a dedicated probe in combination with special filters to prevent spurious irradiation of e.g. fluorine frequency via the proton channel. A very versatile probe, a quadruple resonance probe, is simultaneously tuneable to ^{2}H, ^{13}C, ^{15}N, ^{31}P and ^{1}H and can be used to measure proteins and nucleic acids. However, such probes have reduced specifications compared to a triple resonance probe and the latter should be preferred for applications where one of the heteronuclear frequencies is not required.

Probes are built for a specific sample tube diameter. The most commonly used diameter is 5 mm. Probes for 3, 8 or even 10 mm are available but not so universally applicable. Typically large diameter probes do not yet reach the performance expected by extrapolating specifications of a 5 mm probe. In addition, these probes suffer from more severe problems with the H_2O resonance because shimming tends to be more difficult and adverse effects like radiation damping are more pronounced (Section 5.4.1). Nevertheless, in situations where a protein cannot be dissolved at the desired concentration for a 5 mm tube, a larger diameter sample tube is definitely an interesting alternative.

Precise and stable control of the sample temperature in the probe is very important for optimal performance of the spectrometer. More specifically, the variable temperature (VT) control system must fulfil the following requirements. First, it must be very stable and keep the temperature within 0.05 K of the set temperature. This is because the field–frequency lock is based on the deuterium resonance of water which is very temperature sensitive with a resonance shift of 0.01 ppm K^{-1}. Even small temperature changes will degrade the performance of the spectrometer by causing field corrections which are not based on a field–frequency drift. Since many protein resonances have a very small intrinsic temperature dependence, these field changes can severely deteriorate the

spectral quality. Second, easy and secure temperature stabilization is essential in the temperature range from 273 to 323 K where most experiments are performed. For proper operation of the regulation circuitry the input temperature of air supplied to the probe should be at least 10 K lower than the temperature desired in the probe. A cooling unit which can deliver dried air (or nitrogen) at 260 K at the probe entry facilitates the VT operation in the desired temperature range.

In recent years, pulsed magnetic field gradients (PFGs) have found widespread applications in experiments used for studies of biological macromolecules [71,72]. To allow such experiments to be carried out, a z gradient channel which can deliver gradients up to 0.3 T m^{-1} (30 G cm^{-1}) or more should be available. A gradient channel (Fig. 8) includes the gradient control hardware and the gradient amplifier as well as a special actively shielded gradient coil in each probe. A gradient shaping unit may not be absolutely necessary but is certainly a desirable feature when working with strong gradients. Presently available triple axis gradient coils seem to reduce the performance of the z gradient due to interactions of the three different gradient coils. Currently, most applications require only a z gradient and the necessity of installing triple axis gradients on a particular spectrometer must be evaluated carefully.

Modern spectrometers use a general purpose workstation as host computer which does not really need a special configuration except for a fast link with the spectrometer computer. For optimal performance, large memory and disk capacities are an advantage. When operated within a computer network, the host computer should not require any data for its operation as a spectrometer host computer from the network to prevent spectrometer downtimes during network interruptions.

3.3. Radiofrequency components

3.3.1. The transmitting path

The transmitting path starts at the synthesizer and ends at the RF coil in the probe (Fig. 8). The synthesizer delivers the basic frequency for the transmitter which sets the final offset frequency, duration and phase of the RF pulse. The frequency can be set in steps of at least 0.1 Hz, the phase in steps of 1° or smaller and the pulse duration in steps of 50 ns or smaller. For shaped pulses the time-dependent amplitude of the pulse is formed according to a shape stored in a waveform memory. Before entering the final linear power amplifier, the pulse passes through an attenuation stage which sets the preset power level. The RF power can be attenuated from the maximum power over a very large range, typically over 80 dB (Eq. (44)) or more, in steps of 0.1 dB or smaller. From the power amplifier the pulse travels to the coil and a linearly polarized, oscillating magnetic field $2B_1$ is established across the sample during the pulse. When different RF frequencies are applied during an experiment, each channel has to be optimized by inserting a proper bandpass filter between the power amplifier and the probe. This prevents RF frequencies widely different from the one assigned to the channel from reaching the sample where the additional frequencies could severely affect the measurement if they happen to match another resonance frequency. As discussed in Section 2.1.1 only one of the two circularly polarized waves into which B_1 can be decomposed interacts with the spins depending on the sign of the gyromagnetic ratio γ:

$$2B_1\cos(2\pi\nu_0 t) = B_1\exp(i2\pi\nu_0 t) + B_1\exp(-i2\pi\nu_0 t) \tag{43}$$

Therefore, half of the transmitter power cannot be used to excite the spins. Typical transmitter powers for protons are 50 to 100 W. Reference to Eq. (18) makes it clear that for small values of γ, higher power amplifiers are required to prevent exceedingly long RF pulses with their unsatisfactory excitation profile (Section 2.2.1). Consequently, so-called X frequency amplifiers deliver 300 to 400 W. All elements in the transmitter path must be linear, including the final power amplifiers, otherwise the performance of shaped pulses is compromised and tedious phase adjustments may be necessary when using pulses with different power. Some shaped pulses require rather high peak powers, demanding the transmitter path to be linear to high power levels. The linearity has the advantage that power levels of all the pulses can be calculated from one rectangular pulse irrespective of shape, length, power and phase. This avoids the experimental determination of these parameters which may be a rather cumbersome procedure.

In the following a few technical definitions and relations are presented which are important in the

context of the transmitter path. The transmitter power P is often expressed as a ratio to a reference power P_{ref} on a logarithmic scale (in dB units):

$$P[\mathrm{dB}] = 10 \log(P_{ref}/P) = 20 \log(V_{ref}/V) \quad (44)$$

where V stands for the applied voltage. The B_1 field is proportional to the voltage across the coil. Suppose, for example, that the user wishes to double the 90° pulse length, then the voltage at the coil must be halved and the power must be cut by a factor of four. Changing the pulse length for a 90° pulse by a factor of two requires a change in power by 6 dB. Another scale, the dBm scale, indicates the power P based on the logarithm of its magnitude in milliwatts (mW)

$$P[\mathrm{dBm}] = 10 \log(P[\mathrm{mW}]) \quad (45)$$

On this scale 100 W correspond to 50 dBm or 1 mW to 0 dBm. The power P of an amplifier can be calculated from the peak-to-peak voltage V_{pp} measured across a 50 Ohm load resistance using the equation

$$P = V_{pp}^2/400 \quad (46)$$

Using Eqs. (3) and (18) B_1 can be expressed in units of Gauss (G) and in units of kHz establishing a useful relationship between the two units

$$B_1[\mathrm{G}] = 0.2334 B_1[\mathrm{kHz}] \quad (47)$$

The strength of B_1 is often specified in units of Gauss instead of the SI unit Tesla (T) which contains 10^4 G. For example a B_1 field of 5 G corresponds to 21.42 kHz or a 90° pulse length of 11.7 μs.

Modern pulse sequences depend on phase and amplitude stability of the RF pulses which are under normal operating conditions set and maintained to high accuracy by the spectrometer hardware. If it is suspected that the performance may have been degraded, test procedures are available to check for the pulse reproducibility on the spectrometer [129].

3.3.2. The receiving path

The receiving path starts in the RF coil in the probe and ends with the digitized signal in the computer memory (Fig. 8). After being picked up by the receiver coil (Section 3.5.1) as an oscillating voltage, the signal is routed to the preamplifier. The typical voltage induced in the coil by the nuclear magnetization of interest is in the range of μV or smaller and transmission losses have to be minimized by placing the preamplifier as close as possible to the detection coil. Together with the receiving coil in the probe, the quality of the preamplifier determines the maximal S/N ratio that can be obtained with a particular spectrometer. From the preamplifier the signal is sent to the main electronic console where its frequency is converted to an intermediate frequency range which is the same for all nuclei.

The use of an intermediate frequency allows a further treatment of the signal that does not depend on the nucleus measured. At the intermediate frequency the signal is split into two channels. This is accomplished by mixing the signal with a reference frequency which has a phase difference of 90° for the two channels. Thus the two channels correspond to a sine and a cosine modulation of the signal, respectively, which determine the sign of the resonance frequency with respect to the carrier frequency. This quadrature detection scheme allows reduction of the bandwidth to be measured by a factor of two and concomitantly reducing the noise by $\sqrt{2}$. A further mixing step reduces the signal frequency to a few tens of kHz while maintaining a frequency range of at least 100 to 200 kHz. The signal is digitized and submitted to a digital filter which rejects all noise and possible signals outside the selected spectral range of typically a few kHz. The resulting digitized signal is passed to the computer memory. If digital filtering is not available, narrow-band analog filters have to be used before digitizing the signal. The benefits of digital filtering are discussed in Section 2.4.4. The digitizer must have at least 16 bit resolution so that the dynamic range is high enough to digitize signals from macromolecules dissolved in H_2O and the strong residual solvent signal simultaneously.

Some elements of the signal path discussed above need to be optimized by the operator of the NMR instrument. Following the signal path and starting at the sample, the receiving coil circuitry first needs optimization and has to be tuned to the proper frequency and matched to an impedance of 50 Ω (Section 3.5.1). When heteronuclear decoupling is applied during acquisition, a bandpass filter for the observe frequency must be inserted between the probe and the preamplifier to prevent noise created in the decoupling channel from entering into the detection path. Finally, the voltage of the detected analog signal must not exceed the dynamic range of the ADC or of earlier

amplification or mixing stages. A more detailed description of the receiving pathway lies outside the scope of this article. More details can be found in excellent reviews on this topic [127,128].

3.3.3. The lock system

With modern NMR spectrometers a full width of a proton signal at half height of 0.3 Hz at 800 MHz can be obtained which requires a stability of better than 10^{-9}. The stabilization of both the magnetic field and the RF frequency to at least the same order of magnitude is not possible. Fortunately, only the ratio of these two factors must be stable to 10^{-9}. The desired experimental conditions can thus be achieved by permanently measuring the NMR signal of a specific nucleus and compensating the field for any deviation of this signal from its resonance position. This coupling of the magnetic field to a resonance frequency, referred to as a field–frequency lock, typically uses a deuterium resonance. Deuterium can be incorporated in many solvents replacing protons. The lock circuitry detects the dispersion mode signal of deuterium (Fig. 9). This signal has zero voltage precisely at the resonance of the reference compound at $\Delta B = 0$. The lock circuitry detects any departure from the resonance position and converts it into a correcting current which is fed into a z_0 coil in the room temperature shim system. The z_0 coil adds a small homogeneous magnetic field to the main magnet field to re-establish the original field–frequency lock condition. The lock system requires the exact dispersion line which can be obtained by proper adjustment of the phase of the detected signal. A wrongly adjusted phase makes the lock response non-linear and generates a correction that deviates from the actually required field setting, a situation that is indicated in Fig. 9 by a resonance that deviates from a dispersion line.

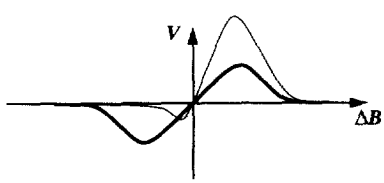

Fig. 9. Plot of the dispersion signal (voltage V) versus the deviation of the main magnetic field ΔB for the deuterium signal which is continuously recorded with the field–frequency lock activated (thick line). The thin line represents the lock signal with a wrongly adjusted phase setting.

The power of the lock channel is usually set to be just under saturation. Changing the power setting influences the phase of the detected lock signal and requires a readjustment of the phase. For measurements in H_2O adding 5 to 10% of D_2O to the sample suffices to establish a good field–frequency lock. In addition to the dispersion line used to maintain the field–frequency lock, the absorption line can be used by the operator to assess field homogeneity during shimming. When the system is not locked the magnetic field on the z_0 coil is swept over a small range which facilitates finding the lock frequency. This field sweep must be switched off in special applications where a spectrum without lock must be measured.

When working with large proteins uniform double labelling with ^{15}N and ^{13}C may no longer be sufficient for a complete structure determination and ^{2}H labelling may be used in addition [130]. Since the lock signal is derived from a deuterium resonance, every probe has a coil that is tuned to deuterium which can also be used to decouple deuterium [131,132] and to apply full power deuterium pulses [133]. In full analogy to the receiving channel the deuterium preamplifier has to be protected during the application of deuterium pulses and the lock regulation has to be set on hold. However, since the deuterium channel was originally not intended for these uses, the necessary protection circuitry is not present on all spectrometers.

3.4. The magnet

The magnetic field B_0 removes the degeneracy of the nuclear spin energy levels. Higher fields result in a better separation of resonance lines and in better sensitivity which depends on $B_0^{3/2}$ (Eq. (50)). After the initial installation of the magnet system, the magnet requires very little attention aside from the regular fillings of the cryostat with liquid nitrogen and liquid helium to keep the solenoid in a superconducting state. On the other hand, the magnet usually sets the most stringent boundary conditions for the selection of the installation site of an NMR spectrometer. Superconducting magnets have noticeable fringe fields which extend from the magnet by several metres

depending on the field strength. Disturbances in the fringe field interfere with the homogeneity of the field in the magnetic centre of the solenoid where the NMR experiment is performed. Control over the stray field area is therefore a prerequisite for stable long-term operation. Whereas movement of small ferrous items, such as small tools in an area where the stray field is smaller than 1 mT, do not interfere noticeably with the performance, large moving ferrous objects (cars, elevators) should circulate only in areas where the stray field is smaller than 0.1 mT. For safety reasons the 0.5 mT stray field should be contained within the NMR laboratory. Newly developed actively shielded magnet systems have led to a great reduction in the stray field and consequently its adverse effects. A 500 MHz actively shielded magnet produces a field of 0.5 mT in a maximal horizontal distance of 1.3 m which compares favourably with the 3.0 m for a conventional magnet. Actively shielded magnets promise to greatly reduced interference from the environment and will probably replace conventional magnets in the future except for the highest field magnets which are running at the technical limits. In addition to magnetic interferences, the performance of the spectrometer is very sensitive to vibrations. Vibrations are transmitted via the magnet stand or via vibrating ferromagnetic objects which result in small fluctuations of the magnetic field producing sidebands in the NMR spectrum.

Magnetic fields are measured in Tesla but in NMR the proton resonance frequency in MHz at the corresponding field is often used instead, for example 17.63 T correspond to 750 MHz. NMR systems above 100 MHz require superconducting magnets which are operated at the temperature of liquid helium, which is 4.2 K at standard pressure, and for the highest available fields even at 2 K. The magnet coils are constructed using niobium alloy wires embedded in a copper wire which allows the winding of a solenoid. The niobium alloys used become superconducting at low temperatures, unlike copper. In the case of a sudden, unintentional collapse of the superconductivity, known as a quench, much of the current may flow through the copper. In addition, copper guarantees efficient heat dissipation which helps to prevent damage to the superconducting wire. However, most of the energy is dissipated by protective resistors which are placed in parallel to the main coil. After a quench the solenoid can usually be recharged with no loss in performance. At a critical current density and magnetic field strength, superconductivity is lost, and for presently used materials these two factors are the principle limitations in the design of ever-higher field magnets. The stability needed for high-resolution NMR magnets requires operation in a persistent mode, i.e. with no connection to a power supply after the initial charging. Consequently, the joints which connect different superconducting wires must have an extremely small resistance to minimize the gradual reduction of the magnetic field. This drift of the field is very small indeed and even at 750 MHz the proton resonance frequency typically shifts only by 5 Hz in an hour. With this drift rate it would take 23 years before the field is reduced by only 1 MHz (0.024 T).

In addition to the main coil, a superconducting magnet contains additional superconducting coils, shim coils, which produce specific magnetic field gradients that can be used to improve the basic homogeneity of the main coil. However, the homogeneity required for high-resolution NMR experiments can only be reached by additional non-superconducting shim coils which are mounted in the room temperature bore of the superconducting magnet. Typically, 30 different room temperature shims are available making possible lineshapes which have a full width of 0.4 Hz at 50% of the peak maximum, 5 Hz at 0.55% and 8 Hz at 0.11% with a non-spinning sample of 1% chloroform in d_6-acetone. Spinning the sample can improve the lineshape but at the same time introduces instabilities which may compromise the performance of multidimensional NMR experiments. These are consequently run without spinning the sample (Section 3.5.1). Shimming directly on the rather broad D_2O resonance of a protein sample can be rather cumbersome because it is not so sensitive and responsive to changes as, for example, the deuterium resonance of d_6-acetone. In order to obtain optimal homogeneity it is helpful to have a range of samples for shimming which have different filling heights and a susceptibility matched to that of water. For example, a mixture of 3% chloroform, 84% $CBrCl_3$ and 13% d_6-acetone fulfils these criteria. Modern spectrometers offer gradient shimming procedures [134] which are most effectively used for solutions in H_2O. With such gradient shimming procedures starting from some standard shim values, a good homogeneity on protein

samples can routinely be obtained in a few minutes without interaction of the operator.

3.5. The probe

3.5.1. The radiofrequency coil

The probe contains resonance circuitry with a coil that acts as an antenna which transmits the radiofrequency pulses to the sample and subsequently receives the response of the spins via the precessing magnetization which induces a voltage across the coil. The use of two different coils for transmitting and receiving would have some conceptional advantages, but designs with two coils at the same frequency suffer from interference effects between the coils and result in inferior performance. The coil produces a linearly polarized oscillating magnetic field $2B_1$ perpendicular to the main static magnetic field (Section 2.1.1). The coil is mounted in the probe with some solid material and possibly glue. Special care is taken in the choice of materials to limit the background NMR signal from such material at the detection frequency.

One coil can be tuned simultaneously to at most three different frequencies or can be designed to be tunable over a whole range of frequencies with one additional fixed frequency. Best performance can be obtained for coils which are optimized for one specific frequency only. A probe contains one or two coils with different frequency ranges. The receiving coil requires mounting as close as possible to the sample and is usually optimized for one receiving frequency and, in addition, tuned to the lock frequency. If more frequencies are needed the probe contains one additional coil outside the receiving coil. This coil finds application for decoupling or polarization transfer experiments. With current technology only one of all the possible frequencies can be made tunable over an extensive range, for example from the ^{15}N to the ^{31}P resonance frequency, the other tuning ranges must be narrow and allow only the adjustment for one nuclear species.

One of the parameters characterizing the coil is the quality factor Q which describes the damping in the coil circuitry. In general, the higher the Q the greater the sensitivity and the larger the RF field that can be obtained with a given RF power. Since Q characterizes the damping, it also describes the lag time for any changes in the RF power or phase. The lag time in nanoseconds is approximately equal to the value of Q. Typical Q values lie in the range from 300 to 400. With superconducting coils much higher Q values can be reached [135] but the low tolerance to salt and the multinuclear capabilities of superconducting probes limit their applicability for measurements with biological macromolecules. The response of the resonance circuitry of the probe depends on its electric and magnetic properties. Using sample spinning these properties can be modulated by a non-cylindrical shape of the sample tube or small imbalances in the spinning rate. Such modulation produces small, varying sidebands in the NMR spectrum which often lead to artefacts in multidimensional NMR experiments. Hence, these spectra are measured without sample spinning. A high Q is only one of many requirements for good overall performance of a probe. For sensitivity reasons the coil must be mounted close to the sample. This spatial proximity can cause problems when the coil and the surrounding medium, usually air or nitrogen used for the temperature stabilization, do not have the same magnetic susceptibility. In this situation the presence of the coil may distort the main static magnetic field in the sample which can render shimming very difficult. Coils can be produced which match the slightly different susceptibilities of nitrogen or air and should be used with the corresponding gas.

The spatial homogeneity of the radio frequency field B_1 applied during the pulses constitutes a further important property of the coil [136]. With an inhomogeneous B_1 field not all the spins in the sample experience the same nominal pulse length. Whereas for a single 90° pulse this is hardly a problem, complicated pulse sequences with numerous RF pulses may suffer from substantial signal loss and from an increased number of artefacts. A common measure of the RF homogeneity uses the ratio of the signals obtained after a 810° pulse and after a 90° pulse. Theoretically, this should result in the same signal amplitude; in practice, signal loss occurs due to RF inhomogeneity. A good probe produces a ratio larger than 75%. A further problem which is partly related to the B_1 inhomogeneity comes from the electric field caused by the RF pulse. In aqueous protein solutions the electric field leads to substantial sample heating during the application of long pulse trains, for example during

decoupling or TOCSY sequences. Due to the inhomogeneity of the electric field the heating is not uniform and the temperature increase in some parts of the sample may be significantly higher than the average temperature rise observed. Generally, the average temperature in the sample depends on the experiment performed and can be different for the same settings of the variable temperature control system. When the sample volume is limited to the coil size or slightly smaller, the B_1 homogeneity can be improved and the heating reduced [127,137]. This can be accomplished by limiting the sample volume to the appropriate region using a sample plug inserted into special NMR tubes. The plugs have a magnetic susceptibility that is matched to the solution. None the less, some more tedious shimming may be required.

A probe must fulfil very stringent requirements. The optimal performance of a coil can easily be compromised by choosing the wrong operating conditions. The best sensitivity is obtained when the coil is tuned exactly to the resonance frequency of the individual nuclear species for every sample. In addition, the coil has to be matched to the impedance of the transmitter and receiver path, usually 50 Ω, which is required for optimum transmission of the RF pulses and the induced NMR signal via the coaxial cables. A filter inserted in the transmission path directly before the probe forms part of the circuitry and should not be removed for tuning and matching. The insertion or removal of a filter should not lengthen the duration of a 90° pulse by more than 5% under optimized conditions.

3.5.2. The magnetic field gradient coil

Modern probes not only contain RF coils but in addition actively shielded coils for the application of magnetic field gradients in one or three dimensions. To obtain a gradient strength of 0.5 T m^{-1} (50 G cm^{-1}) these coils are driven with currents in the range of 10 A. When switching such large currents on and off, for example at the start and end of a rectangular pulse, the gradient coil tends to vibrate and in addition eddy currents are induced in the surrounding metals used to build the probe. These effects interfere with the requirement of a very fast recovery of the basic, very homogeneous magnetic field after the application of a gradient pulse. Modern probes equipped with a z gradient reach full recovery of the homogeneity within 100 μs after a 2 ms rectangular gradient pulse with a strength of 0.5 T m^{-1}. Even shorter recovery times are obtained for smoothly changing pulse amplitudes such as sine or elongated sine square shapes [68]. For triple axis magnetic field gradient coils the interference between the different gradient coils in general increases the individual recovery times. On the other hand, triple axis gradients offer much more flexibility and less hassle in preventing the accidental refocusing of undesired magnetization during a pulse sequence. Furthermore, efficient automatic gradient shimming can be used for all shims. With only a z gradient the room temperature shim coils may be used for gradient shimming of non-axial shims, but this procedure is less efficient and tends to be less reliable.

For many applications the absolute gradient strength does not need to be known very precisely and a simple calibration procedure can be used to obtain the approximate gradient strength. If the gradient is applied during the acquisition of the water signal in an H_2O sample the width of the resonance line $\Delta\nu$ in the absolute value spectrum is related to the approximate gradient strength G_i, with i representing the x, y or z axis, by

$$G_i = 2\pi\Delta\nu/(\gamma d) \tag{48}$$

where d stands for the dimension of the sample in the direction of the applied gradient. Along the z axis the sample is generally longer than the RF coil and d is set to the length of the RF coil. A more precise calibration can be obtained by measuring the diffusion of a compound with known diffusion constant [68]. Although the absolute strength of the gradient rarely needs to be known very accurately, the relative strength must be set very precisely in experiments using gradients for the selection of coherence pathways (Section 4.4) otherwise severe signal loss will occur. For example, a gradient with strength 0.3 T m^{-1} and a duration of 2 ms is applied to proton magnetization which should be refocused after a 180° pulse by an identical gradient. To refocus 95% of the original signal the strength 0.3 T m^{-1} of the refocusing gradient must be set to a precision better than $\pm\ 4{\cdot}10^{-4}$ T m^{-1} (Eq. (31)).

3.5.3. The variable temperature operation

The sample temperature must be controlled very precisely to prevent temperature drift. This is of

particular relevance to studies in aqueous solution with D_2O as the lock substance. Water exhibits a large temperature-dependent resonance shift of 0.01 ppm K^{-1}. With an unstable temperature the lock system will try to compensate the shift of the water resonance which results in a shift for all other resonances with a different temperature dependence. In multidimensional NMR experiments individual resonances will no longer be completely aligned when evolution times are incremented leading to noise bands in the spectrum (t_1 noise) which run perpendicular to the axis of the direct dimension. In addition, temperature instability contributes to increased subtraction artefacts for phase cycles and in difference spectroscopy.

For temperature regulation, air flows around the sample tube after passing an electrical heating element, and a feedback system regulates the temperature of the air by controlling the power fed to the heater. For good performance of the temperature control, the input temperature of the gas flow when entering the probe should be at least 10 K lower than the temperature required at the sample position. In addition, the flow rate must be high enough to cool the coil and sample efficiently during periods of extensive RF irradiation, for example during decoupling or TOCSY mixing periods. In experiments containing such sequences the probe temperature is usually set lower than the actual sample temperature required, in this way compensation can be obtained for the average heating effect in the sample. This lower temperature can be determined experimentally by comparing the shift of an isolated resonance in a 1D spectrum, for example a methyl resonance, using only one excitation pulse eliminating the specific heating and in a spectrum with the actual sequence. Good cooling capacity requires high flow rates which may interfere with the probe performance if the flow induces vibrations of the coil or even movements of the sample. Vibration sidebands of the coil typically occur at frequencies of several thousand Hertz, are rather broad and can severely deteriorate the spectral quality. These sidebands are most easily detected around a strong solvent line and can be identified by their sensitivity to the air flow rate.

When the temperature regulation fails, built-in security circuits and properly chosen regulation parameters should prevent any damage to the sample in the probe. For example, a heater failure may freeze or overheat the sample depending on the false heater current set by the system and depending on the temperature of the gas used for regulation. On the other hand, when the gas flow stops, the regulation may set the heater current to high values in a attempt to stabilize the temperature. With the normal gas flow re-established, a heat wave will reach the sample which may denature the protein. These scenarios should be kept in mind when choosing the parameters for the regulation system.

3.6. Stability of the system

Instabilities during the measurement of a multidimensional NMR experiment introduce noise bands in the spectrum which run perpendicular to the frequency axis of the direct dimension and may severely distort the spectral quality. Such noise bands are generally referred to as t_1 noise since they were first observed in 2D spectra running parallel to the axis of the indirect dimension [16]. Any incoherent changes of the signals forming the FID in the indirect dimension may cause t_1 noise. Modern NMR spectrometers possess a remarkable internal stability and reproducibility. In many cases it is not an inherent instability of the NMR spectrometer which limits the performance, but the interaction with an unstable environment. For optimal performance of a high-field NMR spectrometer, the NMR room should be far enough from any outside electromagnetic and mechanical source of interference and the temperature of the room should be regulated to within one degree. Mechanical vibrations of the magnet system in the range of a few Hertz are difficult to compensate for, but may severely interfere with NMR difference techniques, as for example used in some hydration measurements (Section 5.3). Special care has to be taken to prevent oscillating disturbances which potentially have more influence on the performance than a corresponding random fluctuation [138]. Even in a very stable environment exceptional circumstances may still affect the measurement. In multidimensional NMR experiments with biological macromolecules, data sets are typically acquired over a period of several hours to several days and the results obtained depend critically on a high stability of the system during the entire recording time. Even a short,

transient instability in the magnetic field homogeneity or a transient temperature variation can severely distort a data set. For this reason some key experimental parameters of the overall performance of the spectrometer should continuously be monitored and stored in a file [138].

The lock level, sample temperature and room temperature are particularly sensitive parameters for the detection of any malfunctioning or external disturbance. If the user detects any disturbance when inspecting the recording file, they can restart the experiment at the point of interference or repeat the measurement of the corrupted FIDs before removing the sample from the magnet or changing any measurement parameter. These FIDs can be introduced into the multidimensional data set and a complete repetition of the measurement becomes unnecessary. The recordings are not only useful for the evaluation of individual experiments, but they also serve as a database for the design of improved laboratory facilities. The permanently stored recordings enable the instrument supervisor to inspect the instrument performance for repeated interferences, which can provide a lead to the cause of the malfunctioning. If the recordings are stored digitally on a computer, remote control of long-term measurements becomes possible from any computer inside or outside the laboratory. Although it appears that the recording of the lock level, the sample temperature and the room temperature monitors most disturbances that lead to spectral distortions, an even more rigorous surveillance could be envisaged, possibly including the current sent to the z_0 coil by the lock system, the pressure at the helium outlet, the air flow for the temperature regulation and an indicator for the RF power at the amplifier output.

4. Basic segments of pulse sequences

The first applications of 2D NMR for studies of proteins in aqueous solution used only a very few pulse sequences [5–7]. Today, a vast number of experimental schemes exist and new ones are continuously developed. Fortunately, a pulse sequence usually consists of a number of portions which belong to a rather small group of key segments from which most experimental schemes can be constructed. Many of the basic segments can be described in the framework of the operator formalism for spin $\frac{1}{2}$ nuclei [28]. For segments based on relaxation or strong spin–spin coupling, for example NOESY or TOCSY mixing periods, more extensive quantum mechanical treatments have to be applied. Once the key segments are characterized they can be used to sequentially analyse complex pulse sequences segment by segment.

Fig. 10 shows a pulse sequence diagram which shall serve as an example to illustrate that a pulse scheme is constructed from a limited number of basic segments. The individual basic segments are indicated above the pulse sequence with a short description and a number in brackets indicating the figure which describes the corresponding segment in more detail. For example, the transfer of magnetization from one nuclear species to another is used six times in this sequence. In the pulse scheme, narrow and wide black vertical bars represent 90° and 180° RF pulses which are drawn on different horizontal lines for different frequencies. In this example the resonance frequencies for proton (H), nitrogen (N), carbonyl carbon (C′) and α-carbon (C) nuclei are shown. An additional horizontal line labelled G indicates where pulsed magnetic field gradients are applied. The first 90° RF pulse on H excites proton magnetization and at the very end of the sequence during the period t_3 proton magnetization is detected. The experimental scheme correlates the chemical shifts of the amide proton and nitrogen (HN) with the α-carbon chemical shift (CA) of the preceding residue in the amino acid sequence via the intervening carbonyl carbon (CO). This 3D experiment is called HN(CO)CA [139,140] which is an acronym that summarizes the magnetization transfer and the nuclei from which the chemical shift is measured. A cross-peak in the corresponding 3D spectrum indicates a connection via the peptide bond of two sequential amino acids in a fully $^{15}N/^{13}C$ enriched protein. Hence the experiment facilitates the sequential assignment of all amino acid spin systems in a protein. A detailed discussion of the HN(CO)CA experiment can be found in the original publications [69,139,140], but for the present purpose a brief summary suffices. The sequence starts with the excitation of amide proton magnetization which is subsequently transferred to the attached ^{15}N nucleus whose chemical shift is measured during t_1. Next the magnetization

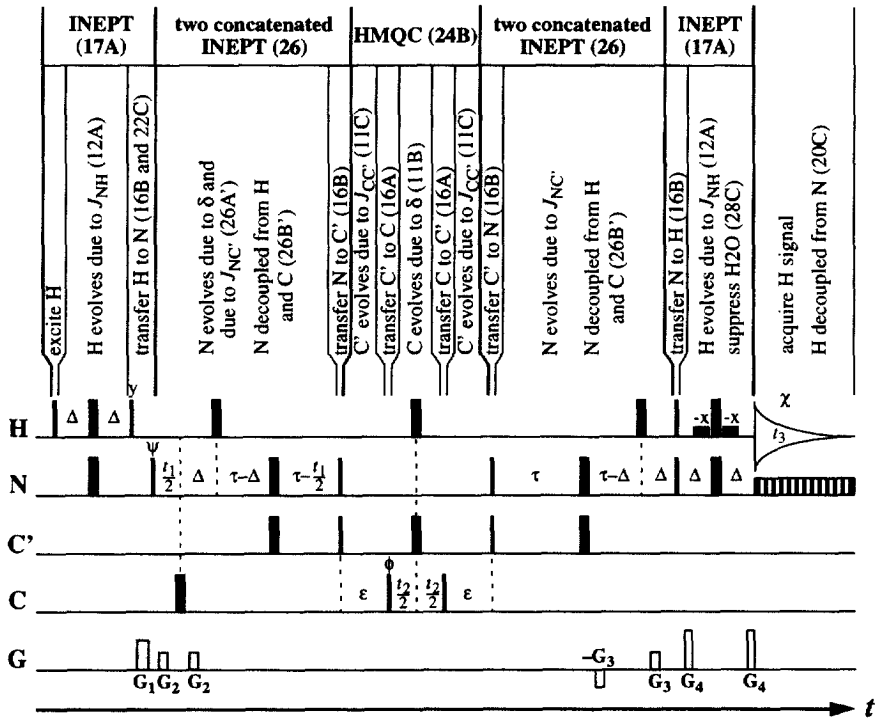

Fig. 10. Experimental scheme for the HN(CO)CA experiment [139,140] used to illustrate the segmentation of a pulse sequence into a limited number of different basic segments. The vertical lines above the pulse sequence indicate start and end of individual basic segments of the pulse scheme. The text between these lines describes the action of the particular segment and the number in brackets indicates the figure in the main text that shows the corresponding segment. At the very top common combinations of key segments (Section 4.5), for example INEPT, are indicated with the number of the figure in brackets where they are discussed. The abbreviations H, N, C′ and C stand for the amide proton, the nitrogen, the carbonyl carbon and the α-carbon nuclei, respectively. J_{NH}, $J_{NC'}$ and $J_{CC'}$ represent the scalar coupling constant between N and H, N and C′ and C and C′, respectively, δ stands for chemical shift. In the pulse scheme narrow and wide black vertical bars represent 90 and 180° RF pulses which are indicated on different horizontal lines for different frequencies: H, N, C′ and C stand for the resonance frequencies of the H, N, C′ and C nuclei, respectively. All RF pulses are applied with phase x unless indicated otherwise on top of the pulse bars where ψ stands for the phase cycle x, x, −x, −x, ϕ for x, −x and χ for the receiver cycle x, −x, −x, x. Pulsed magnetic field gradients (PFGs) are indicated on a separate horizontal line labelled G and PFGs with the same label G_i have the same strength and duration which differ from all other PFGs. The time periods t_1, t_2 and t_3 denote the three chemical shift evolution periods. The time periods labelled Δ, τ and ε are necessary to prepare the correlation between different nuclei and have the values $\Delta = (4J_{NH})^{-1}$, $\tau = (4J_{NC'})^{-1}$ and $\varepsilon = (2J_{CC'})^{-1}$.

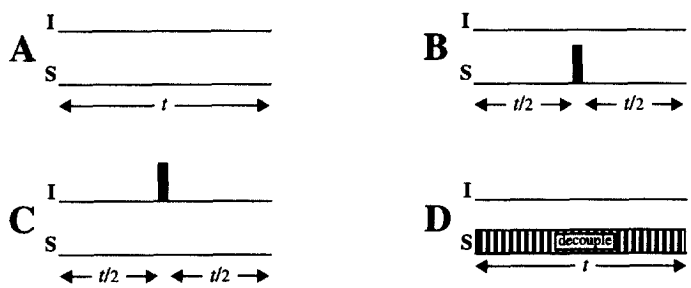

Fig. 11. Schemes for typical segments used to allow spins I to evolve due to chemical shift and/or J coupling, for example, in multidimensional NMR pulse sequences. The spins I evolve due to chemical shift in sequences A, B and D, and in sequence A in addition due to scalar coupling to the S spins. Table 4 presents the transformation properties of these sequences.

Table 4
Evolution due to chemical shift and/or J coupling for the pulse sequences in Fig. 11

Fig. 11	Initial state	Resulting product operators describing the transformation properties of the sequence
A	I^+	$I^+\cos(\pi Jt)\,e^{-i\omega t} - 2I^-S_z\sin(\pi Jt)\,e^{-i\omega t}$
	$2I^+S_z$	$2I^+S_z\cos(\pi Jt)\,e^{-i\omega t} - iI^+\sin(\pi Jt)\,e^{-i\omega t}$
	$2I^+S^+$	$2I^+S^+\,e^{-i(\omega+\Omega)t}$
B	I^+	$I^+\,e^{-i\omega t}$
	$2I^-S_z$	$-2I^+S_z\,e^{-i\omega t}$
	$2I^+S^+$	$2I^-S^-\,e^{-i\omega t}$
C	I^+	I^-
	$2I^+S_z$	$2I^-S_z$
	$2I^+S^-$	$2I^-S^-\,e^{-i\Omega t}$
D	I^+	$I^-\,e^{-i\omega t}$
	$2I^+S_z$	0
	$2I^+S^+$	0

is transferred via the C′-carbon of the preceding residue to that residue's α-carbon whose chemical shift is measured during t_2. Subsequently, the magnetization is transferred back to the ^{15}N nucleus of the original residue via the C′-carbon and finally to the amide proton where it originated. During the period t_3 the amide proton signal is measured.

In the following, commonly used key segments are analysed on the basis of a two-spin system with the scalar coupled spins I and S. Strong spin–spin coupling is not considered unless absolutely necessary, for example in TOCSY sequences. The key segments which are discussed in this section are visually represented by pulse sequence diagrams which all use the same conventions (e.g. Figs. 11 and 12). Thin and wide black vertical bars on the horizontal lines labelled I and S stand for 90° and 180° RF pulses applied to the I or S spin, respectively. All RF pulse have phase x unless indicated otherwise at the top of the pulse bars. The excitation pulse in the sequences is omitted and must be added when applying the segment to z states of the spin system. The resonance frequencies of I and S are denoted ω and Ω, respectively. For strictly homonuclear segments I and S are assigned to only one line labelled I/S (e.g. Fig. 13). Decoupling and RF mixing sequences are indicated by striped rectangles (e.g. Figs. 11 and 14). To indicate pulsed field gradients an additional horizontal line G is added to the sketches (e.g. Fig. 22) and PFGs are indicated by grey rectangles. Rarely used graphical objects are explained in the figure legends. Together with the figures there are tables provided which summarize the transformation properties of the key segments using the product operator formalism. Preference is given to a description using the shift operator basis which allows a more compact formulation of evolution due to chemical shift and magnetic field gradients. In some instances, operators in both basis systems are indicated, facilitating the link between the currently more commonly used cartesian basis and the shift operator basis. Cartesian operators are used only in cases when they allow a much more compact description.

4.1. Evolution segments

Evolution segments consist of a time period t during which the spin system evolves essentially free from external RF disturbances except possibly one or two 180° pulses (Fig. 11). During t, transverse magnetization components evolve due to their chemical shift and J coupling. Typical examples which use evolution segments are the incremented time periods introduced in pulse sequences to obtain multidimensional NMR experiments or the fixed time periods used for the preparation of in-phase and anti-phase spin states in heteronuclear experiments. Evolution segments can easily be analysed using the product operator formalism. Fig. 11 shows different chemical shift evolution segments and Table 4 presents the transformation properties of typical two-spin states when submitted to these sequences. In multidimensional experiments the time period t in these sequences may be incremented during an experiment to sample frequencies in indirect dimensions. When a 90° pulse at the start of the evolution segment brings z magnetization into the transverse plane the effective evolution of these magnetization components due to the chemical shift has a longer duration than indicated by t. This is a consequence of the non-ideal behaviour of RF pulses (see Appendix A). Resonance lines with an offset ν_k from the carrier frequency acquire a phase error in units of radians of $4\tau_{90}\nu_k$ during a 90° pulse with duration τ_{90} and strength γB_1 [16,24,26]. The

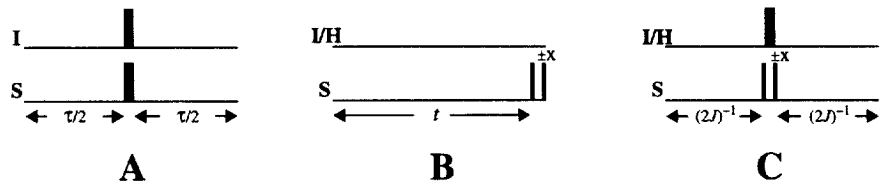

Fig. 12. Typical schemes for the preparation of spin states based on their evolution due to scalar coupling. Sequence A transforms in-phase I magnetization into I magnetization in anti-phase to spin S and vice versa. B and C allow the separation of spins I which are bound to spin S from those I spins (H) which are not bound to S. This is achieved by properly adding or subtracting two scans, I and II (Table 5), with phase x and − x for the second 90° pulse applied to the S spins. Table 5 presents the transformation properties of these sequences.

linear offset dependence of the phase error holds as long as ν_k is less than γB_1 [16]. Hence, an off-resonance 90° pulse can be treated as an ideal pulse followed by an evolution period given by $t_0 = 2\tau_{90}/\pi$. Similarly, rotating transverse magnetization to the z axis can be treated as an ideal pulse preceded by a delay $t_0 = 2\tau_{90}/\pi$ [141]. Thus there is an effective increase of t by t_0 or $2t_0$ depending on whether the evolution segment is bound by one or two 90° pulses, respectively. When evolution segments are used in multidimensional experiments to sample the resonance frequencies in indirect dimensions, this inherent evolution time leads to a linear phase gradient of the signals which can be corrected by a first-order phase correction. However, a linear phase correction may introduce baseline curvature [97,99] and should be avoided unless the correction is an exact multiple of 180° which leaves the baseline unaffected. Consequently, the initial evolution time t_{ini} in the indirect dimension is often set to half a dwell time which results in a linear phase dependence of 180° across the spectrum. The inherent evolution time can then be compensated by a subtraction from t_{ini}. An additional benefit is that folded peaks in such a spectrum have opposite sign, simplifying their identification.

Fig. 11(B) presents a segment where the net evolution of the I spin at the end of the period t does not depend on the scalar coupling J. The state of spin I at the end of t is unaffected by the coupling with S spins. Fig. 11(C) depicts a segment where the state of I at the end of t is unaffected by chemical shift and J coupling and has effectively only been inverted by the 180° pulse. In practical implementations the performance of the sequences in Fig. 11(B) and 11(C) may suffer due to the limited inversion and refocusing profiles obtained for real 180° pulses which may introduce artefacts in the final spectrum. A 180° pulse with strength γB_1 inverts, for example, only 80% of the z magnetization at an offset as small as $0.3\gamma B_1$ and at the same offset it refocuses less than 85% of x magnetization when applied along the x axis (Fig. 7). The inversion profile can be substantially improved using simple composite pulses, a solution which is not available for refocusing pulses (Section 2.2.1). Imperfect pulses result not only in a loss of sensitivity but in addition unwanted peaks may appear in the final spectrum. In evolution periods of multidimensional NMR experiments the EXORCYCLE (Section 2.2.1) should be used to prevent the appearance of artefact peaks in the final spectrum, alternatively pulsed field gradients fulfil the same purpose (Section 4.4). For the segment in Fig. 11(B) the alternative sequence in Fig. 11(D) can be used which maintains the decoupled state of I throughout the period t by the application of a decoupling sequence (Section 4.3).

Fig. 12 presents typical pulse sequence segments used to prepare and/or select special spin states obtained from evolution due to scalar couplings. The segment in Fig. 12(A) transforms in-phase into anti-phase magnetization or vice versa depending on the initial state (Table 5). The total evolution time period τ is kept fixed and the application of a 180° to both spins refocuses the chemical shift of the I spins but maintains the evolution due to scalar coupling. This sequence finds its application typically in heteronuclear experiments where nuclei of different species are brought into an anti-phase state to prepare a coherence transfer or where magnetization is refocused from an anti-phase state after a coherence transfer step to obtain observable magnetization. To counteract relaxation the delay τ is usually set to values shorter than the optimum of $(2J)^{-1}$ needed for complete evolution into anti-phase magnetization. In

Table 5
Preparation/selection of states based on their evolution due to J coupling for the pulse sequence in Fig. 12

Fig. 12	Initial state[a]	Resulting product operators describing the transformation properties of the sequence[b]
A	I^+	$2iI^-S_z \sin(\pi J\tau) + I^- \cos(\pi J\tau)$
	$2I^+S_z$	$-iI^- \sin(\pi J\tau) - 2I^-S_z \cos(\pi J\tau)$
	$2I^-S^+$	$2I^-S^-$
B	$I^+ + H^+$	(I) + (II) $= 2I^+ \cos(\pi Jt)\, e^{-i\omega(I)t} + 2H^+ e^{-i\omega(H)t}$
	$I^+ + H^-$	(I) − (II) $= 4iI^+S_z \sin(\pi Jt)\, e^{-i\omega(I)}$
	$H^+ + 2I^+S_z$	(I) + (II) $= -2iI^+ \sin(\pi Jt)\, e^{-i\omega(I)t} + 2H^+ e^{-i\omega(H)t}$
	$H^+ + 2I^+S_z$	(I) − (II) $= -4I^+S_z \cos(\pi Jt)\, e^{-i\omega(I)}$
C	$H^+ + I^+$	(I) + (II) $= 2H^-$
	$H^- + I^+$	(I) − (II) $= -2I^-$
	$H^- + 2I^+S_z$	(I) + (II) $= H^- + 2I^-S_z$
	$H^+ + 2I^+S_z$	(I) − (II) $= 0$

[a] I and H stand for the same type of nucleus; the spins I are coupled to the spins S and the spins H are not coupled to S spins, the spins I and H are not coupled.

[b] (I) stands for the segment where both 90° pulses on S spins are applied with phase x and (II) for the segment with phases x and − x. (I) + (II) represents the sum of the two scans, (I) − (II) the difference; the resonance frequencies of the I and the H spins are indicated by $\omega(I)$ and $\omega(H)$, respectively.

practical implementations the performance of the 180° pulses requires special attention to avoid artefacts in the spectrum and the discussion in conjunction with Fig. 11(B) and 11(C) is valid here as well.

Evolution due to J coupling is also used to prepare states which differ in sign, allowing a separation of signals from species where nuclei I are bound to a nucleus S from those where nuclei I are not bound to a nucleus S (Fig. 12(B) and 12(C)) [142,143]. Using this segment, for example, protons I bound to a ^{15}N nucleus can be separately observed from protons H not bound to ^{15}N. For the separation of the two classes of nuclei the segment is applied twice, once with a 180° pulse and once without a 180° pulse on the S spins. For both the filter element (Fig. 12(B)) and the half-filter element (Fig. 12(C)) the difference of the two signals thus obtained selects resonances of the nuclei which are bound to a heteronucleus and for the half-filter the sum selects the resonances of the nuclei not bound to a heteronucleus [143]. Half-filter experiments can, for example, be used to observe the interaction of the amide protons separately from those of the aromatic protons in a homonuclear 2D experiment of a ^{15}N labelled protein. In a further application, nuclei from two different molecules in a sample can be observed in two separate spectra when one molecule is labelled with a heteronucleus S and the other is not [144,145].

In practice, two 90° pulses are used to form the 180° pulse on the S nuclei (Fig. 12(B) and 12(C)). Two experiments are performed, one with the same RF phase for the two 90° pulses to produce a 180° pulse and one with a phase difference of 180° for the two 90° pulses producing an effective 0° pulse. The reason for this technical trick lies in the poor inversion profile of the 180° pulse. The 90_x90_{-x} pulse sandwich results only in a 0° pulse on resonance, off-resonances it shows an excitation profile that very closely matches the inversion profile of a 180° pulse in the frequency range $\pm \gamma B_1$. Hence, the 90_x90_{-x} pulses compensate the non-ideal behaviour of the 180° pulse and reduce signal contributions from the I spins when non-bonded H spins are to be selected. This technique improves the selection of H spins but spurious signals of I resonances still constitute a permanent problem [143]. Not only must the 180° pulse invert all the S spins, but the filter delay must exactly match $(2J)^{-1}$. The latter condition often cannot be fulfilled since the values of the coupling constants vary, particularly if the heteronucleus is ^{13}C. In addition, the labelling fraction of the S nuclei must be 100%, otherwise breakthrough cannot be prevented. In contrast to the

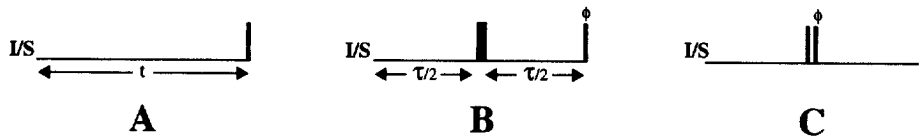

Fig. 13. Schemes of typical homonuclear through-bond transfer segments used in multidimensional NMR pulse sequences. Segment A represents a COSY-type transfer. Segment B serves for the creation of multiple quantum states; the phase ϕ allows selection of even or odd multiple quantum coherence to an order which depends on the number of coupled spins. Segment C represents a double quantum filter with ϕ = x, y, − x, − y and the receiver phase x, − y, − x, y; this element selects coherences which pass through a double quantum state between the two pulses. Table 6 presents the transformation properties of these segments.

problems with the selection of the *H* resonances, the selection of the *I* resonances usually constitutes no problem because imperfections do not introduce *H* spin resonances but merely reduce the S/N of the selected *I* resonances. This discussion of filter elements with two spins applies qualitatively to systems with more spins as long as the heteronuclear coupling constants are much larger than the homonuclear coupling constants among the *I* and *H* spins and among the *S* spins [143].

4.2. Transfer segments

4.2.1. Homonuclear through-bond transfer

Magnetization transfer between spins is based on through-bond connectivities via *J* couplings, on through-space interactions via NOEs and ROEs or on chemical exchange. Transfer segments accomplish magnetization or coherence transfer and establish a correlation between the spins. The simplest transfer segment consists just of a 90° pulse that acts on homonuclear anti-phase magnetization developed during an evolution time period *t* due to scalar coupling (Fig. 13(A)). The 90° pulse acting on anti-phase coherence causes a coherence transfer. This segment was embedded in the first 2D experiment proposed [3,4] which was later named COSY, which stands for 2D correlation spectroscopy [7,146,147]. In proteins, only couplings over a maximum of three chemical bonds are usually large enough to manifest themselves in a COSY step. In [^{1}H, ^{1}H]-COSY experiments, the anti-phase magnetization cannot be refocused due to the widely different coupling constants. In multidimensional spectra, anti-phase multiplet signals are thus obtained which contain positive and negative contributions that tend to cancel each other for broad resonance lines. When the coupling constants vary only in a narrow range, as for aliphatic carbon coupling constants in ^{13}C-labelled proteins, refocusing of the anti-phase magnetization obtained after the transfer step becomes possible and in-phase peaks can be obtained in the spectrum.

The sequence in Fig. 13(B) is closely related to the COSY sequence and excites multiple quantum coherence [148]. In-phase magnetization evolves into anti-phase magnetization during τ due to scalar coupling. A 180° pulse refocuses the chemical shift evolution. Setting the phase ϕ of the 90° pulse at the end of the segment to x results in even-quantum coherences being detected, whereas for ϕ = y odd-quantum coherences are obtained [149]. The length of the time period τ, the number of coupled spins and their mutual coupling constants determine the exact states that can be created. Again, the product operator formalism suffices to analyse the sequence (Table 6). Multiple quantum coherences are *n* times more sensitive to magnetic field gradients and phase shifts of RF pulses than single quantum coherences and similarly have proportionally larger susceptibility to the effects of pulse imperfections, a fact that may influence the performance of the sequence in practical implementations.

The double quantum filter segment shown in Fig. 13(C) eliminates coherence pathways which do not pass coherence level $|p| = 2$ between the two 90° pulses and are not in the coherence state $p = -1$ after the second pulse. Hence, coherence order changes Δp of −3 or +1 are selected (Fig. 1). Following the system given at the end of Section 2.1.2, the appropriate phase cycling scheme can be designed [38]. With N = 4 phase steps of $\Delta\phi$ = 90°, the pulse phase cycle becomes ϕ = x, y, −x, −y and the signal must be accumulated with the receiver cycling through x, −y, −x, y (Fig. 13(C), Table 6). More generally, a multiple quantum filter consists of two 90° pulses which are separated by the time to switch the phase of a pulse,

Table 6
Homonuclear through-bond transfer segments as in Fig. 13

Fig. 13	Initial state	Resulting product operators describing the transformation properties of the sequence[a]
A	I^+	$(I^- + I^+ + 2iI_z)(i(S^- - S^+)\sin(\pi Jt) + \cos(\pi Jt))\,e^{-i\omega t}/2$
	I_y	$-I_x\cos(\pi Jt)\sin(\omega t) + I_z\cos(\pi Jt)\cos(\omega t) + 2I_xS_y\sin(\pi Jt)\cos(\omega t) + 2I_zS_y\sin(\pi Jt)\sin(\omega t)$
	I^-S_z	$-i(I^- + I^+ + 2iI_z)((S^- - S^+)\cos(\pi Jt) + \sin(\pi Jt))\,e^{-i\omega t}/2$
	$2I_yS_z$	$-I_x\cos(\omega t)\sin(\pi Jt) - I_z\sin(\omega t)\sin(\pi Jt) + 2I_xS_y\sin(\omega t)\cos(\pi Jt) - 2I_zS_y\cos(\omega t)\cos(\pi Jt)$
	$2I^-S^+$	$(I^- + I^+ + 2iI_z)(S^- + S^+ + 2iS_z)\,e^{-i(\omega+\Omega)t}$
	$2I_yS_z$	$-2I_xS_x\cos(\Omega t)\sin(\omega t) + 2I_zS_x\cos(\omega t)\cos(\Omega t) - 2I_xS_z\sin(\omega t)\sin(\Omega t) + 2I_zS_z\cos(\omega t)\sin(\Omega t)$
B	I_y	$\phi = x$: $-I_z\cos(\pi Jt) - 2I_xS_y\sin(\pi Jt)$
		$\phi = y$: $-I_y\cos(\pi Jt) - 2I_zS_x\sin(\pi Jt)$
C	I^+	0
	$2I^+S_z$	$-I_z(S^+ + S^-)/2 - (I^+ + I^-)S_z/2$
	$2I^+S^+$	$I^+(3S^+ - S^-)/4 - I^-(S^+ - 3S^-)/4 + I_zS_z$

[a] For the transformation under the sequence of Fig. 13(C) the sum of four transients is indicated, which is obtained with the phase cycle ϕ = x, y, −x, −y and the concomitant receiver cycling x, −y, −x, y.

typically 2 μs. By proper phase cycling of the phase ϕ of the second pulse, the coherence level between the pulses that contributes to the final signal can be selected.

Nuclei separated by more than three chemical bonds but belonging to the same spin system can be correlated using several COSY-steps. Depending on the size of the coupling constants involved, this approach may be limited to very few steps by transverse relaxation. Total correlation (TOCSY) mixing sequences (Fig. 14) offer a more efficient scheme where all transfers are active simultaneously and the relaxation depends on a mixture of longitudinal and transverse relaxation rates and is therefore slower than in a COSY-step. In addition, the TOCSY sequence also transfers in-phase magnetization, in contrast to COSY which transfers only anti-phase magnetization. The TOCSY transfer segment consists of a strong spin-lock mixing sequence [43,44] (Fig. 14). The different mixing sequences available have similar average power requirements. The choice of the sequence

Fig. 14. Scheme for a homonuclear TOCSY transfer segment. During τ the spins I and S are spin-locked with a strong RF field which makes magnetization transfer from the I to the S spin possible, and vice versa, according to Eq. (9).

depends on the orientation of the magnetization at the start of the sequence, whether the mixing is applied to protons or other nuclei and the required efficiency of the mixing for magnetization components in the three spatial dimensions. All mixing sequences simultaneously transfer magnetization components aligned along the mixing axis or perpendicular to it, but with different efficiency. In cases where magnetization components aligned predominantly along one axis should be transferred, spin-lock purge pulses (Section 2.3) with a duration of 1 to 2 ms are used before and after the mixing, which dephase magnetization components not aligned with the mixing axis and partially remove contributions from anti-phase components. The two trim pulses must differ in their duration to prevent refocusing of unwanted signals. Alternatively, phase cycled 90° pulses of the form $90_{\phi 1}$–mixing–$90_{\phi 2}$ can be applied before and after the mixing sequence. For example, y magnetization can be selected to be mixed along the y axis using the four-step phase cycle ϕ_1 = y, −y and ϕ_2 = y, y, −y, −y with constant receiver phase ϕ_r = x; when y magnetization should be mixed along the z axis the phase cycle ϕ_1 = x, −x and ϕ_2 = x, x, −x, −x with $\phi_r = \phi_1 + \phi_2$ can be used.

When applied to protons, the TOCSY sequences, in addition to the desired transfer due to scalar couplings, exhibit an undesired transfer of magnetization

Table 7
Clean TOCSY mixing schemes

Scheme	Basic element R[a]	Cycling of R[b]	Δ[c]
Clean MLEV-16	$90_x-\Delta-180_y-\Delta-90_x$	RRR̄R̄ R̄RRR̄ R̄R̄RR RR̄R̄R	τ_{90}
DISPI2-rc	$180_x-\Delta-140_x-320_{-x}-\Delta-90_{-x}-270_x-\Delta-20_x-200_{-x}-\Delta-85_{-x}-30_x-125_{-x}-\Delta-120_{-x}-300_x-\Delta-75_x-225_{-x}-\Delta-10_{-x}-190_x-\Delta-180_x-\Delta$	RR̄R̄R	τ_{144}
Clean CITY	$\Delta-180_y-2\Delta-180_y-\Delta-48_{-x}-276_x-48_{-x}-\Delta-180_y-2\Delta-180_y-\Delta$	RRR̄R̄	τ_{48}

[a] R is described by a series of RF pulses represented by their flip angles given in degrees and their phase indicated as a subscript, the pulses are separated by durations Δ.

[b] Cycling scheme for the basic element R, R̄ stands for the element R with all phases of the RF pulse changed by 180°.

[c] The theoretical length of the compensation delay Δ in the limit for large molecules is indicated as the duration of a corresponding pulse in the sequence; for example τ_{144} stands for the duration of a 144° pulse using the same power as for the mixing sequence.

via cross-relaxation (ROE). The two pathways result in resonances with opposite signs so that they can, in principle, be distinguished. However, in cases of overlapping resonances undesired cancellation effects may occur so that the elimination of the ROE contribution to [^{1}H, ^{1}H]-TOCSY spectra is desirable. Since transverse and longitudinal cross-relaxation rates for proteins differ in their sign (Eqs. (13) and (16)), a compensation scheme can be designed based on cancellation of the ROE by the NOE. The first scheme based on this idea used time periods during the mixing sequence where the magnetization stays aligned along the z axis [150]. The lengths of these time periods are adjusted for the NOE and ROE to cancel each other. Three different mixing schemes based on this scheme are in use: clean MLEV, DIPSI-2rc and clean CITY.

The MLEV-17 mixing scheme [44] was the first one modified for NOE/ROE compensation [150] (Table 7). The additional 17th pulse in MLEV-17 was added to the original MLEV-16 sequence [151] to compensate for phase and amplitude instabilities [44]. With modern NMR instruments the 17th pulse seems unnecessary and advantage can be taken of the somewhat larger bandwidth of MLEV-16. The mixing sequence MLEV-16 performs best for magnetization aligned along the spin-lock axis (y in Table 7). The more recently developed mixing sequence DIPSI-2rc [152] derives from the DIPSI sequence which has favourable magnetization transfer properties but was optimized without including the delays for the ROE/NOE compensation. DIPSI-2rc is designed for coherence transfer starting with longitudinal magnetization (Table 7). The only sequence optimized including compensation delays is clean CITY [153]. This sequence offers a slightly larger bandwidth than clean MLEV-16 and a considerable larger bandwidth than DIPSI-2rc using the same average power. Clean CITY requires the magnetization entering the mixing scheme to be along the z axis (Table 7). All three mixing sequences contain time periods Δ during which the magnetization is longitudinal to compensate for the ROE. The theoretical values of Δ for the individual sequences listed in Table 7 are the lengths of a 90°, a 144° and a 48° pulse, respectively. In practice, Δ has to be adjusted to yield the best cancellation of ROE contributions and values about twice as large as the theoretical value are often obtained [150,153].

There are mixing schemes available which do not use an explicit delay for the NOE compensation. The windowless sequence TOWNY [154] requires about 20% less peak power than MLEV-16. Another windowless sequence uses shaped pulses to reduce the average power required [155]. However, these sequences may not suppress all ROE peaks and the compensation cannot be adjusted. In contrast, the sequences which use delays for the ROE/NOE compensation allow an easy adjustment to the specific experimental needs. In addition, the power applied for non-selective 90° pulses in these pulse sequences can often be used, making power changes unnecessary. On the other hand, sequences which compensate the ROE by delay periods for NOE do not mix isotropically, i.e. transverse magnetization components along the mixing axis and perpendicular to it as well as z magnetization are not transferred with the same efficiency. Homonuclear sensitivity enhancement [156] cannot be incorporated since this method requires isotropic mixing, such as provided, for example, by a DIPSI sequence (Table 8) without trim pulses before or after the mixing.

Table 8
TOCSY mixing schemes

Scheme	Basic element R[a]	Cycling of R[b]
DISPI-2	$320_x-410_{-x}-290_x-285_{-x}-30_x-245_{-x}-375_x-265_{-x}-370_x$	RRR̄R̄
DISPI-3	$245_{-x}-395_x-250_{-x}-275_x-30_{-x}-230_x-360_{-x}-245_x-370_{-x}-340_x-350_{-x}-260_x-270_{-x}-30_x-225_{-x}-365_x-255_{-x}-395_x$	RRR̄R̄
FLOPSY-8	$46_0\ 96_{45}\ 164_{67.5}\ 159_{315}\ 130_{22.5}\ 159_{315}\ 164_{67.5}\ 96_{45}\ 46_0$	RR̄R̄R RRR̄R̄

[a] R is described by a series of RF pulses represented by their flip angles given in degrees and their phase x or −x indicated as a subscript, for FLOPSY RF phases are given in degrees.
[b] Cycling scheme using the basic element R, R̄ stands for the element R with all RF pulse phases changed by 180°.

In practical implementations TOCSY sequences use an average field strength γB_1 which should be equal to 1.0 to 1.5 times the frequency range $\Delta\nu$ in which the spins should be efficiently mixed. Higher RF field strength could improve the performance of TOCSY mixing sequences, but heating effects in biological samples limit the power that can be applied. Whereas the average sample heating can be compensated by lowering the preset probe temperature (Section 3.5.3), the heating at some spots in the sample may be much larger than average. At such spots the temperature comes closer to the denaturation temperature of the proteins than expected from the average temperature increase. As a result, protein molecules may aggregate and precipitate which not only causes a loss of protein but also disturbs the field homogeneity due the moving aggregates. The heating of the sample depends on the applied field strength and on the mixing time used. Typical mixing times for protons in proteins are in the range from 30 to 80 ms. The maximal mixing time is limited due to heating effects and relaxation. A good basis for the estimation of the required mixing time can be obtained from the time dependence of the coherence transfer by TOCSY mixing in homonuclear proton spin system [157].

When TOCSY sequences are applied to obtain coherence transfer in carbon spin systems, ROE becomes negligible and windowless sequences are used. Efficient broadband isotropic mixing schemes must be used to cover the wider chemical shift range of carbon nuclei. The most commonly used sequences are DIPSI [158] and FLOPSY [159] (Table 8). The power that can be used for the mixing sequences is limited by the hardware and by the heating of the sample. Typically field strengths around 10 kHz are applied which can achieve efficient mixing between all aliphatic carbons when the offset is set in the middle of their resonance frequency range. Aromatic and carbonyl carbons, in practice, do not take part in this mixing but their resonances are disturbed by off-resonance effects. Whereas the DIPSI sequences are rather isotropic, FLOPSY performs best when the mixing starts with magnetization along the z axis.

For an efficient TOCSY transfer in spin systems of coupled aliphatic carbons, mixing times of 10 to 20 ms are usually employed. The field strength should be chosen as large as possible without substantial sample heating, but with a γB_1 not less than the frequency range to be covered. The length of the mixing time depends on the number of carbons to be correlated and the relaxation rate of the carbons involved. The time dependence of homonuclear coherence transfer by ^{13}C isotropic mixing [160] can be used as a guideline to estimate the mixing time appropriate for the application.

4.2.2. *Homonuclear through-space transfer*

Through-space magnetization transfer can be obtained via cross-relaxation in the laboratory frame (NOE) or the rotating frame (ROE). Transfer via

Fig. 15. Schemes for a homonuclear NOESY (A) and ROESY (B) transfer segment. For short mixing times τ_m (τ_m typically smaller than 40 ms) the transfer from S magnetization to I magnetization, ΔI, is usually proportional to the S spin magnetization at the start of the mixing time, S^0 (Eq. (12)): $\Delta I = \tau_m \sigma_N S^0$ for NOESY and $\Delta I = \tau_m \sigma_R S^0$ for ROESY.

NOEs is the basis of the homonuclear NOESY experiment [8,9]. The NOESY segment consists of the mixing time τ_m which is flanked by two 90° pulses (Fig. 15(A)). The first pulse of the NOESY segment transfers transverse magnetization components into I_z states which subsequently cross-relax during τ_m with other protons in the protein (Section 2.1.6). In this way protons located within a distance of typically less than 0.5 nm can be detected. However, in the NOESY mixing time two additional transfer mechanisms may be present: chemical exchange and conformational exchange. Chemical exchange can, for example, be observed between water protons and amide protons located on the surface of a protein. In such experiments the water resonance must not be saturated before the NOESY mixing time (Section 5.3). Conformational exchange may occur in flexible parts of a protein, for example in loops connecting two secondary structure elements. When the two conformers exhibit different chemical shifts for a particular nucleus, the NOESY segment will indicate a transfer of magnetization if the conformational exchange rate is of the order of the inverse mixing time. The three possible effects detected by NOESY cannot be distinguished without further information.

When coupled spins evolve into anti-phase states before the 90° pulse that initiates the mixing time, then multiple quantum coherences may be created. Such states can be converted into undesired observable magnetization by the 90° pulse that ends the mixing time and thus must be eliminated. Proper phase cycling or, even more efficient, the application of a pulsed field gradient (PFG) during τ_m removes multiple quantum coherences with the exception of zero quantum coherence (ZQC). This has coherence level of zero, the same as the cross-relaxing z magnetization and cannot be removed by PFGs or phase cycling. ZQC, however, does not give rise to a net transfer of magnetization so that the integrated intensity over the multiplet pattern is zero. This characteristic property permits us, in principle, to distinguish NOE peaks from ZQC peaks. However, ZQCs may deteriorate the spectral quality since small NOEs may be severely distorted by overlap with ZQC resonances and an adequate integration of the NOE may no longer be possible. Thus the suppression of ZQCs is desirable. Unlike the I_z states, ZQCs precess during the mixing time and this difference can be used to reduce the intensity of ZQC resonances. A slight variation of the mixing time τ_m will not effect the NOE but will attribute a varying phase to the precessing ZQCs. Addition of individual scans with slightly differing τ_m will reduce their contribution to the detected signal [161]. A technique that randomly varies the mixing time within given limits cannot generally be recommended since the ZQC signals are smeared out and may give raise to increased t_1 noise in the spectrum [162]. Another simple scheme increments the initial mixing time τ_0 by a constant small time interval $\Delta\tau_m$ in subsequent experiments. If n NOESY experiments are measured the ZQC can be substantially reduced in a certain bandwidth [163]:

$$\tau_m = \tau_0 + n\Delta\tau_m \text{ with } \Delta\tau_m = (\Delta\nu_{min} + \Delta\nu_{max})^{-1} \tag{49}$$

where $\Delta\nu_{min}$ and $\Delta\nu_{max}$ are the minimal and maximal zero quantum frequencies that should be suppressed. The difference between τ_0 and the maximal mixing time in the experiment should not exceed τ_0 by more than 15%. About 10 experiments with different mixing times according to Eq. (49) are measured and summed together with the contribution of the first and the last spectrum scaled down by a factor of two [163]. For special applications the frequencies of the ZQC in the indirect dimension can be shifted; however, the shifted ZQC resonances may overlap with otherwise undistorted NOE peaks. A further interesting suppression technique removes zero quantum coherence with inhomogeneous adiabatic pulses [164] during the transfer from transverse to longitudinal magnetization. This method requires rather long transition periods of approximately 30 ms between fully transverse and cross-relaxing z states, a time period which for many applications is prohibitively long.

The transfer segment based on ROE (Fig. 15(B)) consists of a spin-lock sequence with length τ_m during which cross-relaxation in the rotating frame occurs. The sequence at first sight seems identical to a TOCSY sequence but for ROESY it suffices to apply only continuous wave (CW) RF irradiation at low power instead of the multipulse broadband inversion sequence necessary for TOCSY transfer. This results in only small interferences between ROESY and TOCSY which are much less severe than in the case of the TOCSY segment. A special suppression

scheme is often not used since the bandwidth for TOCSY transfer with a low-power CW spin-lock becomes very small. If a still better suppression is required, techniques exist which reduce the residual TOCSY transfer in a ROESY sequence. The simplest method sets the offset for the ROESY spin-lock at one edge of the spectral range making the TOCSY transfer even more inefficient. Another approach applies a continuous frequency sweep to the carrier frequency of the spin-lock during its application [165] which strongly attenuates TOCSY contributions but hardly affects the ROE transfer. A third technique uses a special multipulse sequence for the suppression of TOCSY contributions [166]; however, the ROESY transfer with this scheme happens at a reduced rate which makes the sequence inefficient for most applications with proteins.

The RF field strength γB_1 used in ROESY corresponds to about one-quarter of the frequency range $\Delta\nu$ which contains the signals of interest. The low RF field strength used, which is usually not more than 2.5 kHz, means that ROESY may suffer from off-resonance effects which cause varying transfer efficiency across the spectrum. The offset effects can be eliminated by two 90° pulses which bracket the spin-lock mixing sequence [167]. This compensation introduces a phase distortion in the spectrum which is to a good approximation linear unless the frequency difference between two nuclei is much larger than the field strength γB_1 of the applied spin-lock field. An alternative scheme replaces the two 90° by two 170° pulses with just twice the power of the spin-lock, which does not introduce a phase distortion, but does not work well for offsets larger than the field strength applied [168]. The spatial inhomogeneity of the applied RF spin-lock field destroys all orders of multiple quantum coherences which may be present at the beginning of τ_m and only zero quantum coherences will pass the mixing process. In the reference frame defined by the spin-lock field, zero quantum coherence corresponds to anti-phase magnetization in the normal rotating frame or in the laboratory frame of reference. These signals can be suppressed using procedures corresponding to those applied in the NOESY sequence.

In applications with large molecules the mixing times in NOE and ROE experiments must be kept rather short, otherwise the occurrence of spin diffusion (Section 2.1.6) will make the distance information obtained unreliable. The ROE sequence generates less spin diffusion artefacts than the NOE segment since the relayed magnetization has opposite sign and can be reduced by direct transfer [169]. For the NOE segment direct and relayed transfers have the same sign. To reduce spin diffusion contributions in selected frequency ranges in NOE spectra, two techniques were developed. One technique uses the ROE effect to reduce contributions by spin diffusion [170,171] and the other uses selective inversion of part of the resonances during the mixing time [172,173].

ROE and NOE transfers provide very similar information based on different processes. The cross-relaxation in the two mixing schemes, however, produces signals of different sign for large molecules (Eqs. (13) and (16)). On the other hand, contributions from chemical and conformational exchange keep the same sign irrespective of the mixing scheme. Hence chemical and conformational exchange can be distinguished from cross-relaxation in ROE spectra but not in NOE spectra. Based on this difference, special experiments were developed which compensate NOE contributions by ROE and allow the detection of chemical exchange free from interferences from cross-relaxation [174].

4.2.3. Heteronuclear transfer

The efficiency of through-bond coherence transfer steps depends on the size of the coupling constants. Consequently, using heteronuclear couplings is attractive because they are often much larger than proton–proton coupling constants (Fig. 5). The use

Fig. 16. Schemes for heteronuclear polarization transfer starting from heteronuclear anti-phase magnetization. Narrow vertical bars stand for 90° RF pulses. The cartesian product operators indicated in the figure describe a typical coherence transfer step to heteronuclear multiple quantum (A) and to heteronuclear single quantum coherence (B). Transformation properties in the shift operator basis are given in Table 9.

Table 9
Heteronuclear through-bond transfer as shown in Fig. 16

Fig. 16	Initial state	Resulting product operators describing the transformation properties of the sequence[a]
A	$2I_zS_z$	$i(I_zS^+ - I_zS^-) = -2I_zS_y$
	$2I^+S_z$	$i(I^+S^+ - I^+S^-) = -2I_xS_y - 2iI_yS_y$
	$2I^+S^+$	$(I^+S^- + I^+S^+) + 2iI^+S_z = 2I_xS_x - 2I_yS_z + 2iI_xS_z + 2iI_yS_x$
B	$2I_zS_z$	$(I^+ - I^-)(S^- - S^-)/2 = 2I_yS_y$
	$2I^+S_z$	$i(I^- + I^+ + 2iI_z)(S^+ - S^-)/2 = -2I_xS_y - 2iI_zS_y$
	$2I^+S^+$	$(I^- + I^- + 2iI_z)(S^- + S^+ + 2iS_z)/2 = 2I_xS_x - 2I_zS_z + 2iI_xS_z + 2iI_zS_x$

[a] The resulting product operators are indicated in the shift and in the cartesian basis.

of heteronuclear coupling constants, however, requires the protein to be labelled with ^{15}N and/or ^{13}C isotopes. In analogy to the homonuclear COSY segment, coherence transfer occurs through anti-phase states (Fig. 16). For example, starting with heteronuclear anti-phase coherence prepared by an evolution segment (Fig. 12(A)), one 90° pulse on S suffices to transfer anti-phase I spin coherence into two-spin coherence (Fig. 16(A), Table 9). A 90° pulse on both the I and the S spins transfers anti-phase I spin coherence into an anti-phase S spin coherence (Fig. 16(B), Table 9). Heteronuclear coherence transfer is the key segment in heteronuclear multidimensional experiments used with ^{15}N- and/or ^{13}C-labelled proteins.

A very important point to be considered in the context of coherence transfer schemes is the S/N obtainable from a particular experiment. The S/N depends on the polarization obtainable with the nuclei on which the pulse sequence starts and it depends on the size of the magnetization during detection of the signal. In other words, the S/N depends on $\gamma_e B_o$ and on γ_d with the gyromagnetic ratios γ_e and γ_d of the excited and the detected nuclei, respectively (Table 1). Furthermore, the induced voltage is proportional to the resonance frequency $\omega_o = \gamma_d B_o$ of the nuclear species detected. On the other hand, the noise contributed by the detection circuitry is proportional to the square root of the measured bandwidth. The necessary bandwidth increases linearly with ω_o and hence the noise is increased proportional to $\sqrt{\omega_o}$. Combining all these factors the S/N fulfils the following proportionality

$$S/N \propto \gamma_e \gamma_d^{3/2} B_o^{3/2} \tag{50}$$

Eq. (50) demonstrates the benefits that can be obtained when the nuclei excited at the start of the pulse sequence and/or the nuclei detected are protons [175]. In addition, Eq. (50) shows that coherence transfer steps to other nuclei between the excitation and detection influence the S/N only through transfer efficiency and relaxation during the transfer.

The segment most frequently used to transfer magnetization from one nuclear species to another and to achieve the sensitivity improvement described by Eq. (50) is known under the acronym INEPT [45] which stands for "insensitive nuclei enhanced by polarization transfer". The INEPT scheme (Fig. 17(A)) combines the basic segments shown in Figs. 12(A) and 16(B). The discussion of the different representations used to describe NMR experiments (Fig. 3) is based on an INEPT-type sequence. A full

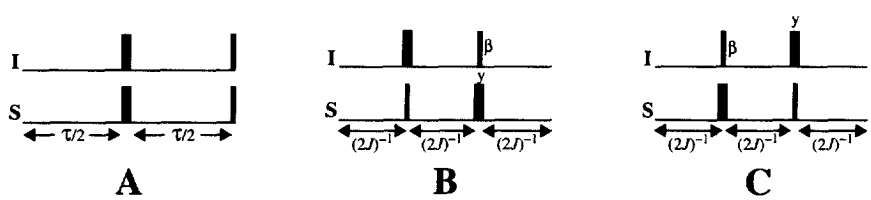

Fig. 17. Schemes for heteronuclear polarization transfer in I_nS spin systems. (A) INEPT segment using a heteronuclear single quantum coherence transfer step (HSQC). (B) and (C) DEPT segments where the pulse labelled β has varying flip angle β. (B) represents the coherence transfer from I to S spins and (C) from S to I spins. Table 10 presents the transformation properties of these segments. The contribution of the natural polarization of the destination spin can be subtracted from the measured signal by proper phase cycling (see text).

Table 10
INEPT and DEPT coherence transfer segments as shown in Fig. 17

Fig. 17	Initial state	Relevant product operators describing the transformation properties of the sequence[a]
A	I_x or I^+	$-2S_yI_z \sin(\pi J\tau) = i(I_zS^+ - I_zS^-)\sin(\pi J\tau)$
	S_x or S^+	$-\sum_{k=1}^{n} 2I_{ky}S_z \cos^{n-1}(\pi J\tau)\sin(\pi J\tau) = i\sum_{k=1}^{n}(I_k^+ S_z - I_k^- S_z)\cos^{n-1}(\pi J\tau)\sin(\pi J\tau)$
B	I_x or I^+	$-S_x \cos^{n-1}\beta \sin\beta = i(S^+ + S^-)\cos^{n-1}\beta \sin\beta/2$
C	S_x or S^+	$-\sum_{k=1}^{n} I_{kx}\cos^{n-1}\beta \sin\beta = -\sum_{k=1}^{n}(I_k^+ + I_k^-)\cos^{n-1}\beta \sin\beta/2$

[a] Only magnetization components transferred between I and S spins are shown. The natural magnetization of the destination spins is assumed to be subtracted from the resulting signal by proper phase cycling (see text). The expressions are valid for I_nS spin systems like the CH, CH_2 and CH_3 moieties in polypeptides. The scalar homonuclear coupling between the I spins is assumed to be much smaller than the heteronuclear coupling J between the I and S spins. The homonuclear couplings among the I spins are thus neglected in the product operator calculations. The resulting product operators are indicated in the shift and in the cartesian basis.

analysis of the INEPT scheme must include at least the spin systems IS, I_2S and I_3S which are of special interest since they represent the moieties $^{15}N^1H$, $^{13}C^1H$, $^{13}C^1H_2$ and $^{13}C^1H_3$ in labelled macromolecules. The much smaller homonuclear couplings are often neglected for the analysis of INEPT in terms of the product operator formalism (Table 10). The efficiency of the transfer depends on τ (Fig. 17(A)). A single value for τ exists for a simultaneous optimal transfer from I to S spins for all the three multiplicities IS, I_2S and I_3S. However, for the transfer from in-phase S magnetization to I magnetization τ depends on the multiplicity (Fig. 18). For a simultaneous transfer for all three multiplicities a value for τ of $0.33/J$ provides a good compromise.The different transfer

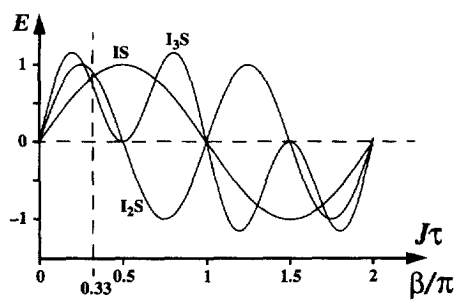

Fig. 18. Coherence transfer efficiency E for heteronuclear polarization transfer in the spin system IS, I_2S and I_3S versus $J\tau$ for the INEPT or β/π for the DEPT segment. J is the scalar coupling constant between the nuclei I and S, τ the period during which the state evolves due to the coupling J and β is the flip angle of the pulse with variable length in the DEPT sequence (Fig. 17). The value 0.33 for $J\tau$ or β/π indicates a compromise value often used when simultaneous in-phase magnetization transfer to or from carbon nuclei in CH, CH_2 and CH_3 moieties is required.

functions allow editing of spectra according to the multiplicities of the resonance lines (Fig. 18). For example, in a carbon spectrum the resonances of the CH, CH_2 and CH_3 groups can be separated into different spectra [16,24,26].

For best performance INEPT requires the coupling constants used to prepare the coherence transfer step to have the same value, a condition often fulfilled for spin systems in proteins. For cases with sizeable variations of the heteronuclear coupling constants used for the polarization transfer, an alternative polarization transfer scheme, DEPT [176], offers superior performance at the cost of a longer sequence. DEPT stands for distortionless enhancement by polarization transfer. In contrast to INEPT the DEPT sequence achieves spectral editing on the basis of spectra measured with different flip angles for the pulse β in the sequence (Fig. 17(B), Table 10) and not by changing a delay period. The complete DEPT segments in Fig. 17(B) and 17(C) transfer in-phase magnetization into in-phase magnetization. This is in contrast to the INEPT segment shown in Fig. 17(A) where the sequence starts with in-phase magnetization and ends with transferred magnetization in anti-phase, which must first be refocused by the segment shown in Fig. 12(A) with the refocusing delay optimized according to Fig. 18. For heteronuclear polarization transfer in proteins, the INEPT segment is used much more frequently than DEPT since the coupling constants used are fairly homogeneous, the possible distortions are less disturbing for large linewidths, and quite often the faster transfer into anti-phase states is preferred to minimize relaxation losses. In addition,

even for an in-phase magnetization transfer, the duration of an INEPT based sequence is shorter than DEPT.

Multidimensional NMR experiments often contain several INEPT steps. For the implementation of consecutive INEPT segments two different methods exist: "out-and-back" and "out-and-stay" (or "straight-through") experiments. The first type retains anti-phase magnetization to the nucleus where the magnetization originates. A further INEPT step brings the magnetization back to the original nucleus. In an "out-and-stay" transfer the anti-phase magnetization obtained after the transfer is refocused on the destination nucleus and finally measured on a nucleus different from the one on which the polarization transfer started. Experiments using the "out-and-back" technique often offer better sensitivity than "out-and-stay" experiments since the relaxation of transverse magnetization on fast relaxing nuclei can be minimized due to the shorter transfer times.

In practical implementations of the polarization transfer sequences discussed, a few points deserve consideration. When transferring magnetization from *I* spins to *S* spins, the natural *S* spin polarization often interferes with the measurement and must be removed, for example, by applying the two-step phase cycle (x, − x) to one of the 90° pulses applied to the *S* spins before the transfer and subtracting the signals thus obtained. In the DEPT segment the phase of the pulse β is often cycled using this scheme. Furthermore, to make sure that the magnetization detected was transferred through the desired heteronucleus *S*, the 90° *S* pulse accomplishing the polarization transfer is cycled in the same way. For optimal polarization transfer, the length of the period to obtain anti-phase magnetization is often chosen to be shorter than dictated by the *J* coupling involved to counteract relaxation. When a polarization transfer step immediately follows an evolution time only half of the magnetization, either the sine or the cosine component created due to chemical shift evolution, can be transferred. However, in some cases the application of a sensitivity enhancement scheme using a heteronuclear multiple quantum state retains both components [177] (Section 4.5.3). The best enhancement is achieved for two-spin systems like the $^{15}N^{1}H$ moiety.

In analogy to TOCSY transfer in homonuclear spin systems, the heteronuclear *J* cross-polarization

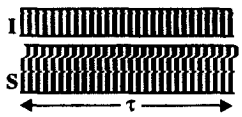

Fig. 19. Pulse sequence segment used to obtain heteronuclear Hartmann–Hahn polarization transfer. The hatched rectangles indicate continuous application of RF pulses. The strengths of the two different RF fields applied to the *I* and *S* spins must fulfil the Hartmann–Hahn condition given in Eq. (10). The magnetization transfer obtained for a heteronuclear two-spin system is described in Eq. (11).

experiment [178] (Fig. 19) presents an alternative to coherence transfer via anti-phase states. Three major differences distinguish heteronuclear Hartmann–Hahn (HEHAHA) experiments from homonuclear TOCSY: for HEHAHA the RF fields applied at different frequencies must match the condition given in Eq. (10), the heteronuclear transfer is a factor of two slower (Eqs. (9) and (11)) and heteronuclear ROESY contributions can be neglected. Complete magnetization transfer from the *I* spins to the *S* spins in a heteronuclear two-spin system requires the same amount of time as the in-phase transfer via an INEPT scheme. A full transfer into anti-phase magnetization cannot be obtained (Eq. (11)). Therefore, heteronuclear *J* cross-polarization mainly presents an alternative for the "out-and-stay" type of experiments, whereas for the more frequently used "out-and-back" experiments the INEPT sequence is usually more efficient. HEHAHA experiments can have an advantage over INEPT when simultaneous homonuclear and heteronuclear coherence transfers are desired. Investigations on double and triple HEHAHA experiments in comparison to INEPT-type experiments show, however, only a small overall advantage of the cross-polarization method [179].

When implementing HEHAHA sequences the Hartmann–Hahn condition must be fulfilled (Eq. (10)). The best matching can be obtained when the frequencies for the nuclei are delivered from the same RF coil, since then the RF homogeneities of the two fields are the same. HEHAHA sequences contribute to the heating of the sample and of the probe circuitry which may detune the coil and, hence, affect the Hartmann–Hahn transfer efficiency. Historically, multipulse broadband decoupling sequences were used for heteronuclear cross-polarization, but the conditions for broadband cross-polarization are more

restrictive than those for decoupling and the best sequences for the former will be efficient for the latter but not vice versa. The most frequently used HEHAHA mixing sequences are DIPSI-2 and DIPSI-3 [158] (Table 8), but alternative sequences have been proposed [180,181]. HEHAHA experiments can also be applied band selectively using trains of shaped pulses [182].

4.3. Decoupling sequences

The scalar coupling between nuclei finds frequent application in the manipulation of spin states or the determination of dihedral angles [42]. On the other hand, couplings may complicate spectra and reduce the maximal signal intensity. If only the spin state at the end of a time period τ is of interest, the evolution due to J coupling between two nuclei can be refocused by a 180° pulse applied to one nucleus in the middle of τ (Section 4.1). Fig. 20(A) shows a more general case where I_k and H_k represent spins from the same species whereas S_k stands for spins from a different species. The spins I_k are decoupled from the S_k spins by a 180° pulse on the S_k spins. At the same time a frequency-selective 180° inversion pulse applied to the H_k spins decouples the I_k spins from the H_k spins. Fig. 20(B) presents a very special decoupling sequence that decouples two spins of the same nuclear species but still maintains the evolution due to their chemical shifts [183]. Starting with y magnetization the analysis of this sequence with the product operator formalism shows that at the end of a time period $2t$, the evolution due to J coupling is refocused and both spins have evolved due to their chemical shifts for a time period t.

If decoupling must be maintained over extended time periods, for instance during the acquisition of the signal, continuous multipulse sequences are applied (Fig. 20(C)). Much effort has been expended to develop heteronuclear decoupling sequences that increase the effective decoupling bandwidth without increasing the RF power dissipation in the sample while keeping the residual splitting much smaller than the linewidth of the resonances observed. The first heteronuclear broadband decoupling technique to appear in the literature applied noise irradiation at the frequency of the undesired coupling partner [184]. Since then, heteronuclear broadband decoupling techniques have improved enormously, initially through various forms of composite pulse decoupling [151,158,185,186] and more recently using methods based on adiabatic fast passage [187–191]. Despite their increased efficiency, decoupling sequences very likely increase the average sample temperature; this effect should be compensated by lowering the preset temperature (Section 3.5.3). Decoupling sequences applied during non-constant time periods t in multidimensional experiments may result in increasing average sample temperatures with increasing values of t which will cause severe distortions in the spectrum. A constant sample temperature over the whole experiment can be obtained by decreasing a continuous wave irradiation after acquisition concomitant with the increasing time period t [192].

The most frequently used decoupling schemes are WALTZ [185], GARP [186], DIPSI [158] and more recently adiabatic schemes such as WURST [191]. A measure of the efficiency of a particular decoupling scheme is given by the frequency range decoupled by a certain average field strength. For example, an RF

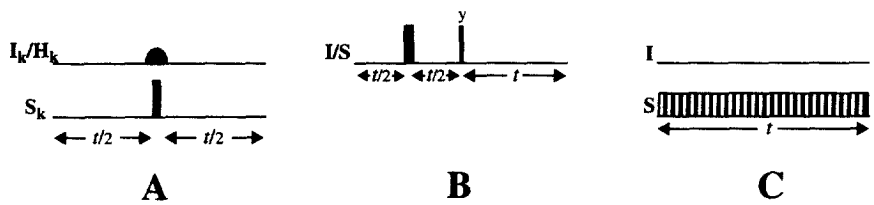

Fig. 20. Decoupling schemes. (A) Transverse magnetization of the spins I_k is decoupled from the S_k spins by a 180° pulse applied to the S_k spins. At the same time a frequency-selective 180° inversion pulse on the H_k spins which are of the same species as the I_k spins decouples the I_k spins from the H_k spins. (B) Special scheme for a homonuclear two-spin system that decouples the two spins I and S from each other and still maintains chemical shift evolution of both spins during a period t. The initial state $I_y + S_y$ is transformed to $-I_x \sin(wt) + I_y \cos(wt) - S_x \sin(\Omega_I) + S_y \cos(\Omega_I)$ at the end of the sequence. (C) The I spins are decoupled from the S spins by a broadband composite pulse decoupling sequence (Table 11).

Table 11
Composite pulse decoupling schemes

Scheme	Basic element R[a]	Cycling of R[b]	$\Delta\nu$[c]	Length of R[d]
Waltz-16	$90_x-180_{-x}-270_x$	RRR̄R̄ R̄RRR̄ R̄R̄RR RR̄R̄R	± 1.0	540
GARP-1	$30.5_x-55.2_{-x}-257.8_x-268.3_{-x}-69.3_x-62.2_{-x}-85.0_x-91.8_{-x}-134.5_x-256.1_{-x}-66.4_x-45.9_{-x}-25.2_x-72.7_{-x}-119.5_x-138.2_{-x}-258.4_x-64.9_{-x}-70.9_x-77.2_{-x}-98.2_x-133.6_{-x}-255.9_x-65.5_{-x}-53.4_x$	RRR̄R̄	± 2.4	2857
DISPI-2	$320_x-410_{-x}-290_x-285_{-x}-30_x-245_{-x}-375_x-265_{-x}-370_x$	RRR̄R̄	± 0.6	2590
DISPI-3	$245_{-x}-395_x-250_{-x}-275_x-30_{-x}-230_x-360_{-x}-245_x-370_{-x}-340_x-350_{-x}-260_x-270_{-x}-30_x-225_{-x}-365_x-255_{-x}-395_x$	RRR̄R̄	± 0.8	4890

[a] R is described by a series of RF pulses represented by their flip angles given in degrees and their phase x or −x indicated as a subscript.
[b] Cycling scheme for the basic element R; R̄ stands for the element R with all phases of the RF pulse changed by 180°.
[c] Decoupled bandwidth $\Delta\nu$ given in units γB_1 of the applied RF field strength.
[d] Total length of the element R given as a pulse angle in degrees.

field of 4 kHz decouples a frequency range of 1.2 kHz with noise decoupling, 7.2 kHz with WALTZ-16, 19 kHz with GARP-1 and 78 kHz with WURST decoupling [193]. Multipulse decoupling sequences consist of a basic element R which is repetitively applied in combination with the element R̄. In the element R̄ all the phases of the RF pulse are shifted by 180° for the improvement of the decoupling performance [151]. In Table 11 composite pulse decoupling sequences are represented by their basic segment R given by a train of RF pulses which are indicated by their flip angles in degrees. The pulses are applied with phase x or −x which is indicated as a subscript.

The modern repetitive heteronuclear decoupling schemes, in general, are susceptible to the problem of cycling sidebands. Viewed in the time domain, decoupling consists basically of a repeated refocusing of the divergence of magnetization vectors due to the spin–spin coupling. Unless the focusing is precise and the sampling of the observed signal is exactly synchronized with the focus points, decoupling introduces spurious modulations into the free induction decay. The Fourier transform of these oscillatory artefacts consists of pairs of modulation sidebands flanking the resonance frequency and separated from it by the cycling frequency. These cycling sidebands may severely distort the quality of spectra with very different peak intensities such as NOESY spectra [194]. Cycling sidebands can be minimized using high decoupling power, but this conflicts with the goal of achieving the desired decoupling bandwidth with lowest possible sample heating. Different techniques to reduce sideband intensities have been developed [195,196] but, depending on the application, only certain techniques may give sufficient reduction. An almost complete suppression can be obtained even at low decoupling power using a WURST decoupling scheme, ECO-WURST [194], with two different decoupling powers which are applied for a variable length of time in different scans. The ECO-WURST scheme permits, for example, the detection of weak cross-peaks close to strong direct correlation peaks in multidimensional heteronuclear decoupled ^{1}H-detected NMR experiments.

In contrast to conventional composite pulse decoupling schemes (Table 11), efficient adiabatic decoupling schemes cover chemical shift ranges that far exceed those required for ^{13}C on a 800 MHz spectrometer [193]. However, adiabatic decoupling schemes may have considerable sideband intensities which are even more obstructive when the adiabatic condition is not properly fulfilled and when the pulse repetition rate is insufficiently high in comparison with the coupling constant. The sweep rate is therefore a compromise between two requirements: it must be slow enough to satisfy the adiabatic condition given in Eq. (26) and fast enough to make the product of the coupling constant J and the sweep duration approximately 0.2. A guide for optimizing the decoupling performance by choosing the most suitable instrumental settings has been published for WURST decoupling [193]. As an example, WURST decoupling with an average RF field strength of 4 kHz using a

frequency sweep over 70 kHz with a rate of 145 MHz s^{-1} decouples a bandwidth of 30 kHz with minimal sidebands if the coupling constant does not exceed 150 Hz.

One important criterion for the selection of decoupling sequences is the requirement to limit the heating of the sample and thus the widest bandwidth per unit power is often favoured. GARP and schemes based on adiabatic pulses offer wide decoupling bandwidths but also suffer from considerable cycling sideband intensities. At the cost of a smaller decoupling bandwidth, WALTZ provides smaller sidebands and very small residual splittings of the decoupled resonances. The latter feature is less important in protein spectra with their inherently broad lines. In systems requiring relatively small decoupling bandwidths which have homonuclear couplings among the decoupled spins, DIPSI sequences may outperform WALTZ and GARP especially at low power levels [158]. DIPSI was optimized including the effect of spin–spin coupling among the spins irradiated.

Not only are multipulse decoupling sequences used for heteronuclear decoupling but they find application as narrow band homonuclear decoupling schemes. The primary goal in these applications is to decouple a narrow range of frequencies with minimal disturbance outside this region. Examples are the decoupling of amide proton resonances from α protons or the decoupling of aliphatic carbon resonances from carbonyl carbons. For homonuclear band-selective decoupling, three different techniques are used. In the first method the high-power 180° pulses employed in evolution schemes for decoupling purposes can be replaced by selective pulses with a box-like inversion profile resulting in a band-selective decoupling (Fig. 20(A)). The same class of pulses can also be applied to obtain homonuclear decoupling during the acquisition of the signal [197], but this requires interleaved acquisition (Section 2.4.3). A second method uses composite pulse decoupling schemes replacing the high-power rectangular pulses normally used with low-power shaped pulses thus obtaining a composite pulse decoupling sequence with narrow band- width [198–200]. A third method adapts adiabatic decoupling schemes for narrowband homonuclear decoupling [201]. All homonuclear decoupling sequences may cause phase and frequency shifts for the resonances outside the irradiated bandwidth by non-resonant effects which are summarized in Eqs. (21)–(23).

4.4. Pulsed magnetic field gradients

The use of pulsed magnetic field gradients (PFGs) in high-resolution NMR has become a routine technique in the last few years [71,72]. This breakthrough is due to the availability of shielded gradient coils which improve the performance of PFGs dramatically. Older gradient coil designs generated eddy currents which compromised field homogeneity and required unacceptable periods to decay. Shielded gradients generate much smaller eddy currents resulting in substantially reduced recovery times. PFGs perform a variety of functions in pulse sequences. They can be used for reduction of phase cycling which saves measurement time for sufficiently concentrated samples, for elimination of experimental artefacts, for suppression of t_1 noise, for suppression of strong solvent lines and for measuring diffusion properties. Gradients up to 0.3 T m^{-1} (30 G cm^{-1}) are usually sufficient for most of these applications. Much stronger gradients can distort the NMR spectrum unless special techniques [68] and/or long recovery times are used after the application of a PFG. The applications of PFGs can be grouped into three different categories which are discussed briefly in the following: use of spatial frequency dependence, destruction of coherences and selection of coherences.

During the application of a PFG, the resonance frequency of a nucleus depends on its spatial location (Eq. (30)). The signal defocused by a PFG cannot be completely refocused by a second gradient if the molecules have diffused to another location between the two gradients. This effect finds direct application in diffusion measurements but, of course, is always present when gradients are used. This can lead to

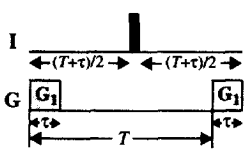

Fig. 21. Gradient scheme for diffusion measurements. A series of experiments is performed with different gradient strength G_1 keeping the time period T constant to exclude interferences from relaxation processes. With increasing values for G_1 the signal intensities obtained decay exponentially according to Eq. (51).

accidental signal loss when defocusing and refocusing gradients are separated by a long time period. Fig. 21 shows a typical sequence used for measuring diffusion constants. Translational diffusion in liquids during a time interval T results in different NMR signal intensities depending on whether or not T is bounded by two identical PFGs with strength G_1 (Fig. 21). The signal intensities S with and S_0 without gradients fulfil the relation [67]

$$\ln(S/S_0) = -\gamma^2\tau^2G_1^2(T - \tau/3)D \quad (51)$$

where D is the translational diffusion coefficient, γ the gyromagnetic ratio (Table 1), τ the length of the gradient, and T the time period between the start of the two gradients (Fig. 21). Depending on the solvent conditions, water molecules diffuse about 10 to 50 times faster than proteins in the molecular weight range from 5 to 25 kDa. For example, the self-diffusion constants of water molecules and of the protein BPTI in a highly concentrated 20 mM BPTI solution in 90%H_2O/10%D_2O at 4°C are 1.0×10^{-9} and 4.7×10^{-11} $m^2 s^{-1}$, respectively [68,202]. Diffusion weighting of the NMR signal can be used to separate resonances of large and small molecules [202,203]. In another application, diffusion constants measured with NMR are used to characterize the aggregation state of proteins [204,205].

Very frequently, PFGs are used to destroy unwanted transverse magnetization where the magnetization of interest is in a z state. If sufficient time is allowed after the gradient for the field homogeneity to recover, the implementation is simple and only accidental refocusing of unwanted magnetization must be prevented. This application does not require special linearity and reproducibility of the gradients. Fig. 22 presents typical pulse sequence segments used to destroy undesired magnetization components. The segment in Fig. 22(A) destroys all transverse magnetization except zero quantum coherence. The segment in Fig. 22(B) acts like the one in Fig. 22(A) and in addition destroys all magnetization components originating from z states which are not properly inverted by the 180° pulse. Fig. 22(C) presents a very popular application in heteronuclear coherence transfer steps where the magnetization of interest is in a z ordered state during the application of the gradient. In this context it is worth noting that, for example, two-spin order, I_zS_z, can relax substantially faster than, for example, S_z magnetization due to additional contributions to relaxation from proton–proton dipolar

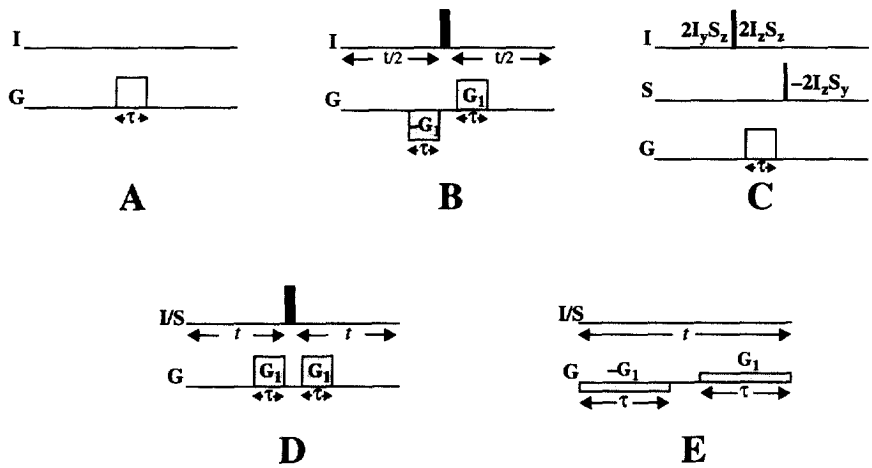

Fig. 22. Gradient schemes that destroy unwanted signals. (A) All magnetization components are destroyed except for z magnetization, z ordered states and zero quantum coherences. (B) This sequence destroys the same states as (A) and in addition all magnetization components created by a non-ideal 180° inversion pulse on z states. (C) Scheme frequently used to destroy unwanted magnetization components in a heteronuclear polarization transfer step, the desired magnetization is in a z ordered state during the gradient. The cartesian product operators indicate typical states which can survive the PFG. (D) Selection of all magnetization components that are properly inverted or refocused by the 180° pulse. (D) The scheme uses very weak gradients and leaves all magnetization components practically unchanged but prevents radiation damping of strong solvent resonances.

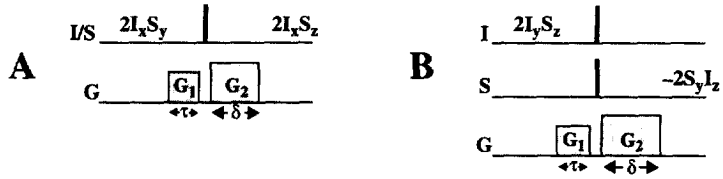

Fig. 23. Examples of schemes that select the desired signal by the application of PFGs. The transformation properties for I^+ states are given in Table 12. (A) Selection of a homonuclear coherence transfer pathway from a two-quantum to a single-quantum state. The product between the strength of the gradient and its duration must fulfil the equation $G_2\delta = 2G_1\tau$. (B) Selection of a heteronuclear coherence transfer step where $G_2\delta = \gamma_I G_1\tau/\gamma_S$. The cartesian product operators indicated in (A) and (B) describe a typical coherence transfer step selected by the PFGs.

interactions [206]. For this reason, gradient and recovery delay should be kept sufficiently short to prevent relaxation losses. Fig. 22(D) and 22(E) show segments which not only destroy undesired magnetization but at the same time retain desired transverse magnetization. This requires exactly reproducible gradients which refocus the magnetization of interest. Fig. 22(D) shows an efficient alternative to phase cycles such as EXORCYCLE (Section 2.2.1). This segment retains only transverse and longitudinal magnetization components that are properly inverted or refocused by the 180° pulse. The segment in Fig. 22(E) restores all magnetization at the end of the time period t and ideally leaves all magnetization components unchanged. Using weak gradients, the segment prevents only radiation damping of very intense solvent resonances [90].

The third category of applications of PFGs, coherence selection, requires linear gradient amplifiers and precisely reproducible gradients where the absolute strength for positive and negative gradients match exactly. Otherwise, tedious optimization procedures are necessary to obtain the maximal signal. Fig. 23 presents typical applications of PFGs for coherence selection and Table 12 summarizes the characterization of these segments using the product operator formalism.The segment shown in Fig. 23(A) demonstrates the selection of a transfer from a double quantum to a single quantum state by PFGs [207]. Double quantum coherence before the 90° pulse is defocused by a gradient as described by Eq. (30). Refocusing the magnetization in a single quantum state requires a PFG with the product $G_2\delta$ of the strength G_2 and duration δ of the gradient to be double compared to the first PFG (Fig. 23(A)). The segment in Fig. 23(B) uses the same principle for the selection of anti-phase magnetization during a heteronuclear coherence transfer step. A PFG is applied to anti-phase magnetization of spin I. After the coherence transfer step to anti-phase S spin magnetization, a second PFG with the appropriate product $G_2\delta$ must be applied to refocus the desired magnetization. The spread of resonance frequencies introduced during a PFG depends on the gyromagnetic ratio γ (Eq. (30)) and hence the condition $G_2\delta = \gamma_I G_1\tau/\gamma_S$ must be fulfilled for the segment in Fig. 23(B). In a more general case the sum of all the exponential factors described by Eq. (30) which are introduced by gradients during the pulse sequence must vanish to result in observable magnetization [71,72].

The application of PFGs for the selection of coherence pathways cannot retain positive and negative coherence levels simultaneously (Eq. (30)) which results in a loss of half of the signal. Thus, one coherence selection step using gradients reduces the obtainable S/N by $\sqrt{2}$ compared to the selection by a phase cycling scheme. When applying a PFG for coherence selection during an evolution time of a multidimensional experiment, the requirement to

Table 12
Coherence selection by PFGs as shown in Fig. 23

Fig. 23	Initial state	Resulting product operators describing the transformation properties of the sequence[a]
A	I^+	0
	$2I^+S_z$	0
	$2I^+S^+$	$iS^-I_z e^{-i(\omega+\Omega)\tau+i\omega\delta} + iI^-S_z e^{-i(\omega+\Omega)\tau+i\Omega\delta}$
B	I^+	0
	$2I^+S_z$	$S^-I_z e^{-i\omega\tau+ik\Omega\delta}$ with $k = \gamma_I/\gamma_S$
	$2I^+S^+$	0

[a] The coherence selection is described from the start of the first to the end of the second PFG neglecting scalar couplings.

retain both coherence levels cannot be fulfilled and pure phase absorptive spectra cannot be obtained (Section 2.5). Pathways for both positive and negative coherence levels can only be obtained using a second scan with the inversion of the sign of one of the gradients used for the selection. In some experimental schemes, part of the detectable magnetization can be destroyed to obtain pure phase spectra, but such a procedure reduces the sensitivity even more [208]. On the other hand, enhancement schemes exist for gradient-selected coherence pathways (Section 4.5.3).

In practical implementations very long and/or very strong PFGs may still require long recovery times compared to the relaxation of transverse magnetization and may cause signal loss. In such situations a pre-emphasis unit may be useful to reduce recovery times. This unit shapes the gradient pulses, for example using exponential functions with different time constants and amplitudes. The pre-emphasis unit compensates the transient response induced in the system when switching on or off magnetic field gradients resulting in shorter recovery times. The adjustment requires manipulations which are similar to shimming a magnet and may require substantial time and experience. The complex spatial and time dependencies of the induced transient effects often exclude their complete compensation. When working with triple axis gradients a pre-emphasis may be desirable even for moderate gradient strengths because the different gradient coils can exhibit interactions resulting in longer recovery times compared to a single axis gradient system.

4.5. Combinations of basic segments

4.5.1. The HSQC and the HMQC scheme

The heteronuclear single quantum coherence (HSQC) transfer and the heteronuclear multiple quantum coherence (HMQC) transfer are the two most frequently used schemes for coherence transfer in heteronuclear multidimensional NMR experiments. Both schemes include two coherence transfer steps separated by an evolution period t_1 to sample the resonance frequencies of one nuclear species (Fig. 24). The HSQC consists of two INEPT steps (Fig. 17(A)) leading to heteronuclear single quantum coherences during t_1, whereas the coherence transfer steps (Fig. 16(A)) used in HMQC create multiple quantum coherences which evolve during t_1. At least two coherence transfer steps are required in heteronuclear coherence transfer experiments, since best sensitivity can usually be obtained if the nucleus with the highest gyromagnetic ratio is excited and detected (Eq. (50)).

The two schemes differ in important features [209]. Because the HMQC has a much smaller number of RF pulses it is less prone to pulse imperfections. In addition, multiple quantum coherences may have better relaxation properties than corresponding single quantum states, an advantage that can be exploited by using an HMQC transfer. The improved relaxation properties are explained by the different dependence on the spectral density at zero frequency $J(0)$ (Section 2.1.4). When an HMQC sequence is applied to a two-spin system, zero quantum (ZQC) and double quantum coherences (DQC) exist during the evolution period. The transverse relaxation for ZQC and DQC based on dipolar interactions does not depend on $J(0)$ [16,29], in contrast to the single quantum coherence present in the INEPT sequence where the dependence on $J(0)$ contributes a major part to the relaxation. However, when more than two spins are considered the multiple quantum states can lose the relaxation advantage due to dipolar interactions with additional protons [210]. Furthermore, the HMQC scheme may

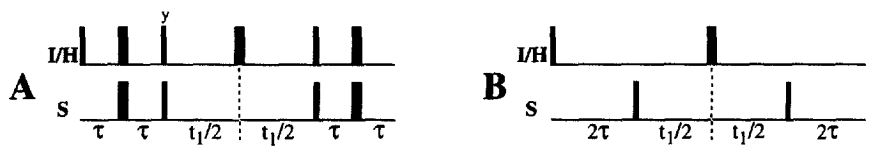

Fig. 24. Coherence transfer schemes transferring heteronuclear single quantum coherence (A) and heteronuclear multiple quantum coherence (B) which are often referred to as HSQC and HMQC schemes, respectively. The time period τ is set to $(4J)^{-1}$ or slightly shorter to compensate for relaxation losses. These sequences can easily be described using the product operator formalism. Table 13 presents the resulting operators at the end of the sequence for a three-spin system with two scalar coupled spins I and H of the same species and one spin S of a different species scalar coupled only to I spins.

Table 13
Coherence transfer by HSQC and HMQC schemes as shown in Fig. 24

Fig. 24	Initial state	Resulting product operators describing the transformation properties of the sequence[a]
A	I_z	$I_x \cos(\Omega t_1) \cos^2(2\pi J_{II}\tau) \sin^2(2\pi J\tau) + I_y H_z \cos(\Omega t_1) \sin(4\pi J_{II}\tau) \sin^2(2\pi J\tau)$
B	I_z	$I_y \cos(\pi J_{II}(t_1 + 4\tau))(\cos^2(2\pi J\tau) - \cos(\Omega t_1) \sin^2(2\pi J\tau))$ $+ 2I_x H_z \sin(\pi J_{II}(t_1 + 4\tau))(\cos(\Omega t_1) \sin^2(2\pi J\tau) - \cos^2(2\pi J\tau))$

[a] A three-spin system is considered with two spins, I and H, belonging to the same nuclear species and one spin S of a different species. Spin S is scalar coupled only to I and not to H. The heteronuclear coupling constant is denoted J and the homonuclear coupling between I and H, J_{II}. Only operators that lead to detectable in-phase magnetization with respect to spin S are shown. Signals originating from polarizations of H and S spins at the beginning of the sequence are assumed to be cancelled by an appropriate phase cycling scheme.

not be optimal for obtaining good resolution in the indirect dimension because the homonuclear couplings, J_{II}, among the I spins modulate the signal of the S nuclei which broadens the resonance lines in the spectrum. In the HSQC these couplings are not active during the evolution time (Table 13). The description of the two sequences in the product operator formalism given in Table 13 demonstrates that the homonuclear couplings J_{II} reduces the signal slightly for the HSQC, whereas a phase shift $4\pi J_{II}\tau$ is introduced into the indirect dimension of the HMQC experiment which cannot be corrected since J_{II} varies randomly from resonance to resonance. In addition, the homonuclear coupling among the I spins leads to a contribution of homonuclear anti-phase dispersive signals. These signals do not usually disturb spectra of proteins due to the inherently broad linewidths.

In both schemes shown in Fig. 24 the S spins evolve not only due to the chemical shift but also due to their homonuclear couplings J_{SS} introducing line splittings in well-resolved spectra. Often only the heteronuclear correlations between the I and S spins are of interest, whereas the resolved couplings are undesired. This requires a scheme during which the spins evolve due to chemical shifts but not due to homonuclear couplings. Fig. 25 presents a sequence that fulfils these boundary conditions [211,212]. The segment has a fixed duration $2T$. The evolution of the S spins due to homo- and heteronuclear scalar couplings does not depend on the chemical shift evolution time t which can be changed in the range from 0 to $2T$. In this constant-time (CT) evolution segment (Fig. 25) the modulation of the signal due to its chemical shift is obtained by moving the two 180° pulses as indicated in Fig. 25. The two 180° pulses have a fixed separation of length T and the delay t is incremented according to the frequency range desired in the spectrum (Table 3). If the homonuclear couplings J_{SS} among the S spins have a narrow range of values the time period $2T$ can be set to a multiple of $1/J_{SS}$ to obtain a homonuclear decoupled spectrum of the S spins. For example, the aliphatic carbon spin systems in fully ^{13}C-labelled proteins have coupling constants in a narrow range around 35 Hz except for the coupling to the carbonyl carbons which can easily be decoupled by conventional decoupling (Section 4.3). Setting $2T$ to $1/J_{SS} = 28$ ms for carbons will result in different signs for resonances of carbons coupled to odd and even numbers of carbons. On the other hand, with $2T = 2/J_{SS}$ (56 ms) all resonances will have the same sign. Transverse relaxation during $2T$ limits the general applicability of CT evolution sequences because in large proteins relaxation may severely reduce the signal intensity. If CT evolution cannot be used, the maximal evolution time for heteronuclei with homonuclear couplings should not exceed $(4J_{SS})^{-1}$ which for aliphatic carbons corresponds to about 8 ms. This short maximal evolution time avoids the measurement of data with inherently low sensitivity caused by the cosine modulation of the signal due to the J_{SS} coupling. In addition, linewidths cannot be significantly

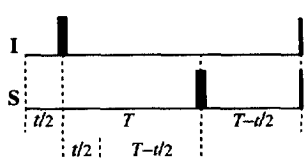

Fig. 25. Constant time (CT) chemical shift evolution period with a fixed duration $2T$. The separation of the two 180° RF pulses stays constant at T. For all values of T the evolution of the S spins due to scalar coupling to the I spins is refocused. If $2T$ is set to a multiple of $1/J_{SS}$, where J_{SS} is the coupling between the S spins, homonuclear decoupling of the S spins can be obtained. The maximal evolution time for the S spins due to their chemical shift is $2T$.

improved with longer evolution times since the unresolved homonuclear couplings can only be resolved using very long evolution times.

4.5.2. Concatenating basic segments

Generally, basic segments are implemented into pulse sequences by applying them consecutively as in the HSQC or HMQC experiments above, or in a more complex example in Fig. 10. Although this results in a functional pulse sequence, in some situations adjacent segments can be combined into a new segment. Such a concatenation may reduce the overall duration and/or the number of RF pulses and hence usually improves the sensitivity of the experiment. When evolution segments containing 180° RF pulses (Figs. 11 and 12) occur consecutively, such an optimization can often be performed [213]. Fig. 26 illustrates the procedure with some very frequently applied optimizations.

One combination of basic segments that frequently occurs in heteronuclear experiments consists of an evolution due to the chemical shift followed by an evolution due to J coupling to prepare a subsequent coherence transfer step (Fig. 26(A)). These two segments can be combined by reducing the number of 180° RF pulses from three to two (Fig. 26(A′)). An algorithm that supports the optimization of pulse sequences has been developed [213] which is based on the properties of 180° RF pulses. A 180° pulse reverses evolution due to chemical shift and it also reverses evolution due to J coupling when applied only to one of two coupled spins. Thus the effective time that the spins evolve can be calculated by summing together time periods before and after a 180° pulse with different signs. Following this system the effective time period t_δ during which the spins I in Fig. 26(A′) evolve due to chemical shift can be calculated as indicated in Eq. (52). The duration of t_δ must be equal to the chemical shift evolution time t in the scheme in Fig. 26(A). Similarly, the effective evolution time t_J of the I spins due to J coupling to the S spins can be calculated (Eq. (53)). Comparing with

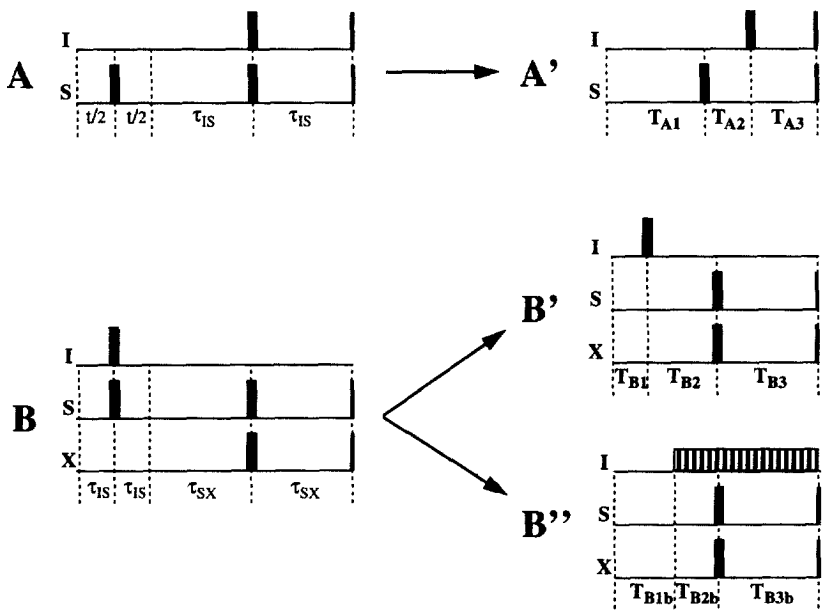

Fig. 26. Optimization of consecutively applied basic segments. (A) Time periods during which the spin states evolve due to chemical shift and due to scalar coupling are combined in (A′) by reducing the number of 180° RF pulses. Depending on the boundary conditions used to calculate the time periods T_{A1}, T_{A2} and T_{A3} in (A′) (see text) the duration of the segment to obtain the same spin state can be reduced compared to the original sequence. (B) Two consecutive time periods with effective evolution due to scalar coupling are combined in (B′) and (B″) by reducing the number of 180° RF pulses as well as the duration (see text). Two alternative schemes are presented: (B′) using 180° pulses for decoupling of the S spins from the I spins and (B″) using a multipulse decoupling scheme.

the original segments in Fig. 26(A), the duration of t_J must be set equal to $2\tau_{IS}$.

$$t_\delta = T_{A1} + T_{A2} - T_{A3} = t \tag{52}$$

$$t_J = T_{A1} - T_{A2} + T_{A3} = 2\tau_{IS} \tag{53}$$

Although Eqs. (52) and (53) have an infinite number of solutions, only solutions with minimal overall duration are of interest. One obvious solution is $T_{A1} = t/2 + \tau_{IS}$, $T_{A2} = t/2$ and $T_{A3} = \tau_{IS}$. Applying the pulse sequence in Fig. 26(A′) with theses values for the delays achieves the same result as the original sequence in Fig. 26(A) which uses one more 180° pulse.

In the solution just described the time t_J required for the INEPT transfer is not used for chemical shift evolution. A different solution of Eqs. (52) and (53) allows the use of the constant period $2\tau_{IS}$ for chemical shift evolution [214,215] in multidimensional experiments. This scheme is often referred to as a semi-constant-time evolution period. The initial condition stays the same but now all three time periods are allowed to vary and T_{A3} should vanish for the last or Nth increment of the evolution time. The following values describe a favourite solution, $T_{A1} = t/2 + \tau_{IS}$, $T_{A2} = t/2 - \tau_{IS}(k-1)/(N-1)$ and $T_{A3} = \tau_{IS}(N-k)/(N-1)$ where the integer k runs from 1 to N. This procedure reduces both the number of 180° pulses and the overall duration of the sequence.

There is yet another solution of Eqs. (52) and (53) which finds frequent applications in pulse sequences used for heteronuclear multidimensional experiments. Setting the overall duration of the segment in Fig. 26(A′) to $2\tau_{IS}$ results in a scheme that allows chemical shift evolution which does not require any more time than required for evolution due to J coupling. Obviously, in this case the chemical shift evolution time t is limited to a maximal value of $2\tau_{IS}$ or an odd multiple thereof. This segment is usually referred to as a constant time evolution period. Solving Eqs. (52) and (53) with these boundary conditions the time periods in the sequence in Fig. 26(A′) become $T_{A1} = t/2 + \tau_{IS}$, $T_{A2} = 0$ and $T_{A3} = \tau_{IS} - t/2$.

The successive application of polarization transfer steps is another very common combination of basic segments which can be optimized. In heteronuclear triple resonance experiments three nuclear species I, S and X are correlated. For example, transverse S spin magnetization in anti-phase to I spins is refocused and subsequently allowed to evolve into an anti-phase state with X spins (Fig. 26(B)). Optimization is achieved by eliminating one 180° RF pulse to shorten the sequence. Again, relations can be formulated [213] for the effective periods of evolution due to chemical shift, t_δ, the coupling between I and S, t_{IS}, and the coupling between S and X, t_{SX}. In the scheme in Fig. 26(B) only the transverse magnetization of S spins is of interest. This magnetization should not exhibit evolution due to chemical shift as is formulated in Eq. (54). The required evolution due to J couplings results in Eqs. (55) and (56):

$$t_\delta = T_{B1} + T_{B2} - T_{B3} = 0 \tag{54}$$

$$t_{IS} = T_{B1} - T_{B2} + T_{B3} = 2\tau_{IS} \tag{55}$$

$$t_{SX} = T_{B1} + T_{B2} + T_{B3} = 2\tau_{SX} \tag{56}$$

When the scalar coupling J_{IS} between the I and S spins is larger than J_{SX} between the S and X spins a solution for Eqs. (54)–(56) is obtained with $T_{B1} = \tau_{IS}$, $T_{B2} = \tau_{SX} - \tau_{IS}$ and $T_{B3} = \tau_{SX}$. An alternative scheme (Fig. 26(B″)) uses a multipulse decoupling sequence instead of a 180° pulse to decouple the I and S spins during the additional time period the S and X spins require for an optimal coherence transfer. With $J_{IS} > 2J_{SX}$ one obvious solution is given by $T_{B1b} = 2\tau_{IS}$, $T_{B2b} = \tau_{SX} - 2\tau_{IS}$ and $T_{B3b} = \tau_{SX}$.

4.5.3. Sensitivity enhancement

Multidimensional NMR experiments contain, among their basic segments, several chemical shift evolution periods bounded by 90° RF pulses. The magnetization M entering the evolution period will be modulated by evolution due to chemical shift resulting in two orthogonal components, from which a subsequent 90° pulse will retain only one which finally contributes to the measured signal. Therefore, increasing the dimensionality of an NMR experiment will generally decrease the sensitivity by $\sqrt{2}$. Further sensitivity losses occur when magnetic field gradients are used to select the magnetization of interest in the evolution time. Gradients select only one coherence level, either positive or negative depending on the relative sign of the gradients (Eq. (30)). However, phase sensitive spectra require both levels to be retained in the coherence pathway. Hence, when

phase sensitive data are measured with gradient selection, two scans must be collected for each increment just as in an experiment using phase cycling. However, gradient selection discards half of the signal, resulting in an additional sensitivity loss of $\sqrt{2}$.

For certain classes of experiments pulse schemes have been developed that overcome the limitations described above and offer improvements in sensitivity. The sensitivity gains are realized by retaining both the cosine- and the sine-modulated components after the evolution time and transforming them into observable magnetization. A maximal sensitivity enhancement of $\sqrt{2}$ can be achieved for each indirect dimension using phase cycling for the coherence pathway selection and a maximal sensitivity enhancement of two using PFGs. The sensitivity enhancement schemes work best for heteronuclear two-spin systems such as ^{15}NH and ^{13}CH moieties in isotope-labelled proteins [177,216]. In cases where XH_2 and XH_3 moieties must also be detected, for example in proton-carbon correlation spectroscopy, the sensitivity enhancement is reduced [217]. In the following the application of a non-gradient, sensitivity-enhanced INEPT segment to a two-spin system is discussed, followed by a similar analysis of a sensitivity-enhanced INEPT segment using gradient selection.

The sensitivity-enhanced sequences rely on a temporary "storage" of magnetization in a heteronuclear double quantum state. The pulse sequence segments in Fig. 27 are longer than the simple basic segments (Figs. 17(A) and 24(A)) and require more RF pulses. None the less, a sensitivity enhancement can usually be obtained for small and medium sized proteins up to 25 kDa. Using the product operator formalism, the principle of the enhancement sequences can easily be analysed. With the sequence shown in Fig. 27(A) the S magnetization in anti-phase to I spins present after a chemical shift evolution time t_e is transformed into detectable I magnetization [177] as follows:

$$2I_zS_y\cos(\Omega t_e) - 2I_zS_x\sin(\Omega t_e) \rightarrow \mp I_y\cos(\Omega t_e) - I_x\sin(\Omega t_e) \quad (57)$$

where the phases of the first 90° pulse on S spins are x and −x. The two scans corresponding to these two phases must be stored in separate memory locations. Addition of the two scans produces the x component, $-2I_x\sin(\Omega t_e)$, and subtraction the y component, $2I_y\cos(\Omega t_e)$. After a 90° phase correction on one of the data sets the two data sets can be added resulting in a sensitivity enhancement of $\sqrt{2}$ since the conventional scheme only retains one of the two components. Gradients in the pulse sequence of Fig. 27(A) are only used to suppress potential artefacts from pulse imperfections.

Fig. 27(B) presents the sequence used to obtain a sensitivity enhancement of a factor of two in gradient-selected multidimensional experiments [216]. For the gradient selection the strength of the gradient G_1 with duration τ_1 applied to transverse S spin magnetization and the strength of the gradient G_2 with duration τ_2 applied to transverse I magnetization must fulfil the relation $G_1 = \pm \gamma_I G_2\tau_2/(\gamma_S\tau_1)$ (Fig. 23(B)). The additional small gradients in the sequence suppress possible artefacts. Just as with the non-gradient

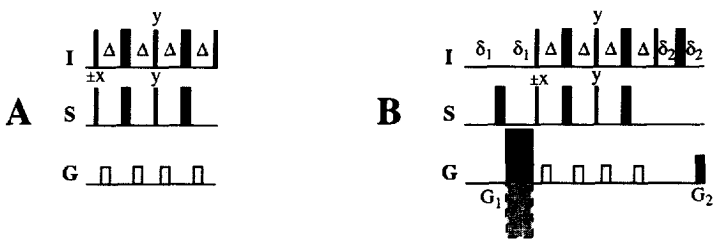

Fig. 27. Sensitivity enhancement schemes. All gradients except for G_1 and G_2 are applied to destroy potential artefacts caused by the 180° RF pulses. The delay Δ is set to $(4J)^{-1}$. (A) Both orthogonal magnetization components present after evolution of the S spins due to chemical shift are recovered. The coherence pathway is selected using phase cycling. (B) Scheme with gradient selection of the desired magnetization resulting in the same sensitivity as in (A). Concomitant with the phase change of the first 90° pulse on the S spins, the sign of the gradient G_1 is changed. The gradients G_1 and G_2 must fulfil the equation: $G_1 = \pm \gamma_I G_2\tau_2/(\gamma_S\tau_1)$ where G_1 and G_2 are the respective gradient strengths and τ_1 and τ_2 the respective durations. The delays δ_1 and δ_2 are set to the duration of the gradient applied during these periods plus the necessary recovery delay.

version, this experiment requires, together with a sign change of gradient G_1, phase cycling of the first 90° pulse on S spins using the phases x and −x in alternating scans which are stored in separate memory locations. The sequence transforms anti-phase S spin magnetization present after an evolution time into detectable I spin magnetization according to

$$2I_zS_y \cos(\Omega t_e) - 2I_zS_x \sin(\Omega t_e) \rightarrow \pm I_y \cos(\Omega t_e) - I_x \sin(\Omega t_e) \quad (58)$$

Phase x for the first 90° pulse on the S spins leads to the plus sign for I_y and phase − x with simultaneous inversion of the gradient G_1 to the minus sign. Phase sensitive data is obtained by phase correcting one of the data sets by 90° followed by addition and subtraction of the two separately stored experiments. This experiment has a sensitivity enhancement of factor two compared to the conventional gradient-selected experiment. In other words, the sensitivity-enhanced gradient-selected experiments for two-spin systems are as sensitive as their sensitivity-enhanced non-gradient counterparts.

4.6. Artefact reduction

Experiments can suffer from two categories of artefacts: those introduced by the particular method applied and those introduced by technical limitations of the NMR spectrometer. Examples of the first category are the signal loss when gradient selection is used, the interference effects due to insufficient relaxation delays between measurements and signal losses or artefacts due to the non-ideal excitation profiles of perfectly homogeneous RF pulses with limited power. Examples of the second category are artefacts introduced by the RF inhomogeneity of the pulses, instrumental instabilities, and artefacts introduced due to the huge dynamic range of proton resonances in a sample with a protein dissolved in H_2O. Numerous artefacts and remedies for their suppression have been discussed in the preceding sections. Most techniques which suppress artefacts rely on proper phase cycling of the RF pulses and the suitable application of magnetic field gradients. Effective use of these tools has led to a very good average quality for multidimensional NMR spectra of proteins in aqueous solution. In this section a few additional frequently used procedures are presented. However, in general, the basis for minimal artefacts remains a well-maintained, state-of-the-art NMR spectrometer in a stable environment [138].

The additional pulse sequence elements shown in Fig. 28 destroy selected magnetization components and may help to reduce artefacts. The elements in Fig. 28(A) and 28(B) make use of the inhomogeneity of the RF field to destroy unwanted magnetization components during a long spin-lock purge pulse [77]. Typically, a 2 ms spin-lock pulse with a strength of about 15 kHz will completely

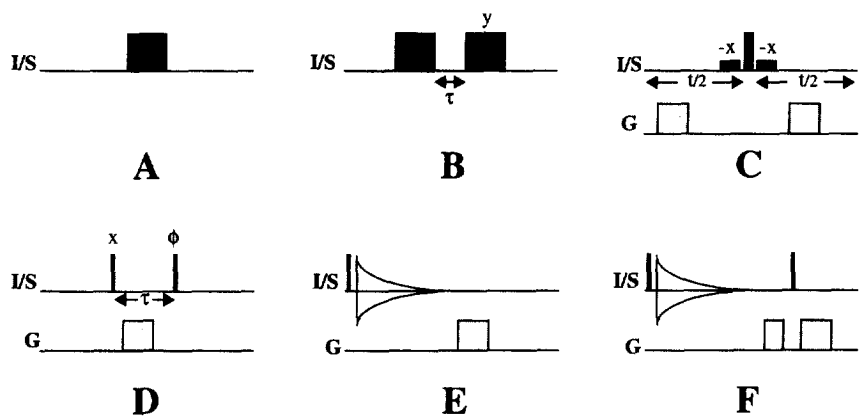

Fig. 28. Schemes used for the suppression of artefacts. (A) and (B) present spin-lock pulse elements which destroy magnetization due to the RF inhomogeneity of the applied RF field. (C) is a sequence that destroys resonances in a small spectral range, for example the water resonance. (D) shows a z filter that allows purging of undesired magnetization components. (E) and (F) depict schemes that destroy magnetization after the acquisition and eliminate interference effects between successive scans.

destroy the water magnetization of an H_2O solution. During the spin-lock pulse all magnetization components not lying along the spin-lock axis are dephased and no longer produce a net signal. However, exactly as in the case of static pulsed magnetic field gradients (Section 4.4), zero quantum states present during the spin-lock pulse cannot be destroyed. The spin-lock field defines a magnetic field axis in the rotating frame around which the magnetization components precess during the pulse. Homonuclear anti-phase I_yS_z magnetization in the laboratory frame will represent a superposition of zero and double quantum states in the rotating frame of the spin-lock field applied along the x axis. Consequently, half of the I_yS_z anti-phase magnetization will survive a spin-lock purge pulse with phase x. In Fig. 28(B) a second spin-lock pulse with phase y is included after a delay τ. This scheme destroys magnetization with arbitrary phase, such as the solvent resonance, which is on-resonance with the frequency of the two spin-lock pulses. Magnetization spin-locked by the first pulse precesses dependent on the offset Δ from the carrier frequency. The components which have rotated to align along the y axis survive the second spin-lock pulse. The intensities of all the resonances in the spectrum will be modulated by $\sin(2\pi\tau\Delta)$ with Δ being the frequency offset of a particular resonance from the carrier frequency. The period τ can be adjusted to have maximum excitation in the desired spectral range. In practical applications the length and power of the spin-lock purge pulses are limited by the specifications of the probe. If spin-lock purge pulses and PFGs are applied in a single pulse sequence, interference effects may occur [218] which degrade the performance.

A further solvent suppression scheme can be obtained by a combination of PFGs and selective excitation as shown in Fig. 28(C). The 180° pulse refocuses all magnetization with the exception of a small spectral region which is selectively excited by the two flanking 90° low-power pulses producing an effective 0° pulse in this spectral region. Only magnetization that experienced an effective 180° pulse refocuses due to the second gradient (Fig. 22(C)) whereas the signals in the narrow spectral region are destroyed. The duration t is kept as short as possible and typically does not exceed a few milliseconds. This sequence, known under the acronym WATERGATE [87], gives very efficient water suppression but at the same time strongly attenuates signals close to the water resonance. This limitation does not affect ^{15}N-relayed heteronuclear experiments where only amide protons are detected during acquisition. In such experiments the sequence can be integrated into the final INEPT step without lengthening the experimental scheme.

Fig. 28(D) displays a purging scheme known as a z filter [219]. The magnetization of interest is taken through a z state so that the magnetization components remaining in the transverse plane can be destroyed by a PFG. Alternatively, the phase of the second pulse and the receiver can be incremented by 90° in four successive scans. Of course, zero quantum coherence present during τ cannot be removed by this element. However, in analogy with the NOESY sequence the time τ can be incremented or randomized between successive scans to suppress zero quantum states based on their precession during τ. When relaxation permits, an improvement of z filters and trim pulses can be obtained by spin-locking with inhomogeneous B_0 or B_1 fields, a technique which can also achieve dephasing of zero quantum states [220].

The repetition rate of pulse sequences in a typical NMR experiment must be a compromise between reaching the Boltzmann equilibrium at the start of the sequence and an efficient signal acquisition requiring relatively short interscan delays. Typically, interscan delays are between 1 and 1.5 s which is often too short to reach thermal equilibrium. The spectra are measured in a steady state mode which can lead to interference effects in successive scans resulting in artefacts in the final spectrum. For example, in COSY spectra small resonances on a line with double the slope of the normal diagonal can sometimes be observed. These artefacts originate from resonances which have not fully relaxed between two scans and hence were frequency labelled a second time obtaining double the frequency in the indirect dimension. With the scheme presented in Fig. 28(E) all transverse magnetization can be destroyed after the acquisition. This is often not of prime interest for protein resonances which usually have a sufficiently fast transverse relaxation not to cause interference; however, the procedure may be useful for small molecules and peptides. In cases where interference effects are transmitted via z states, not only resonances of small

molecules but also protein resonances may contribute. Fig. 28(F) shows a sequence based on magnetic field gradients that destroys all magnetization after the acquisition and guarantees identical starting conditions for all scans during an experiment. Alternatively, this sequence can be replaced by the element shown in Fig. 28(B) with τ set to zero.

5. Hydration studies

This section serves two purposes. On the one hand, it provides examples of the general concepts introduced in the preceding sections and, on the other hand, it presents additional methods and technical problems which are best discussed in the context of NMR hydration studies. Representative examples of experiments are used to discuss the specific technical problems encountered when using NMR for studies of hydration.

5.1. Hydration

Interest in the hydration of proteins arises from a desire to understand the influence of water on the structural, functional and dynamic properties of biological macromolecules such as proteins. Despite their importance, the details of water–protein interactions are not well understood. The compact folding of the polypeptide chains in globular proteins usually excludes the solvent from the molecular core leading to a hydration shell constituting the interface between solvent and molecules dissolved. Still a small number of water molecules in the interior of proteins are often observed in single crystals [221]. These are typically completely shielded from the bulk solvent, form hydrogen bonds with surrounding polar groups of the polypeptide chain, and are thus an integral part of the protein architecture. Similar data to those for interior water molecules in globular proteins in solution have been reported for the intermolecular interfaces in multimolecular complexes with proteins, for example, in protein–DNA complexes [222,223].

Crystal structures of proteins report the position of some hydration water molecules in the interior as well as on the surface of the molecules. However, diffraction experiments probe only the total fraction of time that a particular hydration site is occupied by a water molecule; they are insensitive to the residence time at that site for a particular water molecule. The lack of experimental methods for determining the dynamic behaviour of water molecules at individual sites at the protein–water interface has prevented a more detailed understanding of hydration. This situation improved in the last few years with the development of NMR techniques, enabling studies of individual hydration sites and providing both structural data at atomic resolution and information on dynamic aspects of biomolecular hydration [224].

5.2. NMR and hydration

The potential of NMR to contribute to the understanding of hydration was realized a long time ago. In 1963 it was observed that proteins dissolved in water increase the relaxation rates of the protons in water. This was shown to be due to an increase in the correlation time of a fraction of the water molecules [225]. The interpretation of the data left two possible explanations. Either a very small number of water molecules stick to the protein for a time much longer than the rotational correlation time τ_R of the protein or hundreds of water molecules have a residence time of the order of τ_R [226]. The controversy could only be resolved when a new class of NMR experiments was developed that uses cross-relaxation (NOE/ROE) between protons in water molecules and protons of the protein [227]. The NOE and ROE are proportional to the inverse sixth power of the distance between the protons and are related to a correlation function describing the stochastic modulation of the interaction (Eqs. (13) and (16)). For studies of hydration, it is important that this correlation function may be governed either by the Brownian rotational tumbling of the hydrated molecule or by interruption of the dipolar coupling through translational diffusion of the interacting spins.

The application of NMR hydration experiments to the bovine pancreatic trypsin inhibitor (BPTI) revealed two distinguishable classes of hydration water molecules in aqueous protein solutions [228–230] (Fig. 29): interior hydration and surface hydration water molecules. Interior hydration waters show cross-relaxation with nearby polypeptide protons which is in the slow motional regime. This motional regime is distinguished by opposite signs of

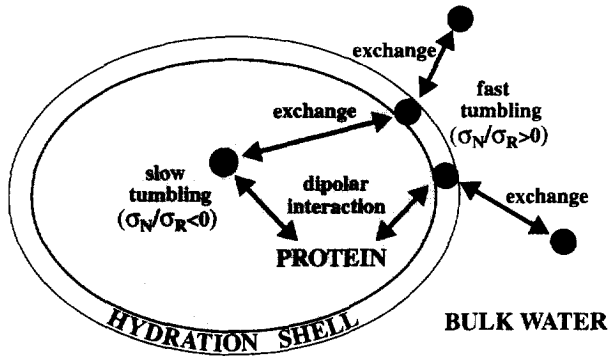

Fig. 29. Schematic representation of a protein shown as a grey ellipse with its hydration shell in an aqueous solution. Black circles represent individual water molecules. Three types of water molecules can be distinguished: bulk water molecules which do not interact with the protein, water molecules in the surface hydration shell which weakly interact with the protein and water molecules in the interior of the molecule. Surface hydration water molecules and interior water molecules show dipolar interactions with the protein and can be distinguished by the different signs of their ratio between the ROE and NOE cross-relaxation rates σ_R and σ_N.

the cross-relaxation rate constants in the laboratory frame of reference, σ_N (Eq. (13)), and in the rotating frame, σ_R (Eq. (16)). Such water molecules have a ratio $\sigma_N/\sigma_R < 0$ indicating lifetimes with respect to exchange with the bulk water greater than 10^{-9} s. Surface hydration waters, however, have a ratio $\sigma_N/\sigma_R > 0$ and much smaller exchange lifetimes in the approximate range of 10^{-11} to 10^{-9} s. Similar data to those for interior hydration of globular proteins in solution have been obtained from NMR studies of the intermolecular interface in complexes between a protein and a DNA duplex [223]. Detailed descriptions of applications of NMR to study hydration can be found in recent reviews [231–233].

Compared to surface hydration waters, interior hydration waters give much more intense NOEs with the protons of the protein because of their longer residence times. However, the residence times are still short enough to observe the same ^{1}H chemical shifts for the interior waters and the bulk water due to exchange averaging [202,229,234]. Not only water molecules exchanging with the hydration shell resonate at the water frequency, but any fast exchanging proton of the protein, especially hydroxyl protons. Consequently, NOEs between these protons and other protons of the protein are indistinguishable from NOEs with water. This degeneracy requires that complete proton assignments are available for the protein and that the solution structure is known in order to distinguish NOEs to hydration water molecules from these rapidly exchanging protons of the protein. In contrast to the hydroxyl protons in the amino acids Ser, Thr and Tyr, the carboxylic acid proton of the Glu and Asp side-chains and the C-terminus do not interfere with hydration measurements [235].

Surface hydration water molecules which show NOEs to protons of a protein with positive σ_N can be detected without the ambiguity introduced by exchanging protons. None the less they suffer from the interference with exchanging protons since they become undetectable when their weak NOE signal overlaps with a strong peak of an interior or exchanging proton. Hence, for proteins with interior water molecules and/or with a considerable number of hydroxyl protons, a complete hydration shell cannot be observed.

The methods developed for hydration measurements can also be used to study the interaction of proteins with other small molecules. The investigation of ligand binding sites [236] and the interaction with denaturants is of special interest in this context [237]. Not only native proteins but also proteins in a denatured state can be studied [238] which do not have a well-defined structure even though structured parts may form transiently [239]. Sequential assignments are a prerequisite for solvent–protein interactions by NMR and can be obtained in the denatured state using isotope-labelled proteins [215,240,241].

5.3. Basic experiments

5.3.1. NOEs between water and protein protons

The first experiment for the observation of individual hydration sites of proteins was a NOESY where the water line was not suppressed before the mixing time but only just before acquisition of the data [227]. With this method water and protein protons will cross-relax during the mixing time when the interproton distance is not larger than about 0.4 nm [227]. Fig. 30 shows a NOESY pulse sequence that would typically be used to study hydration. After the excitation pulse on all protons, a pair of gradients prevents radiation damping of the water resonance during the evolution period [90] (Fig. 22(E)). During the NOE mixing period τ_m (Fig. 15(A)), which is embraced by two 90° pulses, a gradient keeps the water magnetization along the z axis and destroys all single and multiple quantum coherences present during τ_m (Fig. 22(A)). Finally, the water resonance has to be removed to prevent overload of the receiver. The scheme in Fig. 30 utilizes the WATERGATE sequence for this purpose (Fig. 28(C)). The use of RF gradient pulses as originally proposed for water suppression may already transfer magnetization via the TOCSY or ROESY effect for very short durations of the trim pulses [73]. The application of the pulse sequence results in a 2D NOESY spectrum (Fig. 31), where the cross-section through the water resonance parallel to the frequency axis ω_2 contains all interactions between water and protein protons. These interactions include intermolecular NOEs between water and protein protons, intramolecular NOEs between protons of the protein where one nucleus resonates near the water frequency, and exchange

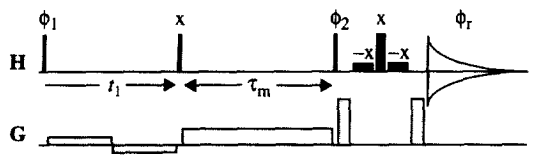

Fig. 30. Pulse sequence for the detection of intermolecular NOEs between water molecules and protein protons using the phases indicated above the pulses and the following phase cycles: $\phi_1 = x, -x$; $\phi_2 = x, x, -x, -x$; $\phi_r = x, -x, -x, x$. During the evolution period t_1 and the mixing time τ_m gradients are applied to prevent radiation damping (Fig. 22(A) and 22(E)). Just before acquisition a WATERGATE sequence (Fig. 28(C)) is used to destroy the water magnetization.

peaks between labile protons and water. The spectrum in Fig. 31 was recorded with the protein BPTI, which contains four interior water molecules [227]. In a horizontal cross-section through the water line, the different resonances cannot be unambiguously assigned and overlap between positive and negative resonances cancels the very small contributions from the rapidly exchanging surface hydration water molecules. NOEs to interior water molecules and exchanging protons of the protein result in positive peaks which dominate the cross-section shown in Fig. 31. Very few interactions with surface hydration water molecules are observable around 0.6 ppm (negative peaks) even though potentially all protein protons on the surface should show an interaction with water. To avoid extensive overlap, the resonances representing the interactions have to be resolved into an additional dimension by some transfer element (Section 4.2). Expanding the NOESY sequence into a 3D experiment results in a 2D cross-section through the water line which contains all resonances of interest. An analogous result can be more efficiently obtained if the water is selectively excited, which results in a 2D spectrum. There are a number of schemes that excite water more or less selectively [73,202,242–248]. All but one sequence [73] suffer from a technical limitation that is quite common in NMR spectra of macromolecules: the water line and some protein resonances usually overlap, which makes the distinction between water–protein interactions and intraprotein NOEs difficult for protons resonating near the water line. Even in uniformly [^{15}N, ^{13}C]-isotope-enriched proteins where intramolecular NOEs can be suppressed using ^{15}N- and ^{13}C-filtering techniques [143], there remains a risk of "breakthrough" of intramolecular NOEs unless the level of enrichment reaches 100% [249].

5.3.2. HYDRA

The HYDRA experiment [73] strictly selects only water–protein interactions even if protein resonances overlap with the water line. These interactions include NOEs as well as chemical exchange. In HYDRA the separation of intermolecular solvent–protein NOEs from intramolecular NOEs is based on the different diffusion constants of water molecules and the biological macromolecules. As a rule, water molecules diffuse about 15 to 25 times faster than proteins in the molecular weight range 10–20 kDa. On this basis,

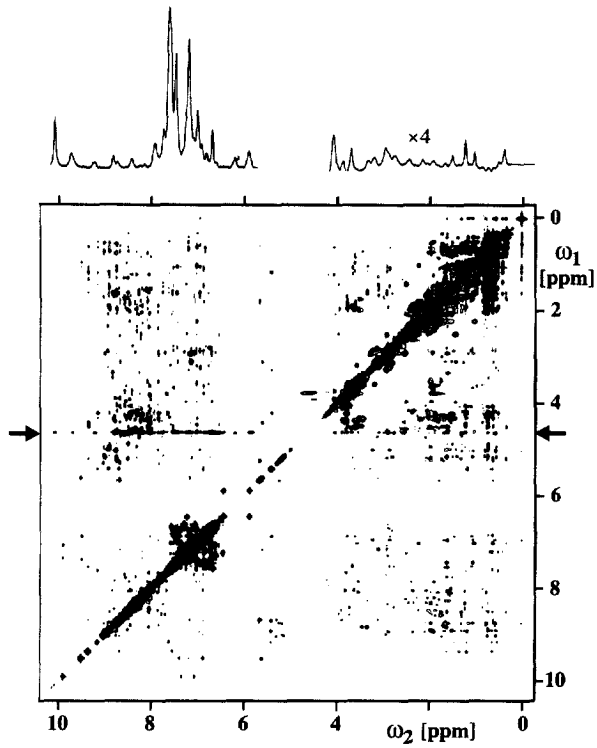

Fig. 31. 2D NOESY spectrum of 10 mM BPTI in a solution of 90% H_2O/10% D_2O at 277 K obtained with the pulse sequence shown in Fig. 30. The horizontal cross-section containing the interactions between protons of the water molecules and protein protons is indicated by arrows and plotted above the 2D spectrum. The spectral range from 0 to 4 ppm in the cross-section is expanded in the vertical direction by a factor of 4 compared to the spectral region from 6 to 10 ppm which is dominated by strong exchange peaks. Exchange peaks and NOEs to the four interior water molecules of BPTI dominate the cross-section and weak NOEs to surface hydration water molecules are only visible for a few methyl groups around 0.6 ppm.

intermolecular water–protein NOEs can be distinguished from intramolecular NOEs with the use of the diffusion segment shown in Fig. 21 which is often referred to as a diffusion filter [203]. A suitably designed experiment, which measures the difference between the signals obtained with strong and weak PFGs in a diffusion filter, selectively records intermolecular protein–water interactions. Fig. 32 shows the pulse sequence for a 1D HYDRA experiment. HYDRA consists of an NOE or ROE mixing period sandwiched between two diffusion filters. The spectrum containing only water–protein interactions is obtained, taking the difference between the data measured in alternating scans using the gradient traces G_I and G_{II}, respectively. The delay Δ and the gradient strengths G_1 and G_2 are chosen such that G_1 destroys most of the water magnetization due to its rapid diffusion (Eq. (52)), whereas G_2 destroys only a small amount of the water magnetization. Subtraction of the two measurements I and II cancels intramolecular Overhauser effects, whereas intermolecular interactions between water and protein protons are retained. For the suppression of the residual water before acquisition, the second diffusion filter is combined with a WATERGATE sequence [87] (Fig. 28(C)). Compared to techniques based on selective excitation, the introduction of diffusion filters reduces the sensitivity [73]. None the less, HYDRA will probably be the method of choice whenever suppression of intramolecular NOEs is important. HYDRA can be used with very short ROE or NOE mixing times. This is in contrast to some schemes using radiation damping [246], where mixing times of less than 60 ms cause severe loss in sensitivity

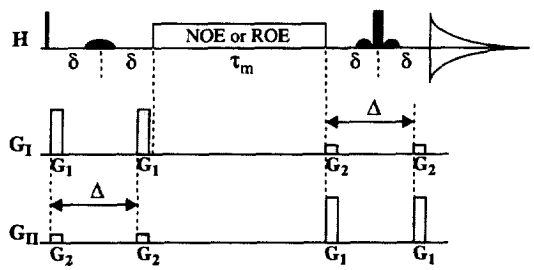

Fig. 32. Schematic experimental scheme for HYDRA difference experiments with diffusion filters for the separation of intermolecular and intramolecular interactions between protein and solvent protons. The curved shapes on the line *H* indicate selective pulses at the water frequency. For the NOE or ROE mixing during τ_m the transfer segment for NOESY or ROESY shown in Fig. 15 must be inserted. The lines G_I and G_{II} indicate the applied magnetic field gradients; the desired spectrum corresponds to the difference between two subsequent experiments recorded with G_I and G_{II}, respectively. The duration of the diffusion filter is 2δ and Δ is the diffusion time. The second diffusion filter immediately before acquisition is combined with a WATERGATE sequence (Fig. 28(C)) to suppress the water resonance. The HYDRA experiments with NOE or ROE mixing have a different phase cycling scheme that provides optimal subtraction of unwanted resonances [73].

and/or in selectivity of the water excitation. Use of very short mixing times may be necessary for studies of short-lived surface hydration, since the very weak NOEs between protein protons and surface hydration water would otherwise be masked by overlap with much stronger NOEs originating from spin diffusion with interior water molecules or labile protein protons (Fig. 31).

As with any difference experiment HYDRA requires special attention to obtain no subtraction artefacts. For this reason the water resonance in the first diffusion filter is refocused by a selective 180° pulse, so that only macromolecular resonances close to the water are preserved and most of the protein magnetization is destroyed before the mixing time (Fig. 22(D)). This improves the quality of the experiment since, for example, methyl resonances can no longer create subtraction artefacts which is a common limitation in difference experiments. When working with macromolecules the duration of the diffusion filter should be kept as short as possible to minimize signal loss due to relaxation. This requires strong gradients that may interfere with the performance of the experiment, since two different gradient schemes G_I and G_{II} are used which induce different transient effects. Shaped gradients with a smooth rise and fall minimize these transient effects and reduce the artefacts in the difference spectrum. One possibility is a modified rectangular shape with the first quarter having a sine-squared and the last quarter a cosine-squared dependence [68,202]. In HYDRA experiments with an NOE mixing period the same amount of magnetization from protein protons has relaxed after τ_m for both gradient sequences G_I and G_{II}. Due to the different strengths of G_1 and G_2 in the second diffusion filter, this would result in a non-zero difference spectrum. Since the NOE depends only on population differences, the water magnetization can be flipped into the positive and negative z direction at the start of the mixing time, which allows subtraction of the residual difference caused by the relaxed protein magnetization. For the experiments with an ROE mixing time there is no relaxed magnetization after the spin-lock mixing and no compensation is necessary.

To achieve the spectral resolution needed for obtaining individual assignments of water–protein interactions, the basic 1D HYDRA scheme (Fig. 32) can be combined with any transfer element (Section 4.2) to generate a higher-dimensional experiment. Fig. 33 compares a 2D [^{1}H, ^{1}H]-TOCSY-relayed HYDRA spectrum [73] with a 2D [^{1}H, ^{1}H]-TOCSY-relayed NOE experiment which uses radiation damping for the water selection [250]. The diagonal in these 2D spectra comprises peaks which originate from NOEs or chemical exchange between water and protein protons. The TOCSY segment transfers magnetization from the diagonal peaks to scalar coupled protons resulting in a cross-peak at the same ω_1 frequency as the diagonal peak. The spectra were recorded with a solution of the protein BPTI. The positive cross-peaks correspond to signals that were previously assigned either to NOEs with the four interior water molecules in BPTI, to exchange peaks or to NOEs with rapidly exchanging side-chain hydroxyl protons of the protein [251]. The spectral region shown does not contain negative cross-peaks which would indicate NOEs between water protons and solvent accessible protons on the protein surface. Either their signal intensity is too small to be detected or they overlap with strong positive peaks. In Fig. 33(A) the spectrum collected using radiation damping to selectively excite the water contains a

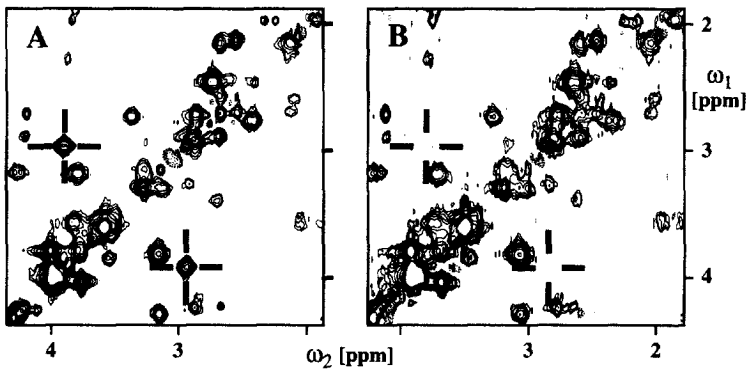

Fig. 33. Contour plots of expansions of 2D TOCSY-relayed NOE difference spectra measured with a 20 mM solution of BPTI at a temperature of 277 K. The solvent was 90% H_2O/10% D_2O at pH 3.5. The NOE and the TOCSY mixing times were 60 and 27 ms, respectively. The crosses mark the position of the TOCSY-relayed intramolecular NOE between Cys 38 H^{α} and Cys 38H^{β}. (A) [^{1}H,^{1}H]-TOCSY-relayed NOE difference spectrum using radiation damping for the selection of the water resonance. (B) [^{1}H,^{1}H]-TOCSY-relayed HYDRA experiment. The intramolecular NOE Cys 38 H^{α}/Cys 38 H^{β} is suppressed and the remaining TOCSY-relay peaks indicate intermolecular NOEs to interior water molecules or rapidly exchanging protons of the protein.

TOCSY-relayed NOE between Cys 38 H^{β} and Cys 38 H^{α} (marked by a cross), because the chemical shift of the Cys 38 H^{α} resonance coincides with that of the solvent water resonance. The HYDRA spectrum of Fig. 33(B) contains exclusively interactions with water protons, as is demonstrated by the absence of the cross-peak between Cys 38 H^{β} and Cys 38 H^{α}.

5.3.3. Measurement of exchange rates using diffusion filter experiments

Observation of hydration water molecules located in the core of globular proteins by NMR spectroscopy showed that these have ^{1}H chemical shifts identical with that of the bulk water, implicating exchange averaging of the shifts in the two environments [229]. The exchange rates for the interior hydration sites are of interest since these can be directly related to the frequency of internal motions of the protein. However, measurements of fast exchange rates in the expected range of 10^3 to 10^6 s^{-1} are rather difficult. Two techniques have been proposed to determine the exchange rates or residence times of interior water molecules. One method uses the dependence of ^{17}O and ^{2}H relaxation in water molecules on the main magnetic field and allows determination of residence times τ_{res} in the range from 4 to 200 μs [226,252,253]. The other method is based on diffusion-weighted NOESY experiments [202,242] and current technology allows the measurement of minimal values for τ_{res} of 1 ms. Although the following discussion of the latter method concentrates on the measurement of residence times of interior water molecules, the same technique can be used for the determination of fast exchange rates, for example of rapidly exchanging hydroxyl or amide protons with the bulk water.

In a suitably designed NOESY experiment with a diffusion filter, the decaying signal amplitudes of protein resonances will record via their NOEs the diffusion properties of the otherwise unobservable interior water molecules. The average translational diffusion constant for water molecules transiently trapped inside macromolecules is smaller than for bulk water. This difference reflects the lifetimes of the interior water molecules. Fig. 34 shows a pulse sequence used for the measurement of lifetimes of interior water molecules [202]. The addition of pulsed magnetic field gradients, which are applied before and after the mixing time, τ_m, introduces diffusion rate-dependent signal intensities of the NOEs between protons in water molecules and protein protons. Self-compensating "PFG sandwiches" [68] are used instead of single gradient pulses to reduce unwanted transient distortions. This allows much shorter recovery times than would be possible with a single magnetic field gradient. During the evolution time t_1 very low amplitude PFGs are applied which defocus and refocus the desired magnetization while preventing radiation damping [90] (Fig. 22(E)). Another low-amplitude PFG during the mixing time eliminates coherences present after the second 90° RF pulse.

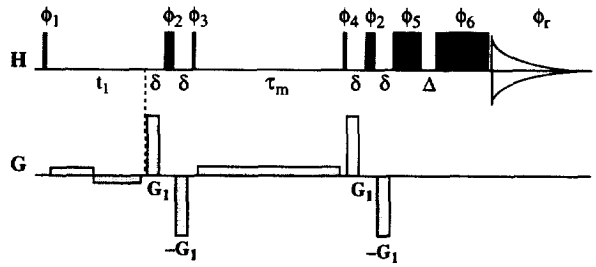

Fig. 34. Experimental scheme for a 2D [^{1}H,^{1}H]-NOESY used to measure exchange rates based on the different translational diffusion of water and macromolecules. On the horizontal line labelled H, RF pulses applied at the resonance frequency of protons are indicated and on the line G the position of PFGs is shown. The evolution time is t_1, τ_m the NOESY mixing period and δ a short delay of 1 ms or less for the application of the very strong magnetic field gradients G_1. A weak gradient is used to destroy unwanted magnetization during τ_m. Immediately before acquisition, two spin-lock purge pulses separated by the duration Δ are applied to suppress the water resonance (Fig. 28(B)). The phase cycle is as follows: $\phi_1 = 8(x), 8(-x)$; $\phi_2 = 2\{2x, 2y, 2(-x), 2(-y)\}$; $\phi_3 = 8\{x, (-x)\}$; $\phi_4 = 4\{2(x), 2(-x)\}$; $\phi_5 = 16(y)$; $\phi_6 = 2\{4x, 4(-x)\}$; with the receiver cycle $\phi_r = 2\{x, 2(-x), x\}, 2\{-x, 2x, -x\}$. Quadrature detection in t_1 is achieved by altering the phase ϕ_1 according to States-TPPI (Table 3).

Water suppression is achieved just prior to acquisition by a pair of orthogonal trim pulses separated by a short delay Δ [77,250] (Fig. 28(B)). In addition, these trim pulses select magnetization components along the x axis only, which results in a phase-sensitive spectrum [208]. For the determination of the exchange rates, a series of spectra with increasing gradient strength G_1 is measured. The shortest exchange lifetime that can be determined depends on the largest available gradient strength [202]. Measuring a lifetime of about 1 ms requires a gradient strength of $2\,T\,m^{-1}$ which is technically very demanding. The goal to measure even shorter lifetimes can only be reached by the use of shorter and stronger gradients with extremely brief gradient recovery times. With such an improved gradient hardware, measurements of residence times of interior water molecules in the submillisecond range will become possible.

The experimental scheme in Fig. 34 was used to measure the residence time of interior water molecules in BPTI [202] which contains four interior water molecules [254,227]. A maximal lifetime of 10^{-3} s could be established for both the cluster of three water molecules, which is partly surface accessible, and a completely buried single water molecule. The limit of $10^3\,s^{-1}$ is set by the maximum available gradient strength of $1.8\,T\,m^{-1}$. The result indicates that motions with amplitudes of approximately 0.15 nm must occur with a frequency of at least $10^3\,s^{-1}$ even in the core of a small protein.

5.3.4. Relaxation dispersion experiments

In relaxation dispersion experiments the average relaxation properties of nuclei are measured in water molecules in aqueous protein solutions. The deviation of this average relaxation from that in pure water samples describes the influence of hydration water molecules. The relaxation behaviour of hydration water molecules differs from bulk water molecules due to their different mobility which is reflected in different correlation times [225]. For a systematic investigation of molecular motions of hydration water molecules by relaxation rate measurements, it is necessary to investigate the frequency dependence of the relaxation over an extended resonance frequency range. Such measurements with aqueous protein solutions were first performed almost thirty years ago [252] and were referred to as nuclear magnetic relaxation dispersion experiments. Details on the techniques used can be found in a review on dispersion or field cycling experiments [255]. In contrast to NOE-based experiments, the results of relaxation dispersion measurements cannot be directly assigned to individual hydration sites, nor can independent information be derived on the number and lifetimes of hydration waters.

Although nuclear spin relaxation dispersion of the nuclei ^{1}H, ^{2}H and ^{17}O in water molecules has long been recognized to contain dynamic information on the interaction of water with proteins in aqueous solutions, the interpretation of the data has been controversial. Only recently, it was proposed that most of the ^{17}O relaxation dispersion could be due to interior

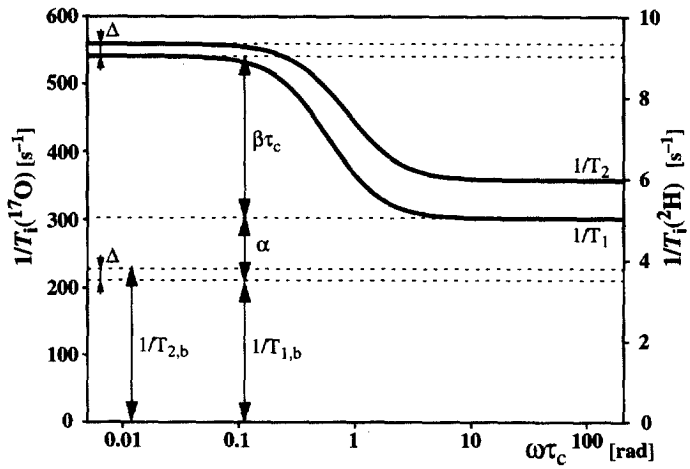

Fig. 35. Typical relaxation dispersion obtained when measuring the field-dependent longitudinal, $1/T_1$, and transverse, $1/T_2$, relaxation rates of ^{17}O and ^{2}H nuclei in water molecules in an aqueous protein solution. The relaxation rates are plotted against the product of the Larmor frequency ω and the rotational correlation time τ_c of the water molecules. The variables α and β describe the two plateaux reached at small and large values of $\omega\tau_c$. The frequency independent relaxation rates of bulk water are indicated by $1/T_{i,b}$ with i being 1 or 2. The difference between the two rates at low frequency is indicated by Δ.

water molecules [256]. For ^{17}O the dominant relaxation process is based on quadrupolar interactions with electric field gradients. Qualitatively, ^{1}H and ^{2}H show a similar relaxation dispersion curve to that of ^{17}O but their relaxation is affected by hydrogen exchange. In addition, the interpretation of ^{1}H relaxation suffers from cross-relaxation between protein and water protons [257,258]. The determination of the contribution of the interior water molecules to the relaxation dispersion of ^{1}H and ^{2}H requires measurements at different pH/pD values, the knowledge of all pK values, all exchange rate constants and, for protons, the relevant cross-relaxation rates [231,253,258,259]. Often these data are not available to the degree of completeness required for a detailed analysis of ^{1}H and ^{2}H relaxation dispersion data. Typically, only a few interior water molecules contribute to the relaxation dispersion and, hence, even a small number of rapidly exchanging protein deuterons or protons can make a contribution to the dispersion comparable to that of all interior water molecules.

Fig. 35 shows representative relaxation dispersion curves of ^{17}O and ^{2}H in water molecules obtained for aqueous protein solutions; relaxation rates are plotted versus $\omega\tau_c$ where ω is the Larmor frequency and τ_c the correlation time of the water molecules. The longitudinal, T_1^{-1}, and the transverse, T_2^{-1}, relaxation rates show a frequency dependence for values of $\omega\tau_c$ in the range from 0.1 to 10 which correspond to resonance frequencies in the range from 1 to 100 MHz. At low frequencies the two relaxation rates are equal if the pH of the solution is either low or high; for a pH close to neutral there is a further dispersion at a frequency of a few kHz [255,260] due to proton exchange between different water molecules. At high frequency the dispersion curves still deviate from the relaxation rate of bulk water. A further dispersion is expected at even higher frequencies containing information on the interaction of water molecules with the surface of the protein. The general functional form of the longitudinal relaxation for Larmor frequencies from about 0.1 to 1000 MHz can be described by Eq. (59) [261].

$$1/T_1(\omega) = 1/T_{1,b} + \alpha + \beta\left[\tfrac{1}{2}J(\omega) + 2J(2\omega)\right] \qquad (59)$$

$T_{1,b}$ is the frequency-independent longitudinal relaxation time of the bulk water. The parameters α and β are illustrated in Fig. 35 and the spectral density function $J(\omega)$ is given in Eq. (8). The parameter Δ in Fig. 35 describes the additional transverse relaxation which is due to a modulation of the only partially averaged scalar coupling between the hydrogen atom and ^{17}O. This scalar relaxation of the first kind depends on the pH and can be neglected for pH values

below 4.5 and above 9.5 [260]. The value for Δ reaches a maximum around neutral pH with typically 0.6 s^{-1} for protons and 250 s^{-1} for ^{17}O. The parameters α and β have been attributed to the water molecules interacting weakly and those interacting strongly with the protein [226]. In this interpretation α describes the surface hydration water molecules and the term β relates to the interior water molecules with a residence time longer than the rotational correlation time τ_R of the molecule. The term α describes average properties of a large number of surface water molecules and is more difficult to analyse than β [226]. Thus the interpretation of relaxation dispersion measurements focuses on β which depends only on a few interior waters and in some cases allows the characterization of individual binding sites for interior water molecules. For ^{17}O relaxation the dominant contribution to β originates from quadrupolar relaxation. This is not the case for ^{1}H and ^{2}H relaxation where exchange contributions may dominate. Measurements with BPTI show a strong pD dependence of the term β [253] for ^{1}H and ^{2}H relaxation.

Eq. (59) has the same dependence on the spectral densities as quadrupolar relaxation [29]. The explicit functional form of the spectral density functions in Eq. (59) depends on the time correlation function of the fluctuations relevant for relaxation and on the shape of the protein. If rotational diffusion of a spherical protein is assumed, the spectral densities given in Eq. (8) are obtained. In this case, a simple relation between the Larmor frequency at which half the maximum relaxation dispersion is reached, $\omega_{1/2}$, and the correlation time τ_c is obtained with $\tau_c = \sqrt{3}\omega_{1/2}$ [252]. Only waters that exchange with a residence time τ_{res} longer than the rotational correlation time of the protein (typically 5 ns or longer) feel the Brownian motion of the macromolecule and contribute to the relaxation dispersion. On the other hand, the average relaxation of the bulk water can only be enhanced by exchange into the protein interior if τ_{res} is shorter than the interior water spin relaxation time which is about 4 μs for ^{17}O and 200 μs for ^{2}H [253]. Thus for a medium-sized protein the maximal residence time measurable by relaxation dispersion experiments is about 2.5 μs for ^{17}O and 75 μs for ^{2}H. Since ^{2}H relaxation is slower than ^{17}O relaxation, a comparison of ^{2}H and ^{17}O relaxation data may reveal interior water molecules which exchange too slowly to influence the ^{17}O relaxation [253].

The experimental implementation of relaxation dispersion measurements is based on simple pulse sequences. The sensitivity of experiments measuring ^{17}O relaxation is greatly improved by using water enriched in ^{17}O isotopes from natural abundance of 0.037% to a level of about 20%. Longitudinal relaxation rates are often measured by the inversion–recovery pulse sequence (180–τ–90) and transverse relaxation rates by the spin–echo experiment (90–τ/2–180–τ/2). Both experiments are measured for an array of different values of τ and at different magnetic field strengths. For a good representation of the relaxation dispersion curve, relaxation for values of $\omega\tau_c$ between 0.05 and 20 should be measured (Fig. 35). Thus, experiments for a medium-sized protein with a correlation time of 10 ns require measuring at different magnetic fields where the resonance frequencies of the respective nucleus vary in the range from 0.8 to 320 MHz. In practice, the accessible range is more restricted due to the small sensitivity at low frequencies and the available magnetic field strength at high frequencies. Missing relaxation rates at high and at low resonance frequencies limit the precision of the determination of the plateaux reached at these two extremes (Fig. 35) and thus the precision of the parameters α and β. The relaxation dispersion of the transverse relaxation time can be used to confirm that the low-frequency plateau is reached in cases where Δ in Fig. 35 is zero.

Very extensive relaxation dispersion data have been collected for BPTI and a BPTI mutant lacking one interior water. The measurements extended over all the three nuclei ^{17}O, ^{2}H and ^{1}H and residence times of the four interior water molecules in native BPTI were determined to lie in the range from 0.01 to 1 μs for three waters and at 170 μs for the fourth water at a temperature of 300 K [262]. Comparison of the relaxation dispersion data for native BPTI and those of the mutant showed that the most deeply buried water molecule has a residence time which is too long to influence the ^{17}O relaxation in the measurement conditions used [234]. The work with BPTI demonstrated that not only the precise 3D structure with the known positions of interior water molecules but also the use of mutants may contribute to an assignment of the different

contributions to relaxation by interior water molecules at individual sites.

The two techniques using relaxation dispersion or diffusion-weighted NOESY spectra [202] (Section 5.3.3) are complementary and make NMR a powerful tool for the investigation of residence times of interior water molecules.

5.4. Artefacts in hydration studies at high magnetic fields

5.4.1. Radiation damping and demagnetizing field effects

The use of high magnetic fields and the improved sensitivity of probes increase the interference of the magnetization of protonated solvents, for example water, with the performance of the experiment. Usually, the magnetic field in an NMR sample is assumed to be constant during an NMR experiment. However, variations of the longitudinal component of the solvent magnetization during a pulse sequences may induce small changes in the magnetic field [94]. During a typical NMR experiment the magnetic field introduced by the solvent magnetization is time-dependent, which causes non-linear behaviour of the system. One consequence of the changing longitudinal solvent magnetization is alteration of the precession frequencies of all nuclei in the sample. Two effects are associated with the water magnetization: radiation damping and the demagnetizing field. In this section consequences of the two effects are presented, using as an example experiments applied to studies of macromolecular hydration.

Radiation damping is a well-known effect in high-resolution solution NMR, which rotates the solvent magnetization back to the external magnetic field direction via the coupling of the magnetization with the resonant circuit of the detection system [263]. This behaviour can be represented as an induced shaped radiofrequency pulse (Fig. 36). The radiation damping field is commonly assumed to affect signals only in a narrow frequency range close to the solvent resonance, but it can influence signals with resonance frequencies differing by several kHz from that of the solvent signal in spite of its small strength of 15–30 Hz. The amplitude, phase and frequency of such signals can be disturbed giving rise to spectral artefacts. In particular, when difference methods are used to obtain the final spectrum, the spectral quality may suffer severely due to such artefacts.

The demagnetizing field in an NMR sample is caused by highly abundant species of the solvent protons in aqueous solutions of proteins. The magnetization of the water protons at high magnetic fields becomes large enough to measurably influence the magnetic field in the sample. As a consequence, the

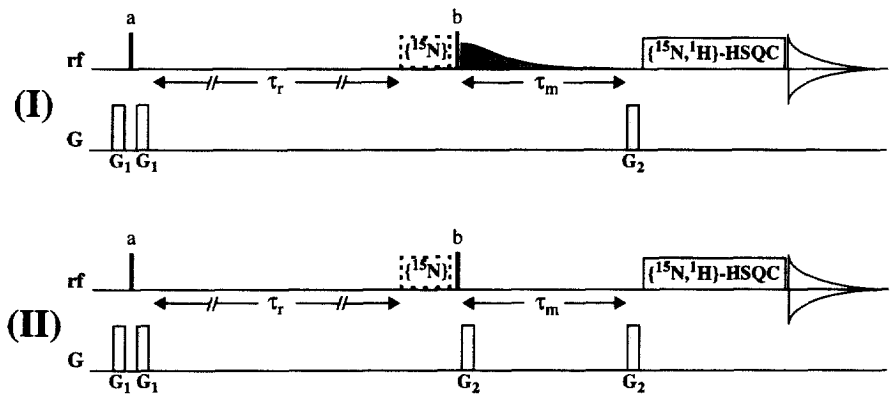

Fig. 36. Schematic pulse sequence for a 2D {^{15}N,^{1}H}-HSQC-relayed NOE difference experiment for protein hydration studies [73,95]. (I) and (II) indicate alternate scans from which the difference spectra are computed. On the line RF the vertical bars labelled a and b stand for 90° proton pulses, the grey shape in scheme (I) indicates the RF induced by the coupling of the solvent magnetization with the receiving circuit (radiation damping), and the box outlined by a broken line labelled {^{15}N} represents a ^{15}N filter used for artefact suppression. The box before acquisition represents the {^{15}N,^{1}H}-HSQC relay step performed with sensitivity enhancement (Fig. 27(B)) and water flip-back [88]. The relaxation delay τ_r is about 2.5 s. On the line G, rectangles stand for gradient pulses. The duration of the gradients is typically 2 ms and they are applied with a strength of about 30 G cm^{-1}.

resonance frequencies of all spins change slightly depending on the state of the solvent magnetization. The strength of the demagnetizing field depends on the sample geometry and vanishes completely in a spherical sample [94]. Unfortunately, this is not a practical alternative to cylindrical NMR tubes and results in reduced sensitivity. The largest chemical shift difference is obtained with the solvent aligned along the positive and the negative z axis and reaches about 2 Hz for protons at 750 MHz in a standard cylindrical sample. The terms "dipolar field" [264] and "bulk susceptibility effect" [94] are alternatively used to denote the same effect. The most direct influence can easily be envisaged in difference experiments in which the water magnetization has a different state in alternate scans which are subtracted from each other.

5.4.2. Minimizing artefacts in hydration measurements

NMR pulse sequences for hydration studies must be designed for the detection of very weak signals in the presence of very intense solvent lines. This has been achieved with the use of selective excitation techniques, the exploitation of radiation damping, isotope filtering and differential diffusion or differential relaxation properties [73,202,242–248]. In many cases, the NMR experiments for studies of macromolecular hydration make use of difference techniques, and are therefore particularly prone to deterioration by artefacts originating from specific NMR properties of the solvent, such as radiation damping and the nuclear demagnetizing field.

The pulse sequence used to demonstrate the influence of radiation damping and the demagnetizing field effect on hydration studies is shown in Fig. 36. This 2D $\{^{15}N,^{1}H\}$-HSQC-relayed NOE difference experiment derives from a scheme described previously [73,95]. The first scan labelled (I) uses radiation damping to rotate the water magnetization back to the equilibrium direction after the 90° pulse labelled b. All remaining transverse magnetization after the NOE mixing time τ_m is dephased by the gradient G_2. In the second scan labelled (II), all transverse magnetization is dephased immediately after the 90° pulse β by an additional gradient G_2 which prevents radiation damping. The difference spectrum obtained from these two scans contains water–protein NOEs, exchange peaks with water, and possibly HN–C^{α}H NOEs when C^{α}H chemical shifts are close to that of water. To prevent artefacts originating from non-steady state conditions, the scheme starts at position a with the sequence G_1–90°(^{1}H)–G_1 to dephase all proton magnetization (Fig. 28(F)).

NOEs between surface hydration water molecules and the protein are very small, making experimental schemes used for such studies especially sensitive to artefacts. Thus the robustness to artefacts must be

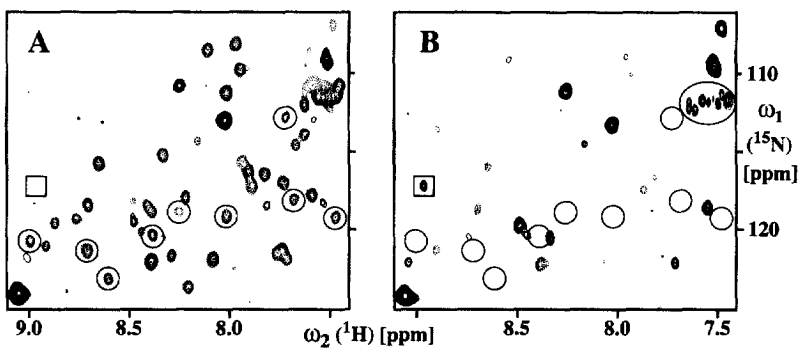

Fig. 37. Contour plots of expanded portions of two 2D $\{^{15}N,^{1}H\}$-HSQC-relayed NOE difference spectra measured with a 5 mM solution of a uniformly ^{15}N-labelled mutant form of the N-terminal DNA-binding domain of the 434 repressor. This mutant with 64 amino acids does not contain any hydroxyl groups. The solvent is 90% H_2O/10% D_2O, the pH 4.8 and the temperature 286 K. The spectrum was obtained with the sequence in Fig. 36, using $\tau_m = 68$ ms. Negative peaks are drawn with dashed lines and positive peaks with solid lines. The circles mark cross-peak positions that correspond to residues with less than 5% solvent accessibility. (A) The rectangle indicates the position of the only backbone amide signal that is missing when compared to a $\{^{15}N,^{1}H\}$-HSQC spectrum recorded with the same conditions. (B) Same as (A), except that a ^{15}N filter was inserted into the pulse sequence ($\{^{15}N\}$ in Fig. 36). The ellipse indicates subtraction artefacts originating from the demagnetizing field effect.

tested for all pulse sequences used in hydration experiments. A first test applies solvent presaturation prior to the sequence and must result in a spectrum which contains no NOEs between solvent protons and protein protons. A further test appropriate for the experiment in Fig. 36 requires perfect subtraction of the signals in the {^{15}N,^{1}H}-HSQC relay step alone. Perfect cancellation for the relay step shows that the stability of the spectrometer is sufficient, the magnetic field gradients used do not create artefacts, the parameters of the field–frequency lock system have been set properly, and that possible small differences in the implementation of the relay step in alternate scans (for example, in the phase of potential water flip-back pulses) do not interfere with the proper performance [95]. These tests are necessary but not sufficient to ensure experiments free of artefacts. A successful presaturation test is not sufficient since presaturation suppresses the dipolar field and the radiation damping effects as well. In a further test a difference spectrum is measured without solvent saturation but with a very short mixing time of only a few milliseconds. In the resulting spectrum only exchange peaks should be detectable. If the solvent magnetization is in different "states" and therefore the demagnetizing field has different strength during evolution periods of two data sets to be subtracted, a difference NMR spectrum may contain "dispersive-like" artefacts [94], which are especially pronounced for narrow signals (Fig. 37(B)). Because phase cycling is a type of subtraction procedure, it alone can already produce such artefacts [265]. The artefacts created by radiation damping can be much more disturbing and are discussed in the next section.

5.4.3. Consequences of radiation damping and demagnetizing field effects

In this section the effects of radiation damping and demagnetizing fields are analysed using the pulse sequence in Fig. 36. Fig. 37 shows spectra obtained with this scheme for a globular protein with 64 residues, a mutant form of the N-terminal domain of the 434-repressor which does not contain any hydroxyl groups [266]. A spectrum obtained without the ^{15}N filter (Fig. 36) contains signals for all amide protons in the protein except one, the position of which is indicated by a square in Fig. 37. Such a result can hardly be expected for a globular protein with a well-defined hydrophobic core that protects part of the amide protons from contacts with the solvent. A standard control 2D spectrum recorded with weak presaturation of the water resonance before the start of the actual pulse sequence contained no peaks. The pulse sequence in Fig. 36 uses radiation damping to select the water resonance. In the scheme, radiation damping is included in the form of an induced shaped RF pulse. Radiation damping during an evolution period can be represented by a shaped pulse which is reminiscent of a truncated hyperbolic secant [263]. Such a shaped pulse can disturb the magnetization of spins that resonate as much as several kHz away from the solvent signal.

A systematic investigation of the phenomenon revealed that negative peaks are obtained for all resonances from an effect of the radiation damping field on the transverse component of the proton magnetization [95]. The negative peaks have intensities of the order of 1% of the equilibrium magnetization of the protein protons before the start of the pulse sequence. The artefacts in the spectrum of Fig. 37(A) can be eliminated by modifying the pulse sequence in such a way that there is no transverse magnetization for ^{15}N-bound protons during the mixing time τ_m. This can be achieved by addition of a ^{15}N filter [143,267], as indicated in Fig. 36 with {^{15}N}. The modified experiment results in the spectrum shown in Fig. 37(B). All cross-peaks observed in the spectrum of Fig. 37(B), except possibly those framed by an ellipse (see below), correspond to amide protons of amino acid residues that are either at the protein surface or have the H^{α} chemical shift close to the water resonance. Interior amide protons (circles in Fig. 37) no longer show false NOEs to water protons. At the position indicated by a square in Fig. 37(B), there is a weak positive exchange peak, which was apparently cancelled in the spectrum of Fig. 37(A) by artefactual negative peak intensity.

The spectrum in Fig. 37(B) still contains "dispersive-like" peaks (framed by an ellipse) that originate from the effect of the demagnetizing field during acquisition. These peaks were masked by other strong artefacts in Fig. 37(A). These "dispersive-like" peaks can be suppressed by omitting the water flip-back pulse in the {^{15}N,^{1}H}-HSQC relay step. Since the water magnetization at the end of the mixing period τ_m in the two experiments to be subtracted is either

aligned along the positive z axis (scheme (I) in Fig. 36) or dephased (scheme (II)), the use of the water flip-back pulse in the $\{^{15}N,^{1}H\}$-HSQC relay step results in slightly different magnetic fields in the sample during acquisition. Similar ''dispersive-like'' patterns in the ^{15}N dimension are absent due to the averaging of the demagnetizing field effect achieved by the proton 180° decoupling pulse in the middle of the ^{15}N evolution period, and the downscaling of the demagnetizing field effect by the smaller gyromagnetic ratio (Eq. (2)).

Other sequences used for hydration studies may produce similar artefacts when implemented on high-field spectrometers. Another sequence for the detection of solvent–macromolecular NOEs that uses selective water flip-back based on radiation damping [246] shows similar artefacts which, however, cannot be suppressed simply with a ^{15}N filter [95]. Similarly, an experimental scheme based on the application of selective pulses on the water resonance [243] contains peaks which do not show up in Fig. 37(B).

In summary, many experiments designed to study hydration may suffer from artificial signals created by magnetic fields originating from the solvent magnetization. The intensity of these signals may be larger than the NOE peaks between hydration water molecules and protein protons. Pulse sequences for hydration measurements are very sensitive to small details in their implementation. Since test experiments with presaturation of the solvent signal eliminate radiation damping and the solvent demagnetizing field along with the artefacts arising from them, more extensive test procedures are required to ensure results which are free of artefacts. This becomes especially important when using a pulse sequence on a spectrometer with a higher field, where radiation damping and demagnetizing field effects are intrinsically stronger.

In general, the test procedures for experiments designed for hydration studies should include a cancellation test for the relay step, a difference test with presaturation of the solvent signal, and an experiment with a very short mixing time (< 5 ms). The demagnetizing field effect can be a source of ''dispersive-like'' subtraction artefacts which can usually be suppressed by proper modification of the pulse sequence to avoid different strength of the demagnetizing field in successive scans. The use of water flip-back pulses [88] seems especially attractive to increase the sensitivity, but in some cases such pulses may have to be sacrificed for the sake of data reliability. In such situations the addition of a relaxation agent to obtain a faster relaxation of the water resonance may be a good compromise for measuring water–protein interactions [246].

6. Conclusions

In the past few years NMR spectroscopy has become an established technique in structural biology and every year a large number of new structures of biological macromolecules are determined at atomic resolution using NMR [268]. In addition to structural information, NMR can deliver data which allow the characterization of dynamic properties of biological macromolecules. However, detailed investigations using the complete 3D structure of proteins are limited to the molecular weight range up to 30 kDa using ^{13}C and ^{15}N labelling and possibly up to 50 kDa using, in addition, deuteration of the molecules. The intention of this presentation was to introduce the basic techniques and conventions used in modern high-resolution NMR applied to the study of biological macromolecules in aqueous solution. For the sake of limiting the review to a realistic length, several topics of interest have been neglected. The discussion of the basic components concentrated on their application in experiments required for the sequential assignment and structure determination and much less on experimental techniques used in investigations of dynamic aspects of molecules in solution. In addition, the discussion of relaxation processes concentrated on dipole–dipole interactions which are usually the dominant relaxation processes in biological macromolecules. With the ever-higher magnetic field strengths used, relaxation due to chemical shift anisotropy (CSA) gains importance since it increases with the square of the magnetic field. For example, magnetization transfer through carbonyl carbons becomes less efficient at high magnetic fields because of the large CSA of these carbons. On the other hand, CSA can be used in transverse relaxation-attenuated (TROSY) experiments [269] at high magnetic fields to reduce transverse relaxation by a constructive use of the interference between dipole–dipole coupling and CSA. TROSY experiments have the potential to

make possible detailed NMR studies of proteins much larger than 50 kDa.

In this review the author hopes to have made clear that NMR of biological macromolecules is extremely rich in experimental techniques which provide a flexibility of the method to adapt to peculiarities of the system investigated. This article is intended to introduce the newcomer to the field to technical and methodological aspects of NMR with proteins in solution from basic concepts to the modern implementations and applications using hydration studies as an example. To reach this goal, a building block approach was chosen, starting with the discussion of simple elements such as RF pulses or gradients, proceeding to simple key segments and finally presenting some combinations of key segments. Along with the discussion of these elements and basic segments, experimental details were introduced which are essential for a successful application of NMR with biological macromolecules. This outline should help the reader to find special topics again later for further reference.

Acknowledgements

The author is indebted to Professor Dr K. Wüthrich for his generous support and for many fruitful discussions. Thanks are due to all the members in the research group of Professor Wüthrich, in particular to Dr F. F. Damberger and R. Riek for critical reading of the manuscript and to D. Braun for numerous technical discussions.

Appendix A: The Bloch equations

In the framework of classical physics the nuclear spins in an external magnetic field B_0 create a magnetization M along B_0. NMR is described classically by the precession of this magnetization vector $\boldsymbol{M}$ about externally applied magnetic fields. The equations of motion for the magnetization vector $\boldsymbol{M} = (M_x, M_y, M_z)$ under the action of the magnetic field vector $\boldsymbol{B} = (B_x, B_y, B_z)$ are known as the Bloch equations [30] and take the following form in the rotating frame

$$dM_x/dt = \gamma(M_yB_z - M_zB_y) - M_x/T_2$$

$$dM_y/dt = \gamma(M_zB_x - M_xB_z) - M_y/T_2$$

$$dM_z/dt = \gamma(M_xB_y - M_yB_x) - (M_z - M_0)/T_1$$

The components B_x and B_y are the components of the radiofrequency (RF) field $\boldsymbol{B}_1$ applied perpendicular to the z axis. The residual field B_z along the z axis depends on the frequency difference between a particular resonance and ω_{rf}, the rotation frequency of the rotating frame. The vector sum of $\boldsymbol{B}_1$ and $\boldsymbol{B}_z$ results in an effective field $\boldsymbol{B}_{eff}$ with an amplitude B_{eff} and with an angle Θ to the z axis

$$B_z = B_0 + \omega_{rf}/\gamma \tag{A.2}$$

$$B_{eff} = (B_1^2 + B_z^2)^{1/2} \tag{A.3}$$

$$\Theta = \arctan(B_1/B_z) \tag{A.4}$$

The magnetization vector $\boldsymbol{M}$ precesses about the effective field $\boldsymbol{B}_{eff}$ in the rotating frame. With no B_1 field present the transverse magnetization in the rotating frame precesses about the residual field $\boldsymbol{B}_z$ with the frequency

$$\boldsymbol{\Omega} = -\gamma\boldsymbol{B}_z = -\gamma\boldsymbol{B}_0 - \boldsymbol{\omega}_{rf} = \boldsymbol{\omega}_0 - \boldsymbol{\omega}_{rf} \tag{A.5}$$

where $\omega_0 = -\gamma B_0$ is the Larmor frequency, the frequency which induces nuclear transitions. With $\omega_{rf} = -\gamma B_0$ the residual magnetic field B_z vanishes and magnetization components with this Larmor frequency remain stationary in this rotating frame unless an RF pulse is applied.

It is worth noting that the precession frequency ω_0 of the magnetization is negative for nuclei with positive gyromagnetic ratios such as protons. The carrier frequency ω_{rf} has to be taken negative as well to obtain $\Omega = 0$. Setting the carrier frequency on the water resonance the precession of proton magnetization in the rotating frame is negative (from the x towards the $-y$ axis, in Fig. 38) for resonances in the spectrum left of the carrier and positive for those right of the carrier frequency [16,31]. Thus in a ^{1}H spectrum of a protein with the frequency of the rotating frame set to the water resonance frequency, magnetization of aromatic protons precesses in the direction from the x towards the $-y$ axis and

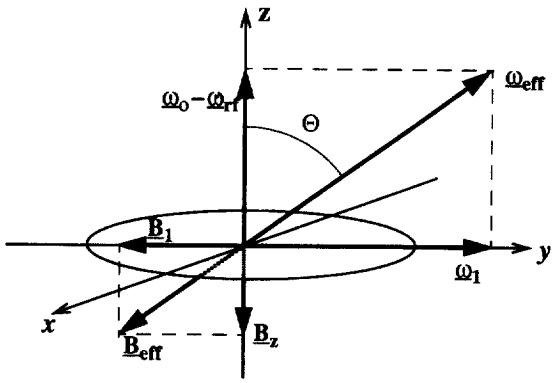

Fig. 38. Representation of the rotating frame where the z axis coincides with the external magnetic field B_0 and which rotates with respect to the laboratory frame with the frequency ω_{RF} of the applied RF frequency pulses. Vectors are shown for the effective field $\boldsymbol{B}_{eff}$ which is the vector sum of the applied RF field $\boldsymbol{B}_1$ and the residual field $\boldsymbol{B}_z$. $\boldsymbol{B}_z$ represents the difference of the resonance frequency ω_0 from ω_{RF}. Precession of magnetization components is governed by the corresponding angular frequency vectors with the values ω_{eff}, ω_1 and $(\omega_0 - \omega_{RF})$ which are shown for a positive gyromagnetic ratio in the figure. Assuming B_1 to be on-resonance with the water resonance in a proton spectrum of a protein, the magnetization corresponding to methyl protons precesses from the x towards the y axis after a 90° pulse applied along the y axis, magnetization corresponding to amide protons precesses from the x towards the $-y$ axis.

magnetization of methyl protons from the x towards the $+y$ axis.

Appendix B: The product operator formalism

The product operator formalism applies only to spin systems with spins $\frac{1}{2}$ [28]. In addition, it is assumed that there is no relaxation and that the chemical shift difference between two scalar coupled nuclei is much larger than their mutual scalar coupling J. In this framework the spin operators are transformed within their basis set (Table 2) by the three operators representing chemical shift, scalar coupling and RF pulses. The transformation of the spin operators during the course of a pulse sequence can be described by simple rules which are summarized in the following for the cartesian and the shift operator basis. The transformation under the individual operators is indicated by an arrow ($\rightarrow$).

Transformation under the chemical shift operator $(\omega\tau I_z)$:

$$I_x \rightarrow I_x \cos(\omega\tau) + I_y \sin(\omega\tau) \tag{A.6}$$

$$I^+ \rightarrow I^+ \, e^{-i\omega\tau}$$

$$I_y \rightarrow I_y \cos(\omega\tau) - I_x \sin(\omega\tau)$$

$$I^- \rightarrow I^- \, e^{i\omega\tau}$$

$$I_z \rightarrow I_z$$

Transformation under the scalar spin–spin coupling operator $(2\pi J\tau I_z S_z)$:

$$I_x \rightarrow I_x \cos(\pi J\tau) + 2I_y S_z \sin(\pi J\tau)$$

$$I^+ \rightarrow I^+ \cos(\pi J\tau) - 2I^+ S_z \sin(\pi J\tau) \tag{A.7}$$

$$I_y \rightarrow I_y \cos(\pi J\tau) - 2I_x S_z \sin(\pi J\tau)$$

$$I^- \rightarrow I^- \cos(\pi J\tau) + 2I^- S_z \sin(\pi J\tau)$$

$$I_z \rightarrow I_z$$

$$2I_x S_z \rightarrow 2I_x S_z \cos(\pi J\tau) + I_y \sin(\pi J\tau)$$

$$2I^+ S_z \rightarrow 2I^+ S_z \cos(\pi J\tau) - iI^+ \sin(\pi J\tau)$$

$$2I_y S_z \rightarrow 2I_y S_z \cos(\pi J\tau) - I_x \sin(\pi J\tau)$$

$$2I^- S_z \rightarrow 2I^- S_z \cos(\pi J\tau) + iI^- \sin(\pi J\tau)$$

$$2I_x S_x \rightarrow 2I_x S_x$$

$$2I^+ S^+ \rightarrow 2I^+ S^+$$

$$2I_y S_x \rightarrow 2I_y S_x$$

$$2I^- S^+ \rightarrow 2I^- S^+$$

$$2I_z S_z \rightarrow 2I_z S_z$$

Transformation of the cartesian spin operators under the operator for an RF pulse with angle β and phase ϕ (βI_ϕ):

$$I_x \rightarrow -I_z \sin\beta \sin\phi + I_x(\cos\beta \sin^2\phi + \cos^2\phi)$$

$$+ I_y \sin^2(\beta/2) \sin 2\phi \tag{A.8}$$

$$I_y \rightarrow I_z \sin\beta\cos\phi + I_y(\cos\beta\cos^2\phi + \sin^2\phi) + I_x \sin^2(\beta/2)\sin 2\phi$$

$$I_z \rightarrow I_z \cos\beta + I_x \sin\beta\sin\phi - I_y \sin\beta\cos\phi$$

Transformation of the shift spin operators under the operator for an RF pulse with angle β and phase ϕ (βI_ϕ):

$$I^+ \rightarrow I^- \sin^2(\beta/2)\,e^{i2\phi} + I^+ \cos^2(\beta/2) + iI_z \sin(\beta)\,e^{i\phi} \quad (A.9)$$

$$I^- \rightarrow I^- \cos^2(\beta/2) + I^+ \sin^2(\beta/2)\,e^{-i2\phi} - iI_z \sin(\beta)\,e^{-i\phi}$$

$$I_z \rightarrow -iI^- \sin(\beta)\,e^{i\phi}/2 + iI^+ \sin(\beta)\,e^{-i\phi}/2 + I_z\cos(\beta)$$

For the most frequently used RF pulses with flip angle 90° and 180° and with RF phases which are multiples n of $\pi/2$ (90°) the transformation rules become much simpler and can be written in a compact form. For 180° pulses the following rules are obtained

$$I_x \rightarrow (-1)^n I_x \quad (A.10)$$

$$I^+ \rightarrow (-1)^n I^-$$

$$I_y \rightarrow (-1)^{n+1} I_y$$

$$I^- \rightarrow (-1)^n I^+$$

and for 90° pulses

$$I_x \rightarrow -I_z \sin(n\pi/2) + I_x \cos^2(n\pi/2) \quad (A.11)$$

$$I^+ \rightarrow (-1)^n I^-/2 + I^+/2 + i^{n+1} I_z$$

$$I_y \rightarrow I_z \cos(n\pi/2) + I_y \sin^2(n\pi/2)$$

$$I^- \rightarrow I^-/2 + (-1)^n I^+/2 + (-i)^{n+1} I_z$$

$$I_z \rightarrow I_x \sin(n\pi/2) - I_y \cos(n\pi/2)$$

$$I_z \rightarrow -(i)^{n+1} I^-/2 - (-i)^{n+1} I^+/2$$

Operators transform individually under the rules formulated in Eqs. (A.6)–(A.11) even in products of operators, except for anti-phase terms (Table 2) which have to be treated as a unit using Eq. (A.7). However, these terms can be treated consecutively when different couplings to the same spin exist.

Even though calculations with the product operator formalism are in principle easy, quite a large number of terms may have to be treated when describing a pulse sequence, making computer programs performing the calculations very attractive [36,37].

References

[1] M. Saunders, A. Wishnia, J.G. Kirkwood, J. Am. Chem. Soc. 79 (1957) 3289.

[2] J.S. Cohen, J.W. Jaroszewski, O. Kaplan, J. Ruiz-Cabello, S.W. Collier, Progr. NMR Spectrosc. 28 (1995) 53.

[3] J. Jeener, Ampere International Summer School, Basko Polje, Yugoslavia, 1971.

[4] W.P. Aue, E. Bartholdi, R.R. Ernst, J. Chem. Phys. 64 (1976) 2229.

[5] K. Wüthrich, G. Wider, G. Wagner, W. Braun, J. Mol. Biol. 155 (1982) 311.

[6] G. Wider, K.H. Lee, K. Wüthrich, J. Mol. Biol. 155 (1982) 367.

[7] G. Wider, S. Macura, A. Kumar, R.R. Ernst, K. Wüthrich, J. Magn. Reson. 56 (1984) 207.

[8] J. Jeener, B.H. Meier, P. Bachmann, R.R. Ernst, J. Chem. Phys. 71 (1979) 4546.

[9] A. Kumar, R.R. Ernst, K. Wüthrich, Biochem. Biophys. Res. Commun. 95 (1980) 1.

[10] A.S. Arseniev, G. Wider, F.J. Joubert, K. Wüthrich, J. Mol. Biol. 159 (1982) 323.

[11] P. Strop, G. Wider, K. Wüthrich, J. Mol. Biol. 166 (1983) 641.

[12] W. Braun, G. Wider, K.H. Lee, K. Wüthrich, J. Mol. Biol. 169 (1983) 921.

[13] M.P. Williamson, T.F. Havel, K. Wüthrich, J. Biol. Mol. 182 (1985) 295.

[14] G.M. Clore, A.M. Gronenborn, Progr. NMR Spectrosc. 23 (1991) 43.

[15] K. Wüthrich, NMR of Proteins and Nucleic Acids, Wiley, New York, 1986.

[16] R.R. Ernst, G. Bodenhausen, A. Wokaun, Principles of Nuclear Magnetic Resonance in One and Two Dimensions, Clarendon Press, Oxford, 1987 and 1994.

[17] A.E. Derome, Modern NMR Techniques for Chemistry Research, Pergamon Press, Oxford, 1987.

[18] M. Goldman, Quantum Description of High-Resolution NMR in Liquids, Clarendon Press, New York, 1988.

[19] C.P. Slichter, Principles of Magnetic Resonance, Springer, Berlin, 1992.

[20] G.M. Clore, A.M. Gronenborn (Eds.), NMR of Proteins, CRC Press, Boca Raton, 1993.

[21] W.R. Croasmun, R.M.K. Carlson (Eds.), Two-Dimensional NMR Spectroscopy: Applications for Chemists and Biochemists, VCH, New York, 1994.

[22] J.N.S. Evans, Biomolecular NMR Spectroscopy, Oxford University Press, Oxford, 1995.
[23] F.A. Bovey, P.A. Mirau, Nuclear Magnetic Resonance Spectroscopy of Macromolecules, Academic Press, San Diego, 1996.
[24] J. Cavanagh, W.J. Fairbrother, A.G. Palmer III, N.J. Skelton, Protein NMR Spectroscopy: Principles and Practice, Academic Press, San Diego, 1996.
[25] S.K. Sarkar (Ed.), NMR Spectroscopy and its Application in Biomedical Research, Elsevier, Amsterdam, 1996.
[26] F.J.M. van de Ven, Multidimensional NMR in Liquids, VCH, New York, 1996.
[27] J.L. Markley, S.J. Opella (Eds.), Biological NMR Spectroscopy, Oxford University Press, New York, 1997.
[28] O.W. Sørensen, G.W. Eich, M.H. Levitt, G. Bodenhausen, R.R. Ernst, Progr. NMR Spectrosc. 16 (1983) 163.
[29] A. Abragam, The Principles of Nuclear Magnetism, Oxford University Press, London, 1961.
[30] F. Bloch, Phys. Rev. 70 (1946) 460.
[31] M.H. Levitt, J. Magn. Reson. 126 (1997) 164.
[32] F. Bloch, A. Siegert, Phys. Rev. 57 (1940) 522.
[33] N.F. Ramsey, Phys. Rev. 100 (1955) 1191.
[34] M.A. McCoy, L. Müller, J. Magn. Reson. 98 (1992) 674.
[35] M.A. McCoy, L. Müller, J. Magn. Reson. 99 (1992) 18.
[36] J. Shriver, J. Magn. Reson. 94 (1991) 612.
[37] P. Güntert, N. Schaefer, G. Otting, K. Wüthrich, J. Magn. Reson. 101 (1993) 103.
[38] G. Bodenhausen, H. Kogler, R.R. Ernst, J. Magn. Reson. 58 (1984) 370.
[39] A. Bain, J. Magn. Reson. 56 (1984) 418.
[40] H. Kessler, M. Gehrke, C. Griesinger, Angew. Chem., Int. Ed. Engl. 27 (1988) 490.
[41] L. Werbelow, J. Magn. Reson. 57 (1984) 136.
[42] C. Biamonti, C.B. Rios, B.A. Lyons, G.T. Montelione, Adv. Biophys. Chem. 4 (1994) 51–120.
[43] L. Braunschweiler, R.R. Ernst, J. Magn. Reson. 53 (1983) 521.
[44] A. Bax, D.G. Davis, J. Magn. Reson. 65 (1985) 355.
[45] G.A. Morris, R. Freeman, J. Am. Chem. Soc. 101 (1979) 760.
[46] A. Bax, Meth. Enzym. 176 (1989) 151.
[47] R. Bazzo, J. Boyd, J. Magn. Reson. 75 (1987) 452.
[48] S.R. Hartmann, E.L. Hahn, Phys. Rev. 128 (1962) 2042.
[49] I. Solomon, Phys. Rev. 99 (1955) 559.
[50] D. Neuhaus, M. Williamson, The Nuclear Overhauser Effect in Structural and Conformational Analysis, VCH, New York, 1989.
[51] A. Kumar, G. Wagner, R.R. Ernst, K. Wüthrich, J. Am. Chem. Soc. 103 (1981) 3654.
[52] T.E. Bull, Progr. NMR Spectrosc. 24 (1992) 377.
[53] A.A. Bothner-By, R.L. Stephens, J. Lee, C.D. Warren, R.W. Jeanloz, J. Am. Chem. Soc. 106 (1984) 811.
[54] A. Bax, D.G. Davis, J. Magn. Reson. 63 (1985) 207.
[55] G. Bodenhausen, R. Freeman, D.L. Turner, J. Magn. Reson. 27 (1977) 511.
[56] R. Freeman, S.P. Kempsell, M.H. Levitt, J. Magn. Reson. 38 (1980) 453.
[57] M.H. Levitt, Progr. NMR Spectrosc. 18 (1986) 61.
[58] L. Emsley, Meth. Enzym. 239 (1994) 207.
[59] H. Kessler, H. Oschkinat, C. Griesinger, W. Bermel, J. Magn. Reson. 70 (1986) 106.
[60] H. Geen, R. Freeman, J. Magn. Reson. 93 (1991) 93.
[61] L. Emsley, G. Bodenhausen, Chem. Phys. Lett. 165 (1990) 469.
[62] J.-P. Böhlen, G. Bodenhausen, J. Magn. Reson. A 102 (1993) 293.
[63] P.C.M. van Zijl, T.-L. Hwang, M. O'Neil Johnson, M. Garwood, J. Am. Chem. Soc. 118 (1996) 5510.
[64] E. Kupče, R. Freeman, J. Magn. Reson. 127 (1997) 36.
[65] M. Garwood, Y. Ke, J. Magn. Reson. 94 (1991) 511.
[66] T.-L. Hwang, P.C.M. van Zijl, M. Garwood, J. Magn. Reson. 124 (1997) 250.
[67] E.O. Stejskal, J.E. Tanner, J. Chem. Phys. 42 (1965) 288.
[68] G. Wider, V. Dötsch, K. Wüthrich, J. Magn. Reson. A 108 (1994) 255.
[69] A. Bax, S.S. Pochapsky, J. Magn. Reson. 99 (1992) 638.
[70] G. Wider, K. Wüthrich, J. Magn. Reson. B 102 (1993) 239.
[71] J. Keeler, R.T. Clowes, A.L. Davis, E.D. Laue, Meth. Enzym. 239 (1994) 145.
[72] L.E. Kay, Curr. Opinion Struct. Biol. 5 (1995) 674.
[73] G. Wider, R. Riek, K. Wüthrich, J. Am. Chem. Soc. 118 (1996) 11629.
[74] C.J.R. Counsell, M.H. Levitt, R.R. Ernst, J. Magn. Reson. 64 (1985) 470.
[75] D. Canet, Progr. NMR Spectrosc. 30 (1997) 101.
[76] W.E. Maas, F. Laukien, D.G. Cory, J. Magn. Reson. A 103 (1993) 115.
[77] B.A. Messerle, G. Wider, G. Otting, C. Weber, K. Wüthrich, J. Magn. Reson. 85 (1989) 608.
[78] W.E. Maas, D.G. Cory, J. Magn. Reson. A 112 (1995) 229.
[79] D.C. Champeney, Fourier Transforms and Their Physical Applications, Academic Press, New York, 1973.
[80] A.G. Redfield, S.D. Kunz, J. Magn. Reson. 19 (1975) 250.
[81] D. Marion, K. Wüthrich, Biochem. Biophys. Res. Commun. 113 (1983) 967.
[82] J.C.J. Barna, E.D. Laue, J. Magn. Reson. 75 (1987) 384.
[83] P. Schmieder, A.S. Stern, G. Wagner, J.C. Hoch, J. Biomol. NMR 4 (1994) 483.
[84] P. Schmieder, A.S. Stern, G. Wagner, J.C. Hoch, J. Magn. Reson. 125 (1997) 332.
[85] M. Gueron, P. Plateau, M. Decorps, Progr. NMR Spectrosc. 23 (1991) 135.
[86] G. Wider, R.V. Hosur, K. Wüthrich, J. Magn. Reson. 52 (1983) 130.
[87] M. Piotto, V. Saudek, V. Sklenar, J. Biomol. NMR 2 (1992) 661.
[88] S. Grzesiek, A. Bax, J. Am. Chem. Soc. 115 (1993) 12593.
[89] S. Mori, C. Abeygunawardana, M.O. Johnson, P. van Zijl, J. Magn. Reson. B 108 (1996) 94. Correction in J. Magn. Reson. B, 110 (1996) 321.
[90] V. Sklenar, J. Magn. Reson. A 114 (1995) 132.
[91] C. Anklin, M. Rindlisbacher, G. Otting, F.H. Laukien, J. Magn. Reson. B 106 (1995) 199.
[92] P. Broekaert, J. Jeener, J. Magn. Reson. A 113 (1995) 60.

[93] A. Louis-Joseph, D. Abergel, J.-Y. Lallemand, J. Biomol. NMR 5 (1995) 212.
[94] H.T. Edzes, J. Magn. Reson. 86 (1990) 293.
[95] A. Sobol, G. Wider, H. Iwai, K. Wüthrich, J. Magn. Reson., 130 (1998) 262.
[96] R. Hurd, J. Magn. Reson. 93 (1991) 666.
[97] E.O. Stejskal, J. Schaefer, J. Magn. Reson. 14 (1974) 160.
[98] G. Zhu, D.A. Torchia, A. Bax, J. Magn. Reson. A 105 (1993) 219.
[99] D. Marion, A. Bax, J. Magn. Reson. 79 (1988) 352.
[100] D.I. Hoult, C.-N. Chen, H. Eden, M. Eden, J. Magn. Reson. 51 (1983) 110.
[101] G. Wider, J. Magn. Reson. 89 (1990) 406.
[102] M.A. Delsuc, J.Y. Lallemand, J. Magn. Reson. 69 (1986) 504.
[103] D.I. Hoult, R.E. Richards, Proc. R. Soc. London, Ser. A 344 (1975) 311.
[104] C. Griesinger, O.W. Sørensen, R.R. Ernst, J. Magn. Reson. 84 (1989) 14.
[105] O.W. Sørensen, J. Magn. Reson. 89 (1990) 210.
[106] L.E. Kay, G.M. Clore, A. Bax, A.M. Gronenborn, Science 249 (1990) 411.
[107] T. Szyperski, G. Wider, J. Bushweller, K. Wüthrich, J. Biomol. NMR 3 (1993) 127.
[108] T. Szyperski, G. Wider, J. Bushweller, K. Wüthrich, J. Am. Chem. Soc. 115 (1993) 9307.
[109] A. Bax, M. Ikura, L.E. Kay, G. Zhu, J. Magn. Reson. 91 (1991) 174.
[110] D. Marion, M. Ikura, R. Tschudin, A. Bax, J. Magn. Reson. 85 (1989) 393.
[111] D.J. States, R.A. Haberkorn, D.J. Ruben, J. Magn. Reson. 48 (1982) 286.
[112] R.E. Hoffman, G.C. Levy, Progr. NMR Spectrosc. 23 (1991) 211.
[113] J.C. Hoch, A.S. Stern, NMR Data Processing, Wiley-Lyss, New York, 1996.
[114] I. Pelczer, B.G. Carter, in: D.G. Reid (Ed.), Protein NMR Techniques, Methods in Molecular Biology, vol. 60, Humana Press, New Jersey, 1997, p. 71.
[115] E. Bartholdi, R.R. Ernst, J. Magn. Reson. 11 (1973) 9.
[116] G. Otting, H. Widmer, G. Wagner, K. Wüthrich, J. Magn. Reson. 66 (1986) 187.
[117] P. Güntert, V. Dötsch, G. Wider, K. Wüthrich, J. Biomol. NMR 2 (1992) 619.
[118] F. Delaglio, S. Grzesiek, G.W. Vuister, G. Zhu, J. Pfeifer, A. Bax, J. Biomol. NMR 6 (1995) 277.
[119] S. Sperra, A. Bax, J. Am. Chem. Soc. 113 (1991) 5490.
[120] D.S. Wishart, B.D. Sykes, J. Biomol. NMR 4 (1994) 171.
[121] D. Braun, G. Wider, K. Wüthrich, J. Am. Chem. Soc. 116 (1994) 8466.
[122] R. Wimmer, N. Müller, S.B. Petersen, J. Biomol. NMR 9 (1997) 101.
[123] P. Luginbühl, T. Szyperski, K. Wüthrich, J. Magn. Reson. B 109 (1995) 229.
[124] L. Szilagyi, Progr. NMR Spectrosc. 27 (1995) 325.
[125] D.S. Wishart, C.G. Bigam, J. Yao, F. Abildgaard, H.J. Dyson, E. Oldfield, J.L. Markley, B.D. Sykes, J. Biomol. NMR 6 (1995) 135.
[126] T. Maurer, H.R. Kalbitzer, J. Magn. Reson. B 113 (1996) 177.
[127] D.I. Hoult, Progr. NMR Spectrosc. 12 (1978) 41.
[128] D.I. Hoult, in: D.M. Grant, R.K. Harris (Eds.), Encyclopedia of Nuclear Magnetic Resonance, vol. 4256, Wiley, Chichester, UK, 1996.
[129] G.M. Morris, J. Magn. Reson. 78 (1988) 281.
[130] D.M. LeMaster, Progr. NMR Spectrosc. 26 (1994) 317.
[131] S. Grzesiek, J. Anglister, H. Ren, A. Bax, J. Am. Chem. Soc. 115 (1993) 4369.
[132] X. Shan, K.H. Gardner, D.R. Muhandiram, N.S. Rao, C.H. Arrowsmith, L.E. Kay, J. Am. Chem. Soc. 118 (1996) 6570.
[133] K. Pervushin, G. Wider, K. Wüthrich, J. Am. Chem. Soc. 119 (1997) 3842.
[134] P.C.M. Van Zijl, S. Sukumar, M. O'Neil Johnson, P. Webb, R.E. Hurd, J. Magn. Reson. A 111 (1994) 203.
[135] R.D. Black, T.A. Early, P.B. Roemer, O.M. Mueller, A. Mogro-Campero, L.G. Turner, G.A. Johnson, Science 259 (1993) 793.
[136] S. Crozier, I.M. Brereton, F.O. Zelaya, W.U. Roffmann, D.M. Doddrell, J. Magn. Reson. 126 (1997) 39.
[137] W. Jahnke, J. Magn. Reson. B 113 (1996) 262.
[138] D. Braun, G. Wider, K. Wüthrich, J. Magn. Reson. B 110 (1996) 313.
[139] A. Bax, M. Ikura, J. Biomol. NMR 1 (1991) 99.
[140] S. Grzesiek, A. Bax, J. Magn. Reson. 96 (1992) 432.
[141] A. Bax, D. Marion, J. Magn. Reson. 78 (1988) 186.
[142] D. Neuhaus, G. Wider, G. Wagner, K. Wüthrich, J. Magn.-Reson. 57 (1984) 164.
[143] G. Otting, K. Wüthrich, Q. Rev. Biophys. 23 (1990) 3.
[144] G. Wider, C. Weber, H. Widmer, R. Traber, K. Wüthrich, J. Am. Chem. Soc. 112 (1990) 9015.
[145] G. Wider, C. Weber, K. Wüthrich, J. Am. Chem. Soc. 113 (1991) 4676.
[146] K. Nagayama, A. Kumar, K. Wüthrich, R.R. Ernst, J. Magn. Reson. 40 (1980) 321.
[147] R. Baumann, G. Wider, R.R. Ernst, K. Wüthrich, J. Magn. Reson. 44 (1981) 402.
[148] L. Müller, J. Am. Chem. Soc. 101 (1979) 4481.
[149] A. Wokaun, R.R. Ernst, Chem. Phys. Lett. 52 (1977) 407.
[150] C. Griesinger, G. Otting, K. Wüthrich, R.R. Ernst, J. Am. Chem. Soc. 110 (1988) 7870.
[151] M.H. Levitt, R. Freeman, J. Magn. Reson. 43 (1981) 502.
[152] J. Cavanagh, M. Rance, J. Magn. Reson. 96 (1992) 670.
[153] J. Briand, R.R. Ernst, Chem. Phys. Lett. 185 (1991) 276.
[154] M. Kadkhodaie, T.-L. Hwang, A.J. Shaka, J. Magn. Reson. A 105 (1993) 104.
[155] U. Kerssebaum, R. Markert, J. Quant, W. Bermel, S.J. Glaser, C. Griesinger, J. Magn. Reson. 99 (1992) 184.
[156] J. Cavanagh, M. Rance, J. Magn. Reson. 88 (1990) 72.
[157] J. Cavanagh, W.J. Chazin, M. Rance, J. Magn. Reson. 87 (1990) 110.
[158] A.J. Shaka, C.J. Lee, A. Pines, J. Magn. Reson. 77 (1988) 274.
[159] M. Kadkhodaie, O. Rivas, M. Tan, A.J. Shaka, J. Magn. Reson. 91 (1991) 437.

[160] H.L. Eaton, S.W. Fesik, S.J. Glaser, G.P. Drobny, J. Magn. Reson. 90 (1990) 452.
[161] M. Rance, G. Bodenhausen, G. Wagner, K. Wüthrich, R.R. Ernst, J. Magn. Reson. 65 (1985) 497.
[162] S. Macura, K. Wüthrich, R.R. Ernst, J. Magn. Reson. 47 (1982) 351.
[163] G. Otting, J. Magn. Reson. 86 (1990) 496.
[164] J.J. Titman, A.L. Davis, E.D. Laue, J. Keeler, J. Magn. Reson. 89 (1990) 176.
[165] J. Cavanagh, J. Keeler, J. Magn. Reson. 80 (1988) 186.
[166] T.-L. Hwang, A.J. Shaka, J. Am. Chem. Soc. 114 (1992) 3157.
[167] C. Griesinger, R.R. Ernst, J. Magn. Reson. 75 (1987) 261.
[168] Z. Dezheng, T. Fujiwara, K. Nagayama, J. Magn. Reson. 81 (1989) 628.
[169] C.J. Bauer, T.A. Frenkiel, A.N. Lane, J. Magn. Reson. 87 (1990) 144.
[170] J. Fejzo, W.M. Westler, S. Macura, J.L. Markley, J. Magn. Reson. 92 (1991) 20.
[171] C.G. Hoogstraten, W.M. Westler, S. Macura, J.L. Markley, J. Am. Chem. Soc. 117 (1995) 5610.
[172] S.J.F. Vincent, C. Zwahlen, G. Bodenhausen, J. Biomol. NMR 7 (1996) 169.
[173] B. Boulat, I. Burghardt, G. Bodenhausen, J. Am. Chem. Soc. 114 (1992) 10679.
[174] J. Fejzo, W.M. Westler, S. Macura, J.L. Markley, J. Am. Chem. Soc. 112 (1990) 2574.
[175] A.A. Maudsley, R.R. Ernst, Chem. Phys. Lett. 50 (1977) 368.
[176] D.M. Doddrell, D.T. Pegg, M.R. Bendall, J. Magn. Reson. 48 (1982) 323.
[177] A.G. Palmer, J. Cavanagh, P.E. Wright, M. Rance, J. Magn. Reson. 93 (1991) 151.
[178] L. Müller, R.R. Ernst, Mol. Phys. 38 (1979) 963.
[179] A. Majumdar, E.R.P. Zuiderweg, J. Magn. Reson. A 113 (1995) 19.
[180] M.G. Schwendinger, J. Quant, J. Schleucher, S.J. Glaser, C. Griesinger, J. Magn. Reson. A 111 (1994) 115.
[181] N. Sunitha Bai, N. Hari, R. Ramachandran, J. Magn. Reson. A 106 (1994) 248.
[182] E.R.P. Zuiderweg, L. Zeng, B. Brutscher, R.C. Morshauser, J. Biomol. NMR 8 (1996) 147.
[183] A.A. Bothner-By, R. Shukula, J. Magn. Reson. 77 (1988) 524.
[184] R.R. Ernst, J. Chem. Phys. 45 (1966) 3845.
[185] A.J. Shaka, J. Keeler, T. Frenkiel, R. Freeman, J. Magn. Reson. 52 (1983) 335.
[186] A.J. Shaka, P.B. Barker, R. Freeman, J. Magn. Reson. 64 (1985) 547.
[187] T. Fujiwara, T. Anai, N. Kurihara, K. Nagayama, J. Magn. Reson. A 104 (1993) 103.
[188] Z.Starčuk Jr., , K. Bartušek, Z. Starčuk, J. Magn. Reson. A 107 (1994) 24.
[189] M.R. Bendall, J. Magn. Reson. A 112 (1995) 126.
[190] R. Fu, G. Bodenhausen, J. Magn. Reson. A 117 (1995) 324.
[191] E. Kupče, R. Freeman, J. Magn. Reson. A 118 (1996) 299.
[192] A.C. Wang, A. Bax, J. Biomol. NMR 3 (1993) 715.
[193] E. Kupče, R. Freeman, G. Wider, K. Wüthrich, J. Magn. Reson. A 120 (1996) 264.
[194] E. Kupče, R. Freeman, G. Wider, K. Wüthrich, J. Magn. Reson. A 122 (1996) 81.
[195] T.E. Skinner, M.R. Bendall, J. Magn. Reson. 124 (1997) 474.
[196] T.-L. Hwang, M. Garwood, A. Tannus, P.C.M. van Zijl, J. Magn. Reson. A 121 (1996) 221.
[197] A. Hammarström, G. Otting, J. Am. Chem. Soc. 116 (1994) 8847.
[198] M.A. McCoy, L. Müller, J. Am. Chem. Soc. 114 (1992) 2108.
[199] M.A. McCoy, L. Müller, J. Magn. Reson. A 101 (1993) 122.
[200] E. Kupče, J. Boyd, I.D. Campbell, J. Magn. Reson. A 110 (1994) 109.
[201] E. Kupče, G. Wagner, J. Magn. Reson. B 109 (1995) 329.
[202] V. Dötsch, G. Wider, J. Am. Chem. Soc. 117 (1995) 6064.
[203] P.C.M. Van Zijl, C.T.W. Moonen, J. Magn. Reson. 87 (1990) 18.
[204] A.J. Dingley, J.P. Mackay, B.E. Chapman, M.B. Morris, P.W. Kuchel, B.D. Hambly, G.F. King, J. Biomol. NMR 6 (1995) 321.
[205] A.S. Altieri, D.P. Hinton, R.A. Byrd, J. Am. Chem. Soc. 117 (1995) 7566.
[206] J. Boyd, U. Hommel, I.D. Campbell, Chem. Phys. Lett. 175 (1990) 477.
[207] A. Bax, P.G. de Jong, A.F. Mehlkopf, J. Smidt, Chem. Phys. Lett. 69 (1980) 567.
[208] V. Dötsch, G. Wider, K. Wüthrich, J. Magn. Reson. A 109 (1994) 263.
[209] A. Bax, M. Ikura, L.E. Kay, D.A. Torchia, R. Tschudin, J. Magn. Reson. 86 (1990) 304.
[210] G.V.T. Swapna, C.B. Rios, Z. Shang, G.T. Montelione, J. Biomol. NMR 9 (1997) 105.
[211] A. Bax, A.F. Mehlkopf, J. Smidt, J. Magn. Reson. 35 (1979) 167.
[212] G.W. Vuister, A. Bax, J. Magn. Reson. 98 (1992) 428.
[213] L.E. Kay, M. Ikura, A. Bax, J. Magn. Reson. 91 (1991) 84.
[214] S. Grzesiek, A. Bax, J. Biomol. NMR 3 (1993) 185.
[215] T.M. Logan, E.T. Olejniczak, R.X. Xu, S.W. Fesik, J. Biol. NMR 3 (1993) 225.
[216] D.R. Muhandiram, L.E. Kay, J. Magn. Reson. B 103 (1993) 203.
[217] M. Sattler, M.G. Schwendinger, J. Schleucher, C. Griesinger, J. Biomol. NMR 6 (1995) 11.
[218] M. Czisch, A. Ross, C. Cieslar, T.A. Holak, J. Biomol. NMR 7 (1996) 121.
[219] O.W. Sørensen, M. Rance, R.R. Ernst, J. Magn. Reson. 56 (1984) 527.
[220] A.L. Davis, G. Estcourt, J. Keeler, E.D. Laue, J.J. Titman, J. Magn. Reson. A 105 (1993) 167.
[221] F.C. Bernstein, T.F. Koetzle, G.J.B. Williams, E.F.Meyer Jr., M.D. Brice, J.R. Rodgers, O. Kennard, T. Shimanouchi, M. Tasumi, J. Mol. Biol. 112 (1977) 535.
[222] Z. Otwinowski, R.W. Schevitz, R.G. Zhang, C.L. Lawson, A. Joachimiak, R.Q. Marmorstein, B.F. Luisi, P.B. Sigler, Nature 335 (1988) 321.
[223] Y.Q. Qian, G. Otting, K. Wüthrich, J. Am. Chem. Soc. 115 (1993) 1189.

[224] K. Wüthrich, M. Billeter, P. Güntert, P. Luginbühl, R. Riek, G. Wider, Faraday Discuss. 103 (1996) 245.
[225] O.K. Daszkiewicz, J.W. Hennel, B. Lubas, T.W. Szczepkowski, Nature 200 (1963) 1006.
[226] V.P. Denisov, B. Halle, J. Mol. Biol. 245 (1995) 682.
[227] G. Otting, K. Wüthrich, J. Am. Chem. Soc. 111 (1989) 1871.
[228] G. Otting, E. Liepinsh, K. Wüthrich, Science 254 (1991) 974–980.
[229] G. Otting, E. Liepinsh, K. Wüthrich, J. Am. Chem. Soc. 113 (1991) 4363.
[230] G. Otting, E. Liepinsh, K. Wüthrich, J. Am. Chem. Soc. 114 (1992) 7093.
[231] P.S. Belton, Progr. Biophys. Mol. Biol. 61 (1994) 61.
[232] I.P. Gerothanassis, Progr. NMR Spectrosc. 26 (1994) 171.
[233] R.G. Bryant, Annu. Rev. Biophys. Biomol. Struct. 25 (1996) 29.
[234] V.P. Denisov, B. Halle, J. Peters, H.D. Hörlein, Biochemistry 34 (1995) 9046.
[235] E. Liepinsh, H. Rink, G. Otting, K. Wüthrich, J. Biomol. NMR 3 (1993) 253.
[236] E. Liepinsh, G. Otting, Nature Biotechnol. 15 (1996) 264.
[237] E. Liepinsh, G. Otting, J. Am. Chem. Soc. 116 (1994) 9670.
[238] V. Dötsch, G. Wider, G. Siegal, K. Wüthrich, FEBS Lett. 366 (1995) 6.
[239] D. Neri, M. Billeter, G. Wider, K. Wüthrich, Science 257 (1992) 1559.
[240] D. Neri, G. Wider, K. Wüthrich, Proc. Natl. Acad. Sci. U.S.A. 89 (1992) 4397.
[241] D. Neri, G. Wider, K. Wüthrich, FEBS Lett. 303 (1992) 129.
[242] R.W. Kriwacki, R.B. Hill, J.M. Flanagan, J.P. Caradonna, J.H. Prestegard, J. Am. Chem. Soc. 115 (1993) 8907.
[243] S. Grzesiek, A. Bax, J. Biomol. NMR 3 (1993) 627.
[244] P.X. Qi, J.L. Urbauer, E.J. Fuentes, M.F. Leopold, A.J. Wand, Nature Struct. Biol. 1 (1994) 378.
[245] S. Mori, M.O. Johnson, J.M. Berg, P.C.M. Van Zijl, J. Am. Chem. Soc. 116 (1994) 11982.
[246] G. Otting, E. Liepinsh, J. Biomol. NMR 5 (1995) 420.
[247] C. Dalvit, U. Hommel, J. Biomol. NMR 5 (1995) 306.
[248] S. Mori, J.M. Berg, P.C.M. Van Zijl, J. Biomol. NMR 7 (1996) 77.
[249] S. Grzesiek, A. Bax, L.K. Nicholson, T. Yamazaki, P. Wingfield, S.J. Stahl, C.J. Eyermann, D.A. Torchia, C.N. Hodge, P.Y.S. Lam, P.K. Jadhav, C.-H. Chang, J. Am. Chem. Soc. 116 (1994) 1581.
[250] G. Otting, E. Liepinsh, B.T. Farmer II, K. Wüthrich, J. Biomol. NMR 1 (1991) 209.
[251] E. Liepinsh, G. Otting, K. Wüthrich, J. Biomol. NMR 2 (1992) 447.
[252] S.H. Koenig, W.E. Schillinger, J. Biol. Chem. 244 (1969) 3283.
[253] V.P. Denisov, B. Halle, J. Mol. Biol. 245 (1995) 698.
[254] A. Wlodawer, J. Deisenhofer, R. Huber, J. Mol. Biol. 193 (1987) 145.
[255] F. Noack, Progr. NMR Spectrosc. 18 (1986) 171.
[256] V.P. Denisov, B. Halle, J. Am. Chem. Soc. 116 (1994) 10324.
[257] S.H. Koenig, R.G. Bryant, K. Hallenga, S.J. Gary, Biochemistry 17 (1978) 4348.
[258] K. Venu, V.P. Denisov, B. Halle, J. Am. Chem. Soc. 119 (1997) 3122.
[259] L. Piculell, B. Halle, J. Chem. Soc., Faraday Trans. 1 82 (1986) 401.
[260] S. Meiboom, J. Chem. Phys. 34 (1961) 375.
[261] B. Halle, H. Wennerström, J. Chem. Phys. 75 (1981) 1928.
[262] V.P. Denisov, J. Peters, H.D. Hörlein, B. Halle, Nature Struct. Biol. 3 (1996) 505.
[263] N. Bloembergen, R.V. Pound, Phys. Rev. 95 (1954) 8.
[264] J. Jeener, A. Vlassenbroek, P. Broekaert, J. Chem. Phys. 103 (1995) 1309.
[265] B. Lix, F.D. Sönnichsen, B.D. Sykes, J. Magn. Reson. A 121 (1996) 83.
[266] H. Iwai, K. Wüthrich, personal communication, 1997.
[267] M. Ikura, A. Bax, J. Am. Chem. Soc. 114 (1992) 2433.
[268] W.A. Hendrickson, K. Wüthrich (Eds.), Macromolecular Structures, Current Biology, London, 1991–1996.
[269] K. Pervushin, R. Riek, G. Wider, K. Wüthrich, Proc. Natl. Acad. Sci. U.S.A. 94 (1997) 12366.